

**PhD THESIS IN ENGINEERING**

**Development of  
Small  $\pi$ -Conjugated Molecules with Long Alkyl Chains  
for Organic Field-Effect Transistors**

(長鎖アルキル基を導入した低分子トランジスタ材料の開発)

**March, 2011**

**Iori Doi**

**Department of Applied Chemistry, Graduate School of Engineering  
Hiroshima University**





## Contents

<b>Abstract</b>	III
<b>Chapter 1    General Introduction</b>	1
<b>Chapter 2    Development of Heteroaromatic-Fused TTFs as Organic Semiconductors for Solution Processible Field-Effect Transistors</b>	
2.1    Introduction for Organic Semiconductors	4
2.2    Bis( <i>N</i> -alkyl-pyrrolo[3,4- <i>d</i> ])tetrathiafulvalenes ( <i>N</i> -alkyl-PyTTFs)	10
2.3    Bis( <i>N</i> -acyl-pyrrolo[3,4- <i>d</i> ])tetrathiafulvalenes ( <i>N</i> -acyl-PyTTFs)	20
2.4    Bis(thieno[2,3- <i>d</i> ])tetrathiafulvalenes ( $\alpha$ DT-TTFs)	26
2.5    Correlation between Electronic Structure in Solid State and Field-Effect Mobility	35
2.6    Conclusion for Chapter 2	44
<b>Chapter 3    Evaluation of C<sub>10</sub>-DNTT as a Organic Semiconductor for High Performance Thin-Film Transistors</b>	
3.1    Introduction for Alkylated DNTT	46
3.2    Evaluation on Silicon Substrates	48
3.3    Fabrication of Polymer Dielectrics	53
3.4    Evaluation on Plastic Substrates	60
3.5    Conclusion for Chapter 3	64
<b>Closing Remarks</b>	65
<b>References</b>	66
<b>Appendix</b>	
A1    OFET Operation	72
A2    Nomenclature of Tetrathiafulvalene Derivatives	74
A3    Crystallographic Data for X-ray Single-Crystal Structure Analyses	75
A4    Slideshow for Ph.D Defense	76
<b>List of publications</b>	86
<b>Acknowledgment</b>	



# Abstract

## **Chapter 1. General Introduction.**

Organic field-effect transistors (OFET) have recently attracted much attention because of such possibilities as flexible, low-cost, low processing temperature, and large-area fabrication. Performances of the OFETs reported so far are in fact lower than that their potential applications required. Development of semiconductors has been needed.

The Ph.D thesis focused on a series of small  $\pi$ -conjugated molecules that have long alkyl chains along the  $\pi$ -core. The alkylated molecules presented here were investigated in terms of molecular design, syntheses, device characteristics, solid-state structures, theoretical electronic properties, and application to flexible devices. This work involves interdisciplinary fields of research.

## **Chapter 2. Development of Heteroaromatic-Fused TTFs as Organic Semiconductors for Solution Processible Field-Effect Transistors**

A series of alkylated molecules based on a tetrathiafulvalene (TTF) framework were designed as solution-processible p-channel organic semiconductors. The TTF derivatives that have long alkyl or alkylthio groups showed high solubilities and good FET responses, which can be attributed to well-ordered layer-by-layer structures in the thin films as in the crystal structures. The alkyl chain plays an important role for the self-organizing ability. Correlation between the solid-state structures and the FET characteristics are clearly demonstrated by experimental and theoretical analyses.

## **Chapter 3. Evaluation of C<sub>10</sub>-DNNT as a Organic Semiconductor for High Performance Thin-Film Transistors**

Although the development of semiconductors based on the TTF framework did not afford superior materials, the molecular design strategy was applied to other small  $\pi$ -conjugated molecules to give several high performance materials. One of the materials, alkylated dinaphtho[2,3-*b*:2'3'-*f*]thieno[3,2-*b*]thiophene (DNNT), is a vacuum-processed semiconductor that shows excellent performances and air-stability. The author contributed to accurate and practical evaluations of FET characteristics of the alkylated DNNT by means of improving device-configurations and changing substrates. High performance OFETs on plastic substrates demonstrated in the context can be regarded as a successful exemplification of prototypical OFET applications. Structural difference of the thin films depending on substrates are also examined.

---

## 要約

### 第一章：序論

有機電界効果トランジスタ (OFET) は、高い柔軟性や大面積・低コスト・低温などでの素子作製の可能性を有するため、近年注目を集めている。しかしその特性は実用的な要求に答えられるものではなく、より一層力を入れた有機半導体材料の開発が望まれている。本論文では、 $\pi$ 骨格に長鎖アルキル基を導入した一連の低分子材料に着目し、分子設計や合成、FET特性、固体構造、理論的電子特性、フレキシブル素子への応用などについて調査した。本研究は有機合成化学や有機構造化学、半導体物理などの学際的な研究分野を取り扱う。

### 第二章：ヘテロ芳香族縮環TTFを用いた溶液プロセス可能な有機トランジスタ半導体材料の開発

テトラアチアフルバレン (TTF) を母骨格とした一連のアルキル基を置換した分子を溶液プロセスp型有機半導体として設計した。長鎖誘導体は高い溶解性と良好なFET特性を示した。構造解析からこれらの分子は薄膜中で秩序高い層状構造を形成しており、それがFET特性に寄与していると示唆される。アルキル基は溶解性だけでなく自己組織化能にも重要な役割を果たしていることが明らかになった。本文中では理論的な解析により、これらの構造と物性との相関を明確に示した。

### 第三章：高性能有機半導体アルキルDNNTの評価および応用

第二章で述べたTTFを骨格とする化合物群自体は高性能材料とは成り得なかったが、これらの分子設計は他の低分子骨格に適用され、いくつかの高性能材料を与えた。その中の一つであるアルキルDNNTは、非常に高い移動度と大気安定性を示す。筆者は、素子構造の改善や基板を変更することによって、アルキルDNNTのFET特性の正確かつ応用的な評価に取り組んだ。本文中で示されるプラスチック基板上の高性能トランジスタは、OFETの応用を鑑みた試験的な成功例と考えられる。また、基板による薄膜構造の変化についても調査し、わずかな結晶性や薄膜の表面形状などの違いが特性に影響していることが示唆された。

---

---

# Zusammenfassung

## Kapitel 1. Allgemeine Einführung

Organischen Feldeffekttransistoren (OFET) wird aufgrund ihrer vorteilhaften Eigenschaften seit einiger Zeit erhöhte Aufmerksamkeit gewidmet. Zu diesen Vorteilen zählt z. B. ihre Flexibilität, sie sind kostengünstig, besitzen geringe Verarbeitungstemperaturen und sind zur Massenfertigung geeignet. Jedoch ist die Leistungsfähigkeit von OFETs geringer als es ihre potentielle Einsatzzwecke erfordern würden, weshalb eine Weiterentwicklung dieser Halbleiter notwendig ist.

Die vorliegende Doktorarbeit beschäftigt sich mit kleinen  $\pi$ konjugierten Molekülen mit langen Alkylketten in der  $\pi$ Ebene. Die vorgestellten aklylierten Moleküle werden hinsichtlich Moleküldesign, Synthese, Eigenschaften, Strukturen, theoretische elektronische Eigenschaften und Anwendungen für flexible Bauteile untersucht. Über dies hinaus schließt die vorliegende Arbeit interdisziplinäre Forschungsbereiche mit ein.

## Kapitel 2. Entwicklung von heteroaromatisch kondensierten TTFs als organische Halbleiter für lösungsverarbeitete Feldeffekttransistoren

Mehrere alkylierte Moleküle auf Basis von Tetrathiafulvalene (TTF) Systemen wurden konzipiert als lösungsverarbeitet organische pKanal Feldeffekttransistoren. Die TTF Derivate langer Alkyl- oder AlkylthioGruppen weisen hohe Löslichkeiten und gute FET Eigenschaften auf, welche auf die geordneten Schichtenstrukturen der Dünnschichten sowie der Kristallstrukturen zurückzuführen sind. Die Alkylketten nehmen hierbei eine entscheidende Rolle in der Fähigkeit zur Selbstorganisation ein. Zusammenhänge zwischen Festkörperstrukturen und den FET Charakteristiken werden durch experimentelle sowie theoretische Analysen eindeutig demonstriert.

## Kapitel 3. Bewertung von C<sub>10</sub>DNTT als organische Halbleiter für Hochleistungs-Dünnschicht-Transistoren

Obwohl die Entwicklung von Halbleitern, welche auf TTF Anordnungen basieren, keine hochwertige Materialien bieten, wurde das molekulare Design auf andere kurze  $\pi$ konjugierte Moleküle angewendet, um verschiedene Hochleistungsmaterialien zu erhalten. Eines der Materialien, alkyliertes Dinaphto[2,3-*b*:2'3'-*f*]thieno[3,2-*b*]Thiophen (DNTT), ist ein vakuumverarbeiteter Halbleiter und weist exzellente Leistungsfähigkeit und Luftbeständigkeit auf. Der Autor trägt zur präzisen und praktisch orientierten Bewertung von FET Charakteristiken alkylierter DNTTs bei. Hierbei wird Bezug auf Verbesserung der Bauelementstruktur sowie auf Wechsel zu anderen Trägermaterialien genommen. HochleistungOFETs auf Kunststoffträgermaterialien konnten in diesem Zusammenhang erfolgreich als prototypische OFET Anwendungen demonstrativ eingesetzt werden. Ferner wurden strukturbedingte Unterschiede der Dünnschichten in Abhängigkeit von Trägermaterialien untersucht.

Abstract

## Chapter 1. General Introduction

**Impact of Organic Field-Effect Transistor.** Some people may not realize what a “transistor” is in their daily life. However, it is significantly an important technology that dominates our environment.<sup>1</sup> For example, personal computers, displays, mobile phones, RFID tags, and other intelligent electronic equipments. Most transistors around us are made of silicon, especially silicon-oxide-semiconductor field-effect transistor (MOS-FET).<sup>2</sup> On the other hand, organic field-effect transistors (OFETs) have been recently attracted much attention of many academic and industrial research groups owing to the fascinating possibilities for being flexible, stretchable, large-area manufacturable, low-cost, light-weight, and ecological.<sup>3</sup> Although OFETs will not be able to displace silicon-based FETs, it will be indispensable technology which can produce plastic electronics by combining flexible polymer substrates (Figure 1.1.1).<sup>4,5</sup>

**Current Position of OFETs among Thin-Film Transistors.** Most OFETs can be classified into the thin-film transistor (TFT) by its configuration or device structure.<sup>6</sup> Organic thin-film-based transistors (OTFTs) are often compared with hydrogenated amorphous silicon TFTs (a-Si:H-TFTs), because their mobilities and the targeting applications are very close (Table 1.1.1).<sup>7</sup> However, the rivals are competing in this field, e.g. carbon nanotube TFTs (CNT-TFTs) and amorphous metal oxide TFTs (a-MO-TFTs) in addition to the conventional smaller Si-based TFTs.<sup>8</sup> Although the mobilities of OFETs are somewhat inferior to those of the other TFTs, OTFTs have several advantages over the other TFTs, e.g., the bending radius, both p- and n-channel operations, and easy processability. In fact, demonstration of electronics applications of OTFTs to rollable display, flexible complementary circuits for inverters (CMOS), and pressure-sensors have been reported actively (Figure 1.1.2).<sup>9-11</sup>



**Figure 1.1.1.** Images of plastic electronics (Morph, published by Nokia in 2008).



**Figure 1.1.2.** (a) A rollable display demonstrated by Sony in 2009. (b) An ultra-flexible integrated circuit reported by Sekitani *et al.* in 2010.

**Table 1.1.1.** Comparison of thin-film transistors.

material	$\mu / \text{cm}^2\text{V}^{-1}\text{s}^{-1}$	bending radius / mm	channel		stability		processability			
			p	n	$\mu$	$V_{\text{th}}$	solubility	process	cost	temp / °C
poly-Si (HTPS, LTPS)	10 - 600	10	⊙	○	⊙	⊙	×	PECVD	×	100 ~ 1000
a-Si:H	0.5	10	⊙	×	×	×	×	CVD	⊙	100 ~ 350
$\mu$ c-Si:H	1 - 500	10.00	⊙	×	○	○	×	PECVD, CVD	○	100 ~ 350
Metal Oxide	10 - 20	30	×	⊙	△	○	×	sputtering	○	<100
CNT	15	10	⊙	×	NA	NA	×	PECVD, etc	△	<100
Organic (Small molecule)	1	0.5	⊙	○	△	△	△	vacuum solution	○	<100
Organic (Polymer)	0.1	0.5	⊙	○	△	△	⊙	solution	⊙	<100

**Abbreviations:** HTPS (high temperature poly-Si), LTPS (low temperature poly-Si),  $\mu$  c-Si:H (hydrogenated micro crystalline Si), CNT (carbon nanotube), CVD (chemical vapor deposition), PECVD (plasma enhanced chemical vapor deposition), vacuum (vacuum-deposition), solution (solution process such as spin-coat, drop-casting, inkjet, and printing process)

**Characters:** ⊙ high performance; ○ good; △ few examples; × almost impossible.

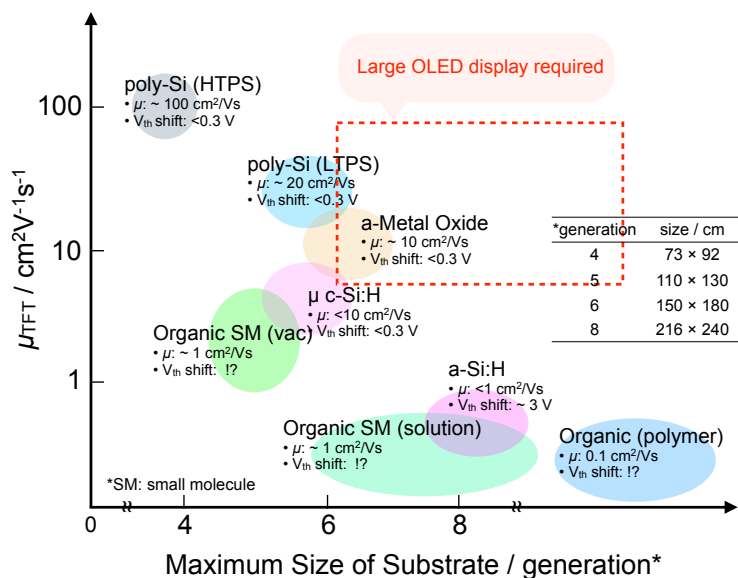


**Figure 1.1.3.** Mobility of TFTs vs maximum size of substrate of several kinds of semiconductor materials. *abbr.* vac = vacuum-deposition.

**Issues for Developing OFETs.** The features of OFETs described above are very fascinating. The virtual performances organic semiconductors are, however, fairly insufficient for industrial applications. For instance, solution-processible materials, which is capable of low-cost and large-area device fabrication, show much lower mobilities than those required for application to large OLED displays (Figure 1.1.3).<sup>12</sup> Likewise, OFET has many issues to be improved: (i) mobility (ii) on-off ratio (iii) operating voltage (threshold voltage) (iv) air-stability (v) bias-stress stability (vi) processability (solubility) (vii) accessibility (material-cost) (viii) flexibility, and (ix) reproducibility. In this work, I have focused on two particular issues; one is development of solution-processible organic semiconductors, and the other is evaluation of high performance organic semiconductors.

**Development of Semiconductors.** Most of the above issues can be solved by finding superior organic semiconductors.<sup>13</sup> In other words, design and synthesis of organic compounds is considered to be the most challenging and intrinsic subject for developing OFETs. For this reason, I have mainly studied to develop organic semiconductors based on a tetrathiafulvalene (TTF) framework, especially heteroaromatic-fused TTFs as potential compounds for solution-processible and high mobility OFETs (Figure 1.1.4, described in Chapter 2).

The benchmark material in the series of the heteroaromat-fused TTFs is dithiophene-tetrathiafulvalene (DT-TTF).<sup>14</sup> OFETs based on single-crystals of DT-TTF showed mobilities up to 1.4 cm<sup>2</sup>/Vs. The other heteroaromatic-fused TTFs are designed as an isoelectronic structure or a structural isomer of DT-TTF that can be introduced alkyl chains along the long molecular axis; alkyl- or acyl-substituted pyrrolo[3,4-*d*]fused TTFs (**1** and **2**) and alkylthio-substituted thieno[2,3-*d*] TTFs (**3**).<sup>15,16</sup> The solubilizing

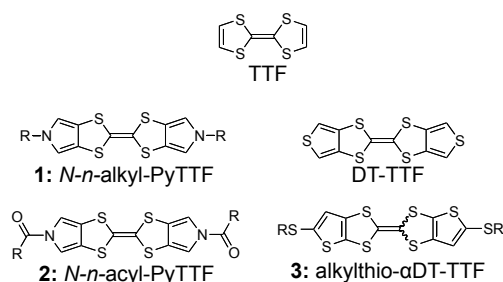


**Figure 1.1.4.** Structures of heteroaromatic-fused TTFs.

alkyl chains along the  $\pi$ -core are expected not to interfere the  $\pi$ - $\pi$  and/or S-S intermolecular interactions (section 2.2 - 2.4).

Since it is important to clarify the relationship between FET characteristics and the thin-film structures for understanding molecular design strategies for superior organic semiconductors, the molecular orientation in both bulk-single crystals and the thin film of the heteroaromatic-fused TTFs were elucidated by X-ray diffractions (XRDs). In addition, theoretical studies were carried out to evaluate electronic structures in the solid states more quantitatively (section 2.5). These results were compared to each other in the present heteroaromatic-fused TTFs and those of high performance semiconductors in other class. An advantage or disadvantage of the TTF framework are discussed.

### Evaluation of Semiconductors.

Dinaphto[2,3-*b*:2'3'-*f*]thieno[3,2-*b*]thiophene (DNNT) is the vacuum-processed semiconductor that gives high performance and highly air-stable organic thin-film transistors (OTFTs) developed in Takimiya's group (Figure 1.1.5).<sup>17-21</sup> Alkylated DNNT, having long alkyl chains along the DNNT core, is the semiconductors developed according to the same molecular design strategy as the heteroaromatic-fused TTF. Although the alkylated DNNT is insoluble, the vacuum-processed organic OFETs based on the alkylated DNNT showed superior performance than the ones based on DNNT. The very high performance of C<sub>10</sub>-DNNT required improvement of our conventional FET device structure for evaluation of characteristics more accurately and more practically. In chapter 3, as the second part of the thesis, I made effort to develop our device structure to evaluate the alkylated DNNT. I first improved the device geometry by defining the shadow mask for patterning of both organic layer and source-drain electrodes layer to evaluate alkylated DNNT as a high performance new semiconductor (section 3.2).<sup>22</sup> Second I tried to fabricate and evaluate of polymer dielectrics. The performances of dielectrics were examined by evaluation of characteristics of DNNT-based OTFTs on the dielectrics (section 3.3). Finally high performance alkylated DNNT-based OFETs on plastic substrates were demonstrated (section 3.4).<sup>23</sup> It is also important to clarify the correlation between FET characteristics and solid-state structures, I examined structural difference between on the polymer dielectrics and on the Si/SiO<sub>2</sub> dielectrics. These works were very challenging because designing device structures and fabrication and characterization of polymer dielectrics were the first attempts in Takimiya's group.

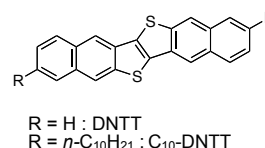


**Figure 1.1.5.** Structures of DNNT derivatives

**The two approaches.** Even though the two chapters seem to be different, each study gave important result for developing OFETs (Figure 1.1.6). The first development of semiconductors based on TTF derivatives afforded the superior molecular design strategy with long alkyl chains both as solubility and self-assembling group. The high crystallinity of the series of TTF allowed systematic analysis of the crystal structures, which enable to elucidate of relationship between

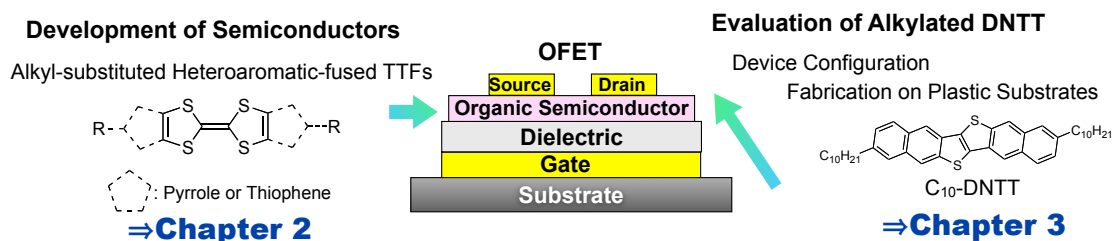


**Figure 1.1.6.** Schematic representation of this work.

## 1. General Introduction

the structures and the mobilities clearly. In the second part of my thesis, I established the advanced evaluation system, which proved DNTT with long alkyl chains to be high performance even on the plastic substrates. Furthermore, structural analysis indicate the performance can still be improved by control morphologies. The interdisciplinary study through the two approaches should be essential for developing OFET materials.

## Chapter 2.

### Development of Heteroaromatic-Fused TTFs as Organic Semiconductors for Solution Processible Field-Effect Transistors

#### 2.1 Introduction for Organic Semiconductors

**History.** Without exceptions, organic semiconductors consist of  $\pi$ -compounds because  $\pi$ -orbitals (conjugated p- and/or d-orbitals) can electronically interact with neighboring molecules with van der Waals interaction. This character realizes both electronic transport and mechanical elasticity simultaneously. A numbers of interesting  $\pi$ -compounds were already synthesized before 1980s such as phthalocyanines and polythiophenes.<sup>24,25</sup> Nevertheless, examination of application to organic field-effect transistors (OFETs) had been very limited, and the field-effect mobilities ( $\mu_{\text{FET}}$ ) of such FET characteristics were quite low ( $\mu_{\text{FET}} < 10^{-5} \text{ cm}^2/\text{Vs}$ ) (Figure 2.1.1).<sup>26,27</sup> This is because the characteristics of OFETs are very sensitive to the purity and the molecular arrangement of semiconductors on the substrates, and thus researchers had to wait establishment of the standard OFET fabrication techniques which includes vacuum-deposition (= vapor-deposition in vacuum) techniques and ultra smooth dielectric surface, e.g. heavily doped silicon with thermally grown silicon oxide (Si/SiO<sub>2</sub>) substrate (surface roughness < 0.1 nm).<sup>28</sup>

**P3AT and Pentacene.** High performance devices ( $\mu_{\text{FET}} > 10^{-3} \text{ cm}^2/\text{Vs}$ ) based on alkyl-polythiophene (P3AT) and pentacene in the late of 1980s accelerated the investigations of OFETs (Figure 2.1.2).<sup>29</sup> P3AT is the most common polymer material, which had been attracting many researchers due to the processability.<sup>30-38</sup> The crystalline thin films of P3AT can be fabricated with solution-process such as drop-cast, spin-coating, dip-coat, and printing. These processes allows low-cost and large-area fabrication of devices. The  $\mu_{\text{FET}}$  of P3AT was increased up to  $\sim 0.1 \text{ cm}^2/\text{Vs}$  by improving regio-regularity of the polymers<sup>39</sup> Recently developed thiophene-containing co-polymer-based materials showed  $\mu_{\text{FET}} \sim 1 \text{ cm}^2/\text{Vs}$  (Figure 2.1.3).<sup>40-46</sup> The  $\mu_{\text{FET}}$ s of the polymer-based OFETs are, however, generally lower than those of vacuum-deposited small-

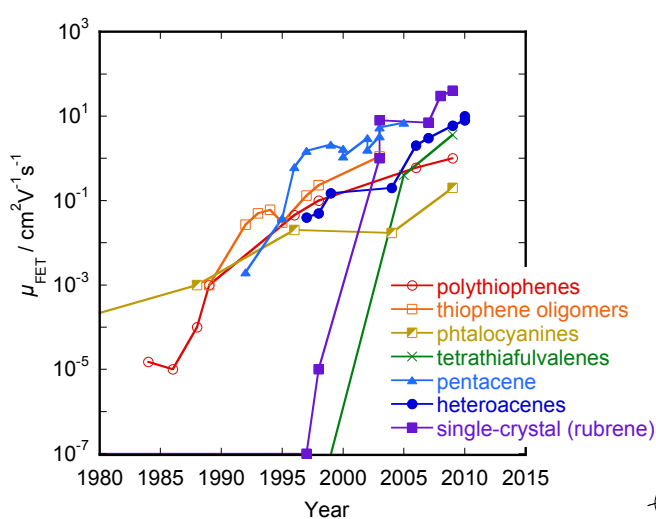


**Figure 2.1.1.** Evolution of OFET hole mobility for the most common p-type organic semiconductors. Examples of compounds of each category are described in Figure 2.1.3 - 2.1.5.

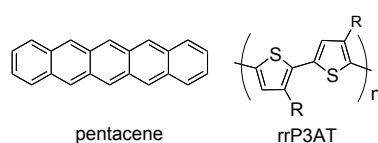


**Figure 2.1.2.** Structures of pentacene and rrP3AT.

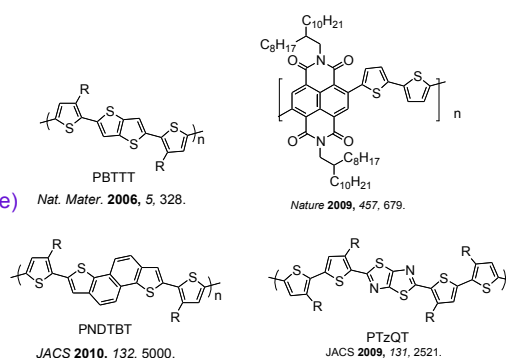


**Figure 2.1.3.** Example of thiophene containing co-polymers.

## 2. Development of Heteroaromatic-fused TTFs

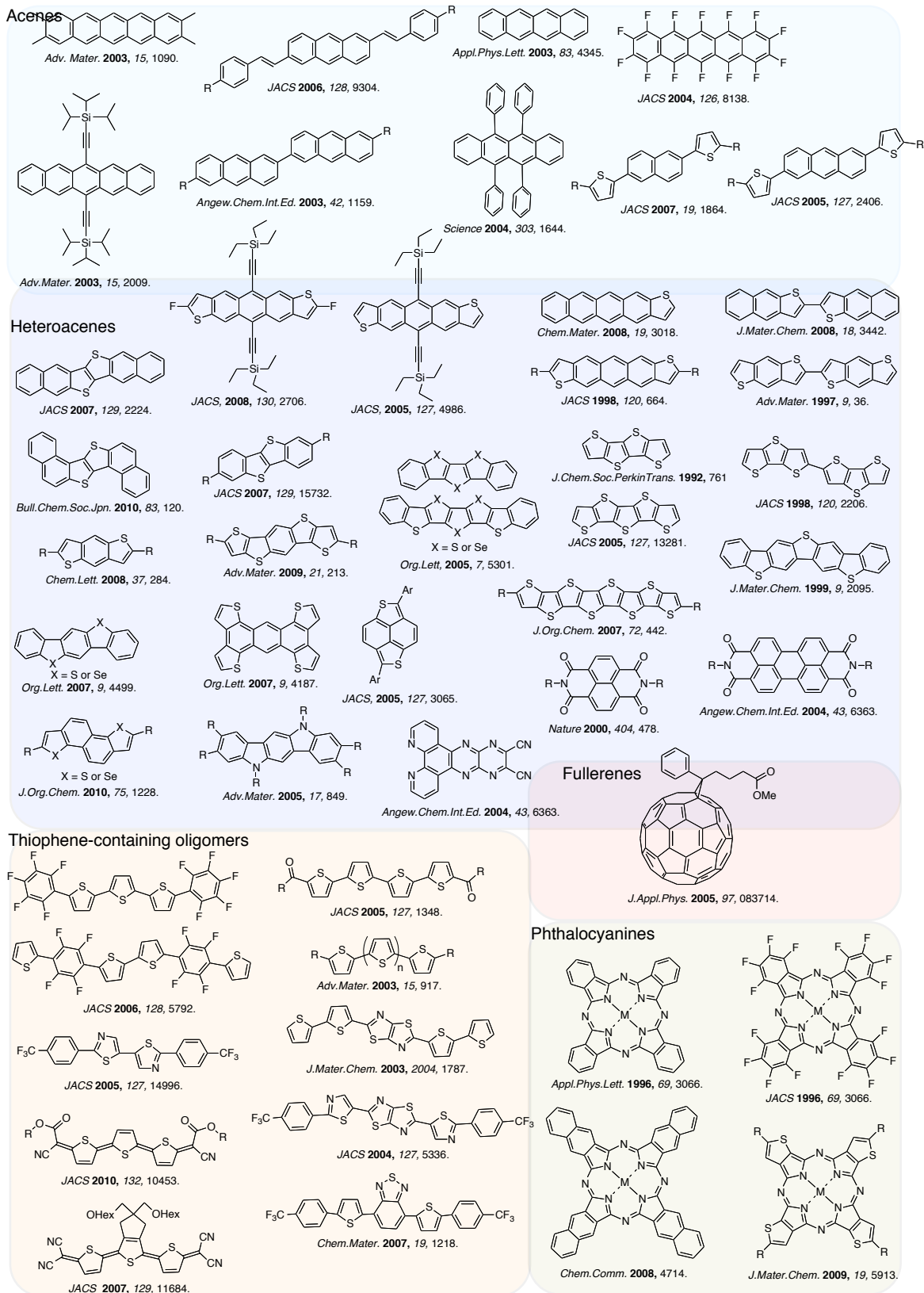


**Figure 2.1.4.** Examples of organic semiconductors based on  $\pi$ -conjugated molecules.

## Tetrathiafulvalenes (TTFs)

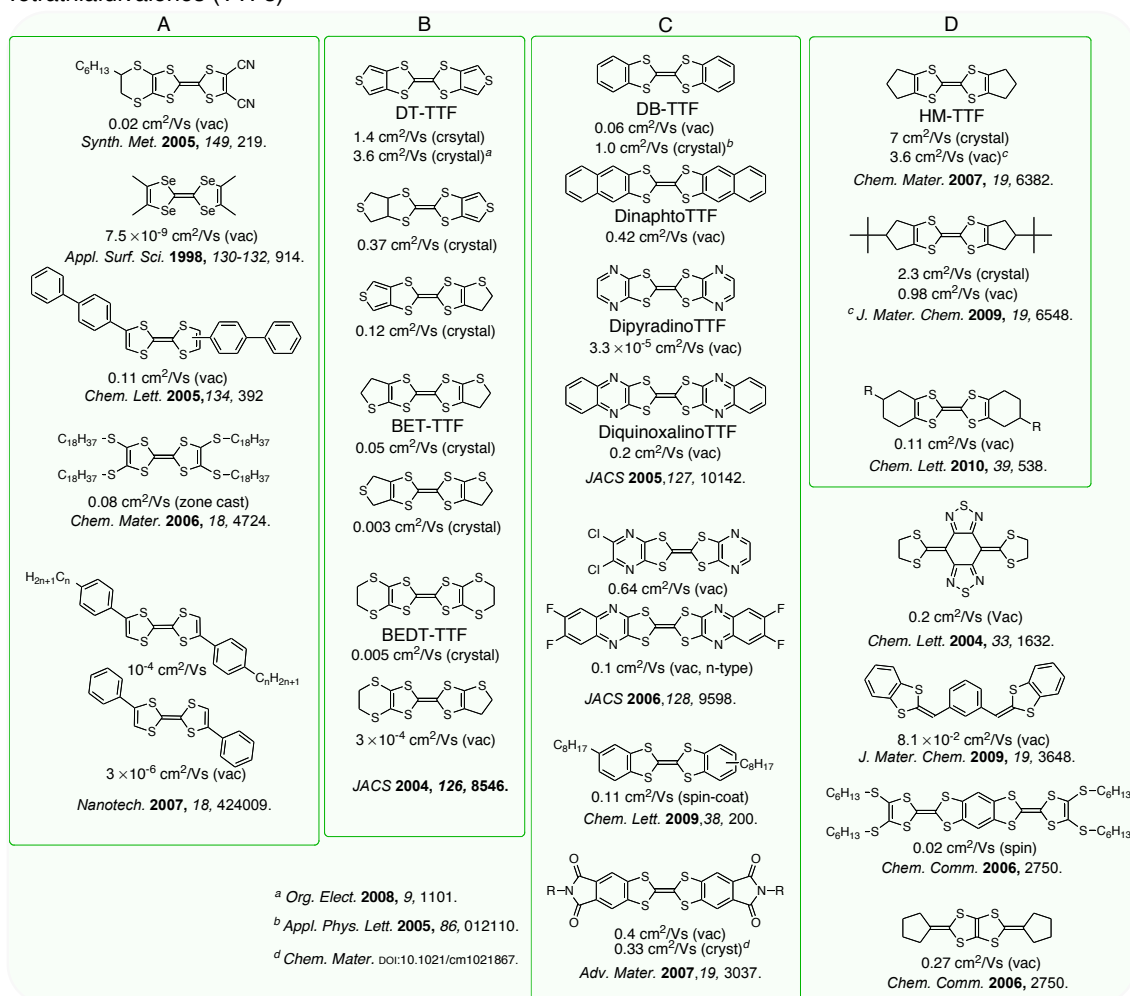


**Figure 2.1.5.** Representative TTF derivatives for OFET materials reported so far. Described values are the highest reported mobilities of the thin-film-based OFETs fabricated by vacuum-deposition (vac), spin-coating (spin), dip-coating (dip), drop-coat (drop), and single-crystal OFETs (crystal). They roughly are sorted with four groups, A is the TTF with substituents, B is TTF annulated with sulfur-containing five or six membered rings, C is six membered aromatic-fused TTFs, and D is TTF annulated with saturated rings.

molecules-based OFETs. The drawbacks of polymer materials include dispersion of molecular weight, low purity, and synthetic limitation. In addition, difficulties to control properties and analyze structures of polymer-based thin films are disadvantages as a research subject.

On the other hand, pentacene, is the most common organic semiconductors at present, gave one of the highest performance OFETs which showed  $\mu_{\text{FET}}$  of  $\sim 3$  cm<sup>2</sup>/Vs.<sup>26,29,47,48</sup> The performances of pentacene-based devices were improved in this decade by means of optimizing fabrication process of the thin films and chemical modification of the dielectric surface. The advantages of the small  $\pi$ -conjugated molecules are easy purification and possibility for fine tuning in properties, such as solubility, ionization potential, energy gap of a highest occupied molecular orbital (HOMO) and a lowest unoccupied molecular orbital (LUMO) by modification of molecular structure (see Appendix).<sup>49,50</sup> In fact, great numbers of extended  $\pi$ -compounds have been reported to be promising organic semiconductors, which shows diversity of possible structures for developing new superior organic semiconductors (Figure 2.1.4 and 2.1.5).<sup>51-55</sup> Small molecules are also convenient for a research subject because their molecular arrangement can be analyzed in detail by means of X-ray diffractions (XRDs) of both thin films and bulk single crystals.<sup>52</sup>

## 2. Development of Heteroaromatic-fused TTFs

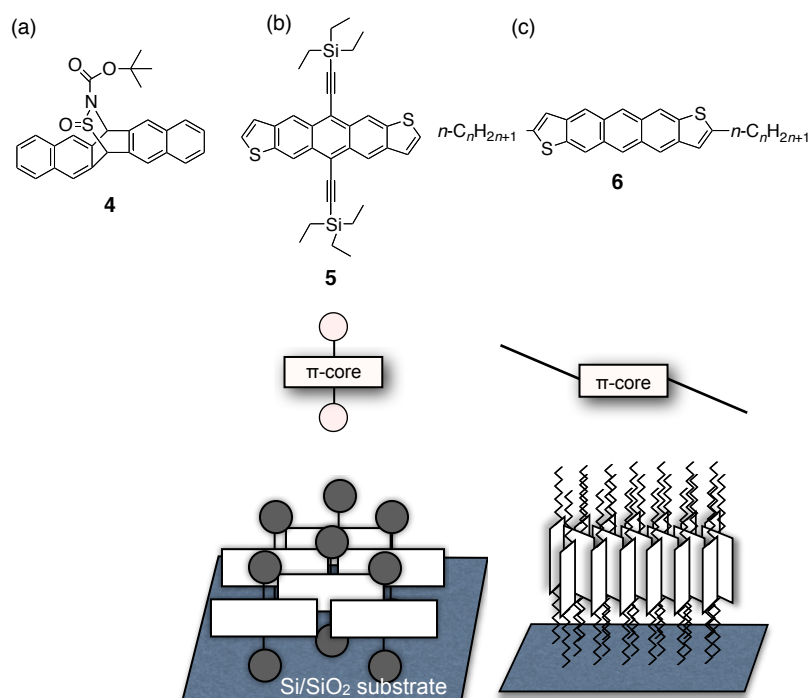


**Figure 2.1.6.** Molecular design strategy for solution-processible small  $\pi$ -conjugated molecules. Expected molecular orders on substrates are depicted in bottom.

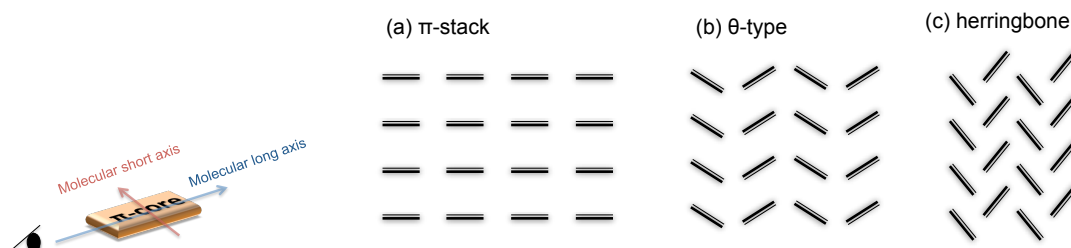


**Figure 2.1.7.** Explanation of “molecular long axis” and molecular short axis.

**Figure 2.1.8.** Explanation of packing fashion with view along molecular long axis; (a) An identical  $\pi$ -stacking. (b) Molecules are inclined for some extent. This structure has no particular name so I named the structure  $\theta$ -type temporary.<sup>73</sup> (c) A herringbone structure where molecules can pack minimally

High potential of small  $\pi$ -compounds was evidenced by single-crystal-based OFETs.<sup>19,56-60</sup> The single-crystal OFET is expected to provide idealized semiconductor channels of perfectly ordered molecules. Takeya *et al.* reported the prominent  $\mu_{\text{FETS}}$  of  $\sim 30 \text{ cm}^2/\text{Vs}$  in rubrene single crystals.<sup>61-62</sup>

**Soluble Small  $\pi$ -Conjugated Semiconductors.** One drawback of high performance materials based on small  $\pi$ -compounds is necessity of vacuum-process. Although soluble precursors of pentacene and phthalocyanine have been developed (**4**, Figure 2.1.6a), the performance of the devices were lower than the parent vacuum-deposited ones.<sup>53,63-66</sup> Approach to develop solution processible small molecules by introducing solubilizing substituents into  $\pi$ -cores has been investigated by several research groups.<sup>67</sup> Anthony *et al.* have reported that a series of soluble acene-based semiconductors that have bulky solubilizing groups along the short-axis direction of an acene-core (Figure 2.1.6b).<sup>68-70,49</sup> Bis(triethylsilyl)ethynyl-substituted anthradithiophene (**5**) gave high performance OFETs with  $\mu_{\text{FETS}}$  up to  $1 \text{ cm}^2/\text{Vs}$ .<sup>69</sup> The molecules form thin films that arranged with brick-wall-like  $\pi$ -stacking on a substrate, which could give two-dimensional conducting layer. However, when the substituent or the  $\pi$ -core is alternated slightly, the ar-

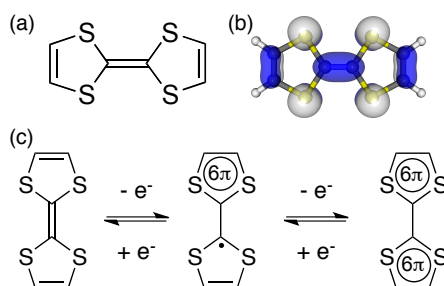


**Figure 2.1.9.** Introduction of tetrathiafulvalene (TTF): (a) Chemical structure (b) Distribution of HOMO coefficients (c) Fundamental electronic character of TTF as a donor.

angement is drastically changed into 1D  $\pi$ -stacking that showed lower  $\mu_{\text{FETS}}$  in most cases. This fact indicates that it is difficult to control molecular orientation with this molecular design strategy.

The other strategy to introduce soluble substituents is to use long aliphatic chains along a  $\pi$ -core long-axis direction (**6**, Figure 2.1.6c). The anthradithiophene core with alkyl chains has been reported as a good example.<sup>71</sup> Although the  $\mu_{\text{FETS}}$  ( $\sim 0.02$  cm<sup>2</sup>/Vs by casting) are lower than those of **5**-based OFETs, it is reported that the molecule formed layer-by-layer structure on a substrate to give conducting layers parallel to the substrate. I considered that the self-organizing ability of this molecular design would be necessary for fabrication of thin films from solution. Additionally, the resulting layer-by-layer structure allows aggregation of the  $\pi$ -cores with herringbone fashion, which is expected to give 2D intermolecular interaction. This thesis focused on the latter molecular design for solution-processible semiconductors.

General explanation to understand the terms of the molecular short and long axis,  $\pi$ -stacking, herringbone, and their intermediate structure are illustrated in Figure 2.1.7 and 2.1.8.<sup>72,73</sup>

**TTF derivatives.** Because the long alkyl chains have small steric bulkiness, the molecules are expected to be closely packed in the solid state. However, it is also expected to give not very high solubility. Several similar  $\pi$ -compounds that have long alkyl chains have been reported as vacuum-process materials.<sup>74-76,129</sup> Thus choice of  $\pi$ -core will play an important role for not only mobility but also solubility in this molecular design. Among the varieties of potential structures for organic  $\pi$ -cores, a tetrathiafulvalene (TTF) framework is attractive for following reasons (Figure 2.1.9a). TTF is well-known skeleton as an excellent molecular donor which give conductors and superconductors (Figure 2.1.9c).<sup>77</sup> With increasing interests in OFETs, TTF derivatives have been examined as promising candidates for p-type semiconductors (Figure 2.1.5).<sup>14,78-94</sup> Impressive FET characteristics have been reported by using ring-fused TTFs such as thiophene, benzene, pyridine, cyclopentane, and related nitrogen-containing aromatic moieties. The highest  $\mu_{\text{FET}}$  among the TTF derivatives have been reported using hexamethylene-TTF (HM-TTF) both in single-crystal-based devices ( $\sim 7$  cm<sup>2</sup>/Vs)<sup>87</sup> and in thin-film-based devices ( $\sim 3$  cm<sup>2</sup>/Vs).<sup>88</sup> Although their characteristics show have small on-off ratios ( $\sim 10^3$ ), the high potential of the TTF framework have been shown obviously. The key feature of TTF is strong intermolecular interaction via four sulfur atoms where HOMO coefficients largely located (Figure 2.1.9b). Furthermore, TTF derivatives are somewhat soluble compared with other extended  $\pi$ -compounds because of the small  $\pi$ -core. Considering the benefits of the strong cohesive character of the TTF cores, I have identified TTF as a promising  $\pi$ -conjugated core for use as soluble semiconducting materials for OFETs.

**Heteroaromatic-fused TTFs for Solution-Processible Semiconductors.** It is possible to design the TTF with two long alkyl chain in such a way that the resulting molecules can assume a

## 2. Development of Heteroaromatic-fused TTFs

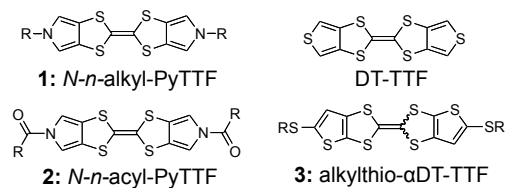


**Figure 2.1.10.** Structures of heteroaromatic-fused TTFs.

stretched structure along the TTF long axis direction, where introduced alkyl chains would not hinder intermolecular  $\pi$ - $\pi$  or S-S interactions. When the mono-substitution on each 1,3-dithiole ring is carried out, however, *cis/trans* isomerization caused by rotation of the central double bond in the TTF core readily occurs.<sup>95,96</sup> The formation of a mixture of two isomers having very different molecular shapes are not optimal for the formation of highly ordered molecular arrays in the thin-film state.<sup>80</sup> Another strategy for introduction of alkyl chains is tetra-substitution on a TTF core.<sup>81,92</sup> It also could result in large steric bulkiness which could disturb close packing in solid state and/or causes liquid crystalline character around room temperature. These may bring poor thermal stability and device operation.<sup>94</sup>

The heteroaromatic-fused TTFs shown in Figure 2.1.10 are considered to be good skeletons that are amenable to di-substitution of alkyl chains along the molecular long-axis direction with avoiding the problems discussed above, i.e., steric hinderance of S-S interaction and problematic structural disorders caused by *cis/trans* isomerization will not occur. In this series, dithiophene-tetrathiafulvalene (DT-TTF) has been reported as a high performance semiconductor.<sup>14</sup> The single-crystal OFETs based on DT-TTF showed  $\mu_{\text{FETS}} \sim 1.4 \text{ cm}^2/\text{Vs}$ . Although the DT-TTF can not be substituted with alkyl groups along the  $\pi$ -cores, bis(pyrrolo[3,4-*d*])tetrathiafulvalene (PyTTF, **1**), which is isoelectronic structure of DT-TTF, can be modified with alkyl chains easily on the N atoms. Bis(thieno[2,3-*d*])tetra-thiafulvalene ( $\alpha$ DT-TTF) also can be modified with alkyl chain at the  $\alpha$ -positions of the fused thiophene rings with keeping the same thiophene moieties as DT-TTF.<sup>97</sup> Each molecular feature will be explained in each introduction of the following sections.

In this chapter, synthesis, properties, FET characteristics, and solid-state structures of the heteroaromatic-fused TTFs with various length of alkyl substituents are described. After description of the experimental results, theoretical analysis of the molecular structures and single-crystal structures will be carried out to correlate between the FET characteristics and the structures and to discuss the potential of the present semiconductors.

## 2.2 Bis(*N*-alkyl-pyrrolo[3,4-*d*])tetrathiafulvalenes (*N*-alkyl-PyTTFs)

**Introduction.** Bis(pyrrolo[3,4-*d*])TTF (PyTTF, **1**, Figure 2.2.1) is first focused as a solution-processible skeleton among the heteroaromatic-fused TTFs. As mentioned in section 2.1, PyTTF seems to be an identical system that confirm the strategy for soluble OFET semiconductors based on the TTF core structure. Unsubstituted (**1a**), methyl (**1b**), and *n*-butyl (**1c**) PyTTF derivatives as electron donors for conducting materials were already synthesized via efficient synthetic route in 2000.<sup>98,99</sup>

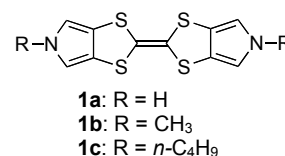
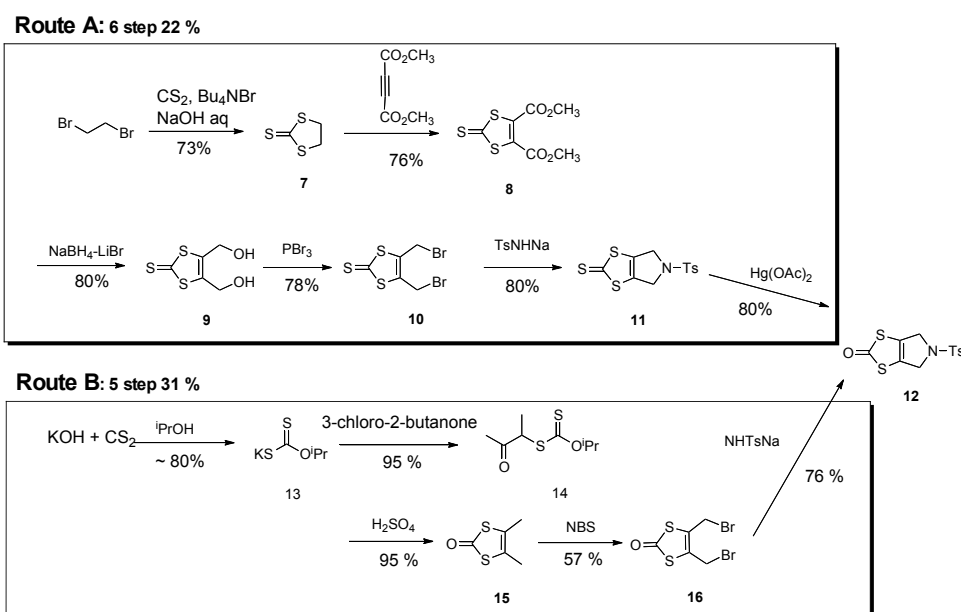


**Figure 2.2.1.** Structure of PyTTF.

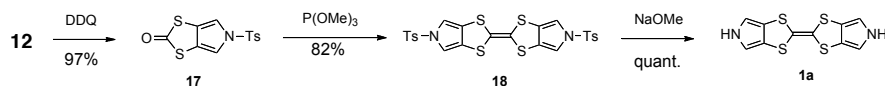
**Synthesis and Characterization.** The parent PyTTF (**1a**) was synthesized via the reported route (Scheme 2.2.1, Route A). The synthesis using tosyl protecting group on the intermediate (**11**) gave PyTTF reproducibly. However, there are three problematic steps in this route; first, dimethyl acetylenedicarbonate (reaction of **7** to **8**) is expensive for use as the starting material. Second, reduction of **8** to **9** is not reproducible, and the third, toxic Hg(OAc)<sub>2</sub> is required for the synthesis of **12** from **11**. As a result of search for another synthetic route to the key intermediate of **12**, I successfully found a new route by combining several efficient reactions (Route B).<sup>100-102</sup> Route B can afford **12** in an improved total yield (22 % to 31 %) with fewer steps (6 steps to 5 steps) and easier purification procedures.<sup>103</sup> From the key intermediate (**12**), the parent PyTTF (**1a**) was synthesized with gram scale in one batch successfully. *N*-alkylated PyTTFs with various chain lengths were then prepared by reaction of **1a** with alkyl halides (Scheme 2.2.2). All alkyl derivatives were isolated as stable yellow powders or crystals and fully characterized by spectroscopic and elemental analysis.

To evaluate the solubilizing effect of the introduced alkyl groups, the solubilities of **1b-g** were determined semi-quantitatively (see Experimental Procedures). Although the methyl derivative (**1b**) was virtually insoluble in toluene, elongation of the alkyl groups enhanced the solubility, as expected. However, in compounds with very long alkyl groups (i.e., **1f** with *n*-cetyl groups and **1g** with *n*-icosyl groups), the solubility was decreased (Table 2.2.1). These results indicate that elongation of the alkyl groups enhances the affinity to solvents by enhancing solubility but that very long alkyl groups, such as the *n*-icosyl group, facilitate strong intermolecular hydrophobic

**Scheme 2.2.1.** Synthesis of parent PyTTF (**1a**).



## 2. Development of Heteroaromatic-fused TTFs



**Scheme 2.2.2.** Synthesis of *N*-alkyl-PyTTF.

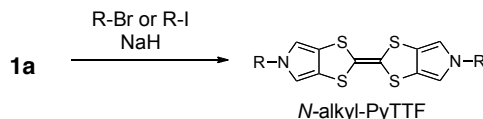


**Table 2.2.1.** Synthetic yields and properties of *N*-alkyl-PyTTFs

	R	yield/ %	mp / °C	solubility / g L <sup>-1</sup>	sublimation at ~10 <sup>-3</sup> Pa
<b>1b</b>	CH <sub>3</sub>	79	252	< 0.001	✓
<b>1c</b>	<i>n</i> -C <sub>4</sub> H <sub>9</sub>	71	198	10	-
<b>1d</b>	<i>n</i> -C <sub>8</sub> H <sub>17</sub>	75	164	29	-
<b>1e</b>	<i>n</i> -C <sub>12</sub> H <sub>25</sub>	61	127	50	-
<b>1f</b>	<i>n</i> -C <sub>16</sub> H <sub>33</sub>	79	122	4	-
<b>1g</b>	<i>n</i> -C <sub>20</sub> H <sub>41</sub>	53	121	0.4	-

in toluene at r.t.

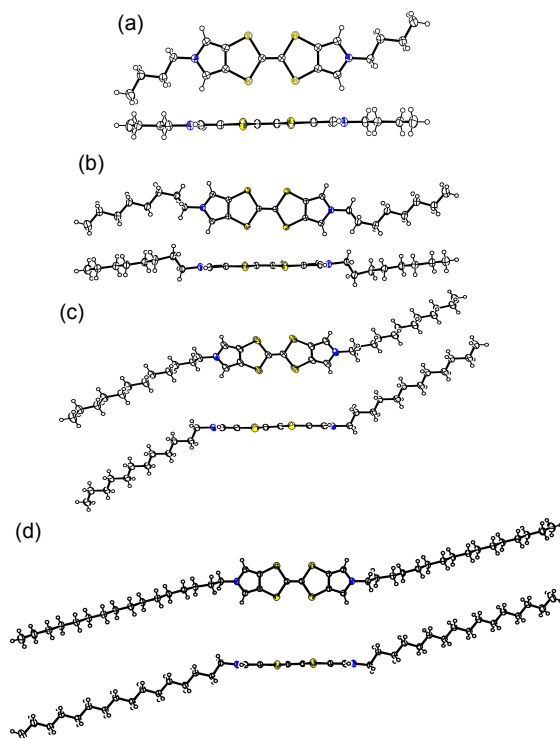


**Figure 2.2.2.** Molecular structures of **1c** (a), **1d** (b), **1e** (c), and **1f** (d).

interactions between the groups, consequently reducing the solubility of the molecules. The increased hydrocarbon-like character in the molecules are also seen in the melting points which dramatically decrease with increment of alkyl chain lengths.

Among the PyTTFs investigated in this study, unsubstituted (**1a**), *n*-butyl (**1c**), *n*-octyl (**1d**), *n*-dodecyl (**1e**), and *n*-cetyl (**1f**) derivatives afforded single crystals of high quality that could be fully characterized by single-crystal XRD. (The crystallographic data are listed in Table A1 in Appendix). Figure 2.2.2 shows the molecular structures of **1c-f**, where the PyTTF cores are almost flat in all compounds but the alkyl groups have different conformations. The *n*-butyl

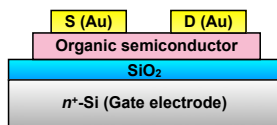


**Figure 2.2.3.** Schematic representation of OFET devices.

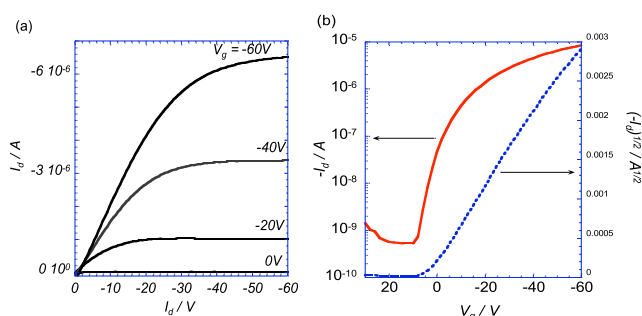


**Figure 2.2.4.** FET characteristics of **1g** (*n*-icosyl) (a) output and (b) transfer characteristics at  $V_d = -60$  V.

**Table 2.2.2** FET characteristics of devices based on **1a-g** on the Si/SiO<sub>2</sub> substrate.

	R	process <sup>a</sup>	OFET <sup>b</sup>		
			V <sub>th</sub> / V	μ / cm <sup>2</sup> V <sup>-1</sup> s <sup>-1</sup>	I <sub>on</sub> /I <sub>off</sub>
<b>1a</b>	H	<i>vac</i>		no field-effect	
<b>1b</b>	CH <sub>3</sub>	<i>vac</i>	40	5 × 10 <sup>-5</sup>	
<b>1c</b>	<i>n</i> -C <sub>4</sub> H <sub>9</sub>	<i>spin</i>	30	2 × 10 <sup>-5</sup>	10 <sup>1</sup>
<b>1d</b>	<i>n</i> -C <sub>8</sub> H <sub>17</sub>	<i>spin</i>		no field-effect	
<b>1e</b>	<i>n</i> -C <sub>12</sub> H <sub>25</sub>	<i>spin</i>	20	6 × 10 <sup>-3</sup>	10 <sup>2</sup>
<b>1f</b>	<i>n</i> -C <sub>16</sub> H <sub>33</sub>	<i>spin</i>	10	8 × 10 <sup>-3</sup>	10 <sup>4</sup>
<b>1g</b>	<i>n</i> -C <sub>20</sub> H <sub>41</sub>	<i>spin</i>	8	1 × 10 <sup>-2</sup>	10 <sup>4</sup>

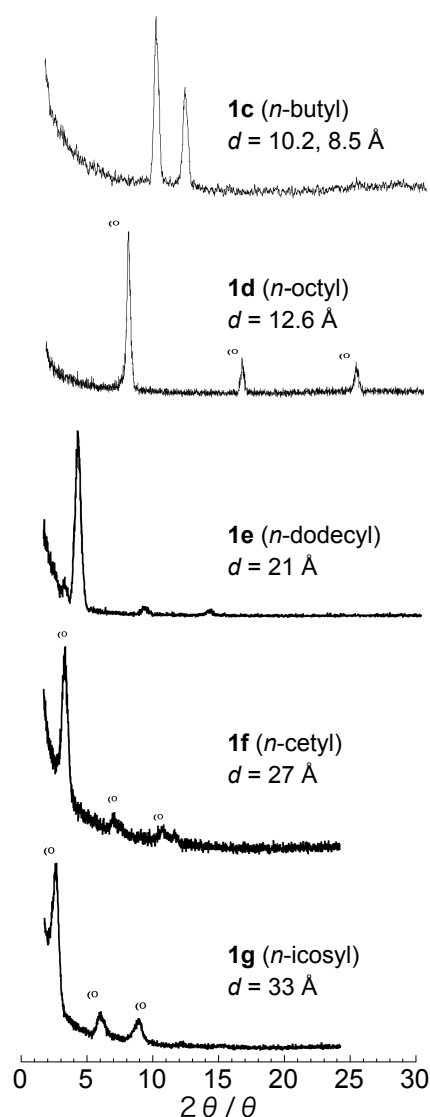
<sup>a</sup> *spin* = spin-coat, *vac* = vacuum-deposition. <sup>b</sup> Typical value. Devices are top-contact configurations with Au electrodes. *W* and *L* are 1500 and 50 μm, respectively.

groups in **1c**, taking an all-anti conformation, lie on the same plane as that of the PyTTF core, whereas the *n*-octyl groups in **1d** take a partial gauche conformation, and at the second methylene carbon from the nitrogen atoms in the pyrrole rings, the CH<sub>2</sub> moiety is normal to the PyTTF plane, while the rest of the *n*-octyl groups lie on almost the same plane as that of the PyTTF core. These molecular structures most likely minimize the space required, enabling dense packing in bulk crystals (*vide infra*). In contrast to the fairly flat molecular structures of **1c** and **1d**, **1e** and **1f** form stretched and doubly bent molecular structures in which the *n*-dodecyl groups in **1e** and the *n*-cetyl groups in **1f** take a staggered, all-anti conformation that minimizes the steric energy in the aliphatic chains.

**Deposition of Thin Films by Spin-Coating and Evaluation of FET Devices.** As previously mentioned, PyTTF derivatives with alkyl chains longer than *n*-butyl (except **1g**) were soluble enough to be spun from various solvents (e.g., dichloromethane, chloroform, THF, toluene, and chlorobenzene). Among these solvents, toluene enabled the reproducible formation of homogeneous thin films of **1c-f** by spin-coating on the Si/SiO<sub>2</sub> substrate. In contrast, homogeneous thin films of **1g**, which has *n*-icosyl groups and showed a low solubility in toluene at room temperature, were obtained only when a warm solution of **1g** in chlorobenzene (ca. 80 °C) was used. On the top of the thin-films, gold source and drain electrodes are deposited to give top-contact OFETs (Figure 2.2.3).

Evaluation of the devices was carried out under ambient conditions without any precautions taken to eliminate air and moisture. Table 2.2.2 summarizes the FET characteristics of the devices evaluated immediately after fabrication.\* The data were obtained by averaging several de-

\* The devices were degraded gradually under ambient conditions, owing to the low oxidation potentials (i.e., high HOMO levels) of **1c-1g**. See section 2.3.

**Table 2.2.3.** Interlayer spacing (*d*-spacing) of thin-film of **1a-g**

R	<i>d</i> -spacing <sup>a</sup> / Å	$\delta_d$ <sup>b</sup> / Å	<i>c</i> -axis <sup>c</sup> / Å
<b>1a</b> H	no peak	-	9.7
<b>1b</b> CH <sub>3</sub>	no peak	-	-
<b>1c</b> <i>n</i> -C <sub>4</sub> H <sub>9</sub>	10.2, 8.5	-	8.1
<b>1d</b> <i>n</i> -C <sub>8</sub> H <sub>17</sub>	12.6	4.0	12.6
<b>1e</b> <i>n</i> -C <sub>12</sub> H <sub>25</sub>	21.0	8.5	23.8
<b>1f</b> <i>n</i> -C <sub>16</sub> H <sub>33</sub>	26.8	5.8	26.9
<b>1g</b> <i>n</i> -C <sub>20</sub> H <sub>41</sub>	32.3	5.5	-

<sup>a</sup> *d* = layer distance, determined on the basis of the (001) peaks in the XRD patterns. <sup>b</sup> Increment of *d*-spacing ( $\delta_d$ ) by elongation of alkyl groups with the addition of four CH<sub>2</sub> units;  $\delta_d = d_0 - d_{n-1}$ . <sup>c</sup> In the single-crystal unit cell. **1b** and **1g** did not form single-crystals sufficient for analysis.

**Figure 2.2.5.** XRD patterns of thin-films of **1c-g**.

vices independently fabricated with each compound. OFETs using spin-coated thin-film of **1c** with short alkyl groups showed poor responses with very small field-effect modulation of drain-current; thus, field-effect mobility ( $\mu_{\text{FET}}$ ) and on-off ratio ( $I_{\text{on}}/I_{\text{off}}$ ) are very low. OFETs based on **1d** showed no current modulation on gate bias application, and thus, the FET parameters of the devices were not determined. Similarly, OFETs based on **1a** and **1b** fabricated by vacuum-deposition showed no and poor field-effect responses, respectively.

In sharp contrast, **1e**-based devices showed a typical p-channel FET response with  $\mu_{\text{FET}} = 6.8 \times 10^{-3} \text{ cm}^2/\text{Vs}$  and  $I_{\text{on}}/I_{\text{off}} = 2 \times 10^2$ . Spin-coated thin films of **1f** and **1g** with long alkyl groups also acted as semiconducting channels in the devices, and the  $\mu_{\text{FETs}}$  of these devices were in the order of  $10^{-2} \text{ cm}^2/\text{Vs}$  with  $I_{\text{on}}/I_{\text{off}} 10^4$  (Figure 2.2.4 and Table 2.2.2). These FET characteristics are fairly good for solution-processible OFET devices and comparable to OFETs based on poly(3-hexylthiophene) tested in our laboratory.

**Evaluation of Molecular Ordering by XRD Studies of Thin Films and Bulk Single Crystals.** Figure 2.2.5 shows the XRD patterns of thin films of **1c-g** deposited on an Si/SiO<sub>2</sub> substrate by spin-coating. Since all the spin-coated films (except **1c**) showed a series of peaks as-

signable to (00*l*) reflections, it is clear that well-oriented crystalline films were formed in the spin-coated film. In contrast, the vacuum-deposited film (**1a-b**) showed no peaks, indicating amorphous structure. Calculated *d*-spacings based on the first-layer line are listed in Table 2.2.3. For the thin film of **1c**, there exist two intense peaks at  $2\theta = 8.7^\circ$  and  $10.4^\circ$ , which correspond to *d*-spacings of 10.2 and 8.5 Å, respectively, indicating the existence of two crystalline phases or two different orientations normal to the substrate surface.

The calculated *d*-spacings were increased with the elongation of the alkyl groups, which can be qualitatively understood by considering that longer molecules form thicker layers. However, focusing on the increment of the *d*-spacing ( $\delta_d$ ) by the addition of four CH<sub>2</sub> units, a large increase of *d*-spacing from **1d** to **1e** is noticeable, which may correspond to a change of molecular orientation. Interestingly, the trend of FET characteristics is also drastically changed at this point, and thus, we speculate that the change of molecular orientation in the thin film and the FET characteristics can be correlated.

To gain further insight into the relationship between molecular orientation and FET characteristics, we examined the structures of **1c-f** in bulk single crystals. By comparing the *d*-spacings with the cell parameters of the bulk single crystals (Table 2.2.3), I noticed a similarity between *d*-spacings and crystallographic *c*-axes in the bulk single crystals, indicating that the preferred orientation normal to the substrate in the thin films is the *c*-axis for all the compounds.

**Molecular Orientation in Bulk Single Crystals.** Regardless of the length of alkyl groups, the crystal structures of **1c-f** are similar to one another, that is, a layer-by-layer structure consisting of alternately stacked aliphatic layers and PyTTF layers (Figures 2.2.6 and Figure 2.2.7). However, detailed examination of the molecular packing revealed that intermolecular interactions, and consequently intermolecular overlaps, are very much dependent on the compounds and dominate the carrier transport properties of FET devices. Interestingly, these four crystal structures can be classified into two groups from the viewpoint of molecular arrangement: one is **1c** and **1d** with a monoclinic space group (Figure 2.2.6), and the other is **1e** and **1f** with a triclinic space group (Figure 2.2.7).

In the PyTTF layers of the former two crystal structures with relatively short alkyl groups (**1c** and **1d**), the molecules tilt markedly from the *c*-axis (Figure 2.2.6, left), resulting in the formation of very thin active semiconducting layers where no stacking of the TTF cores exists owing to the slipping of molecules along the molecular long-axis direction (Figure 2.2.6, right). There-

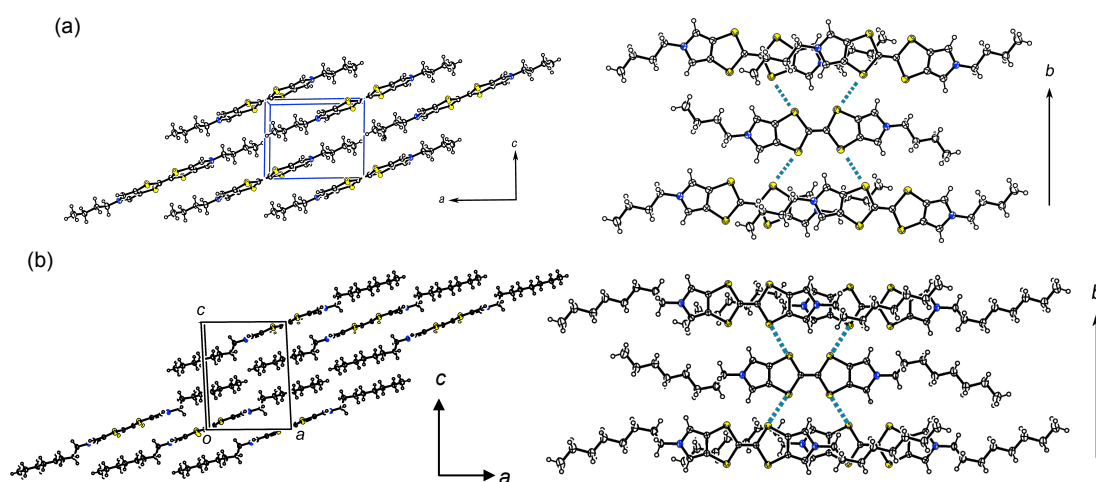


**Figure 2.2.6.** Molecular arrangement in single crystal of **1c** (a) and **1d** (b): side view of molecular layers (*b*-axis projection, left) and projections of one layer normal to the PyTTF plane (right). Side-by-side S-S short distances indicated by dashed lines are 3.63 Å for **1c** and 3.36 Å for **1d**.

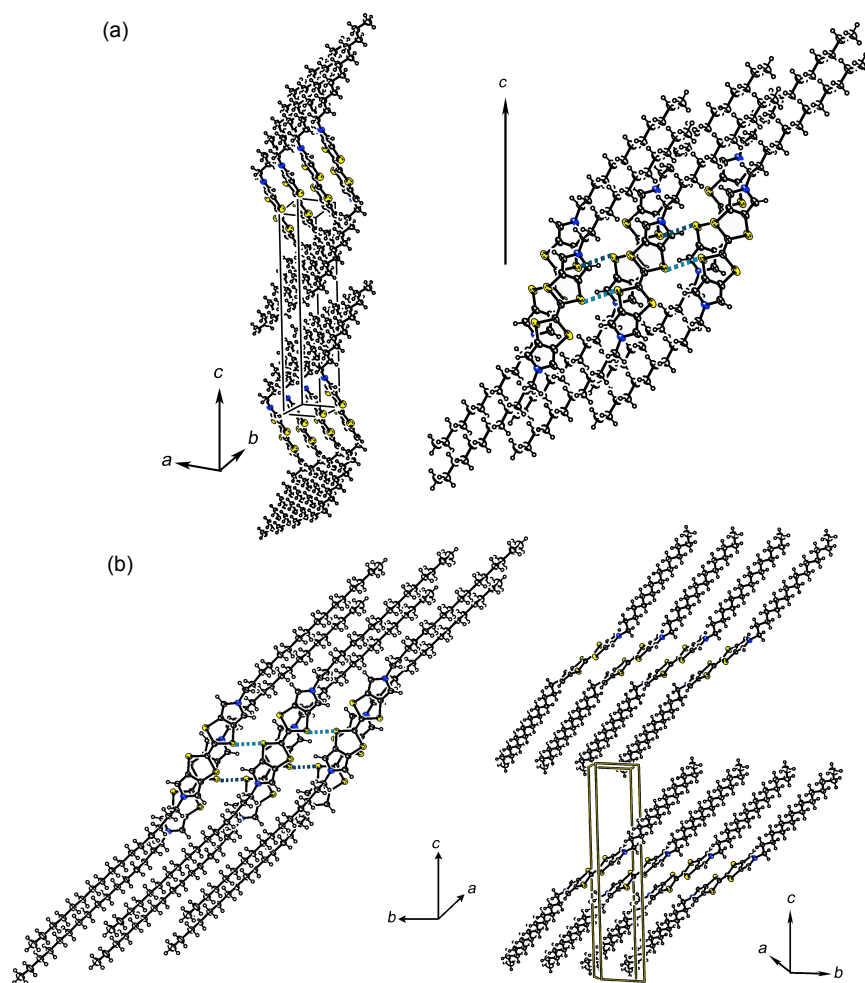


**Figure 2.2.7.** Molecular arrangement in single crystal of **1e** (a) and **1f** (b): side view of molecular layers (left) and projections of one layer normal to the PyTTF plane (right). Side-by-side S-S short distances indicated by dashed lines are 3.43 Å for **1e** and 3.40 Å for **1f**.

fore, molecular overlap along the *a*-axis direction is very small, although there are intermolecular side-by-side interactions through S–S contacts in the *b*-axis direction (3.63 Å for **1c** and 3.36 Å for **1d**).

In contrast, in the PyTTF layers of the latter group (**1e** and **1f**), both well-overlapped  $\pi$ -stacking between PyTTF moieties in the *a*-axis direction and transverse intermolecular interaction through S–S contacts (3.43 Å for **1e** and 3.40 Å for **1f**) was observed (Figure 2.2.7). This indicates that these two compounds have typical two-dimensional (2-D) TTF conducting layers, as observed in many highly conducting charge-transfer TTF salts. The existence of 2-D conducting layers on the substrate is considered to be one of the critical prerequisites to realizing high-performance OFET devices.<sup>104,105</sup> From these structural features, it appears that the FET characteristics of the present PyTTF-based OFETs are well-explained by the electronic nature of the semiconducting layer.

For inspection of poor crystallinity of thin films of unsubstituted PyTTF (**1a**) and methyl derivatives (**1b**), molecular orientation in crystal of **1a** was examined (Figure 2.2.8). The arrangement of **1a** consist of two different layers which stacked alternately along the *a*-axis, neither of which has efficient overlap between the  $\pi$ -core. It is very differed from those of the alkylated PyTTFs where repeated layer-by-layer structures were formed. The structure and the poor FET

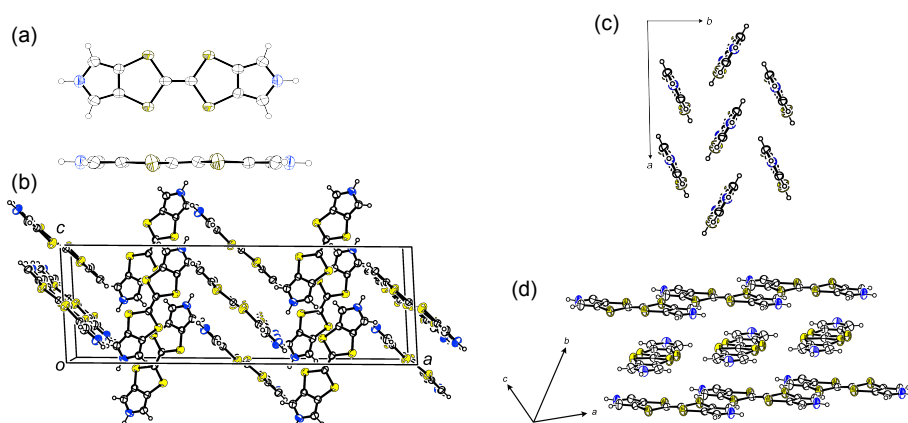


**Figure 2.2.8.** Single-crystal structure of parent PyTTF (**1a**): (a) a molecule and (b) view along *b*-axis. The crystal consists of two layers of (c) and (d) that stacked alternately along the *a*-axis.

characteristics of **1a** and **1b** indicate that the alkyl groups bring the PyTTF the self-assembling character to form 2-D layer-by-layer structure on the substrate from solution.

**Summary.** The present study on *N*-alkyl-substituted PyTTFs (**1c-g**) gave a good demonstration in which PyTTFs are potential compounds for OFET applications. The structural analyses clarified the effect of *N*-alkyl groups in the PyTTF system, which enhance not only solubility but also self-organizing ability in thin films suitable for FET operation. Molecules **1e-g**, which have long alkyl groups, tend to take 2-D molecular ordering both in the bulk single crystals and in the thin films, whereas **1c** and **1d** with relatively short alkyl groups also oriented layer-by-layer structure but have no efficient overlap of  $\pi$ -core. **1a** and **1b** did not form oriented structure. The present performance is not best among recently reported high performance solution-process OFETs (up to  $\mu_{\text{FET}} = 0.01 \text{ cm}^2/\text{Vs}$  on the **1g**). However, an important conclusion that can be drawn from the present study is that an appropriate combination of a  $\pi$ -conjugated core based on a small molecule with long alkyl groups can provide organic semiconductors capable of affording high-quality thin films with a well-organized 2-D molecular array.

### Experimental Procedures

**General.** All chemicals and solvents were of reagent grade unless otherwise indicated. DMF was distilled from  $\text{CaH}_2$  under reduced pressure. THF was distilled before use. Acetonitrile and hexane were distilled from  $\text{CaH}_2$  under  $\text{N}_2$  gas-flow. Trimethylphosphite was treated with sodium for 24 h, then distilled in an inert atmosphere onto activated molecular sieves 4 Å. *o*-Chloranil was recrystallized from toluene. NMR spectra were obtained in deuterated solvents with a JEOL Lambda 400 spectrometer operating at 400 MHz for  $^1\text{H}$  and at 100 MHz for  $^{13}\text{C}$  with tetramethylsilane as internal reference; chemical shifts ( $\delta$ ) were reported in parts per million. EI-MS spectra were obtained on a Shimadzu QP-5050A spectrometer using an electron impact ionization procedure (70 eV). MALDI-TOF-MS spectra were obtained on a Shimadzu KRATOS KOMPACT MALDI spectrometer. The molecular ion peaks of the sulfur-containing compounds showed a typical isotopic pattern, and all mass peaks are reported based on  $^{32}\text{S}$ .

#### Synthesis of *N*-alkyl-PyTTF:

**Bis(*N*-*n*-octylpyrrolo[3,4-*d*])tetrathiafulvalene (**1d**).** Bis(pyrrolo[3,4-*d*])tetrathiafulvalene (**1a**) (434 mg, 1.54 mmol) was dissolved in dry DMF (50 mL), cooled to 0 °C, and degassed by an argon stream for 15 min. 1-Bromooctane (2.19 g, 15.4 mmol) was added to the mixture, and then sodium hydride (0.485 g, 11.1 mmol) washed with dry hexane was added in one portion. The mixture was stirred for 1.5 h at 0 °C. Brine (200 mL) was added, and the resulting yellow precipitate was collected by filtration, washed with water, and dried in vacuo. The yellow solid was collected and purified by column chromatography (silica gel,  $\text{CH}_2\text{Cl}_2$ ) to give **1d** as a yellow solid ( $R_f = 0.7$ ). Recrystallization from hexane gave analytically pure **1d** as yellow needles (380 mg, 75%): mp 165.5- 166.5 °C;  $^1\text{H}$  NMR ( $\text{CDCl}_3$ )  $\delta = 0.87$  (t,  $J = 7.0$  Hz, 6H),

## 2. Development of Heteroaromatic-fused TTFs

1.26 (m, 20H), 1.71 (m, 4H), 3.79 (brs, 4H), 6.43 (s, 4H);  $^{13}\text{C}$  NMR (DMSO- $d_6$ )  $\delta$  = 13.9, 22.0, 25.9, 28.5, 30.8, 31.1, 49.8, 113.2, 116.5, 118.9; MS (EI, 70 eV)  $m/z$  = 506 ( $\text{M}^+$ ); Anal. calcd for  $\text{C}_{26}\text{H}_{38}\text{N}_2\text{S}_4$ : C, 61.61; H, 7.56; N, 5.53. Found: C, 61.60; H, 7.54; N, 5.54. CV:  $E_{ox}^{1/2}$  = +0.33 V, +0.75 V vs Ag/AgCl.

**Bis(*N-n*-dodecylpyrrolo[3,4-*d*])tetrathiafulvalene (1e).** The title compound was synthesized in a similar manner to **1d** to give yellow needles (hexane) in 61% yield: mp 126.5–127.5 °C;  $^1\text{H}$  NMR ( $\text{CDCl}_3$ )  $\delta$  = 0.88 (t,  $J$  = 7.0 Hz, 6H), 1.25 (m, 36H), 1.71 (m, 4H), 3.79 (brs, 4H), 6.43 (s, 4H);  $^{13}\text{C}$  NMR ( $\text{C}_6\text{D}_6$ )  $\delta$  = 14.4, 23.2, 26.7, 29.5, 29.9 ( $\times 2$ ), 30.08, 30.14 ( $\times 2$ ), 31.5, 32.4, 50.3, 112.3, 119.3, 120.8; MS (EI, 70 eV)  $m/z$  = 618 ( $\text{M}^+$ ); Anal. calcd for  $\text{C}_{34}\text{H}_{54}\text{N}_2\text{S}_4$ : C, 65.96; H, 8.79; N, 4.53. Found: C, 65.94; H, 9.08; N, 4.53. CV:  $E_{ox}^{1/2}$  = +0.34 V, +0.75 V.

**Bis(*N-n*-cetylpyrrolo[3,4-*d*])tetrathiafulvalene (1f).** A yellow powder from hexane; 79% yield; mp 120.0–121.0 °C;  $^1\text{H}$  NMR ( $\text{CDCl}_3$ )  $\delta$  = 0.88 (t,  $J$  = 6.8 Hz, 6H), 1.25 (m, 52H), 1.57 (m, 4H), 3.79 (brs, 4H), 6.49 (s, 4H);  $^{13}\text{C}$  NMR ( $\text{C}_6\text{D}_6$ )  $\delta$  = 14.4, 23.1, 26.7, 29.5, 29.9 ( $\times 2$ ), 30.08, 30.16 ( $\times 2$ ), 30.22 ( $\times 4$ ), 31.5, 32.4, 50.4, 112.3, 119.4, 120.8; MS (EI, 70 eV)  $m/z$  = 730 ( $\text{M}^+$ ); Anal. calcd for  $\text{C}_{42}\text{H}_{70}\text{N}_2\text{S}_4$ : C, 68.98; H, 9.65; N, 3.83. Found: C, 68.97; H, 9.69; N, 3.86. CV:  $E_{ox}^{1/2}$  = +0.33 V, +0.75 V.

**Bis(*N-n*-icosylpyrrolo[3,4-*d*])tetrathiafulvalene (1g).** A yellow powder from hexane; 53% yield; mp 120.7–121.7 °C;  $^1\text{H}$  NMR ( $\text{CDCl}_3$ )  $\delta$  = 0.88 (t,  $J$  = 6.8 Hz, 6H), 1.25 (m, 68H), 1.71 (m, 4H), 3.79 (t,  $J$  = 6.8 Hz, 4H), 6.43 (s, 4H);  $^{13}\text{C}$  NMR (100 MHz,  $\text{C}_6\text{D}_6$ )  $\delta$  = 14.3, 23.1, 26.8, 29.5, 29.82, 29.84, 30.05, 30.13 ( $\times 2$ ), 30.21 ( $\times 8$ ), 50.4, 112.3, 119.6, 120.9; MS (MALDI-TOF)  $m/z$  = 842.51 ( $\text{M}^+$ ); Anal. calcd for  $\text{C}_{50}\text{H}_{86}\text{N}_2\text{S}_4$ : C, 71.20; H, 10.28; N, 3.32. Found: C, 71.06; H, 10.25; N, 3.21. CV:  $E_{ox}^{1/2}$  = +0.34 V, +0.76 V vs Ag/AgCl.

### Synthesis forward to PyTTF:

**Potassium O-isopropyl dithiocarbonate (13).** KOH grains (22.4 g, 400 mmol) was placed into a 1,000 mL three-neck flask and dissolved in  $i$ PrOH (600 mL) with heating ca. 60 °C for 30 min. After the grains were dissolved completely, the solution was cooled down below 0 °C using ice-NaCl bath, and  $\text{CS}_2$  was added slowly over 10 min. Then the ice-bath are removed, the reaction mixture was stirred with a mechanical stirrer overnight (ca. 12 h). The resulting light-yellow solids were collected by filtration by ice-cooled  $i$ PrOH to give **13** (ca. 55 g, >80%).  $^1\text{H}$  NMR (400 MHz, DMSO- $d_6$ )  $\delta$  = 1.156 (d,  $J$  = 6.4 Hz, 6H), 5.450 (sept,  $J$  = 6.4 Hz, 1H).

**2-Oxo-1-methylpropyl O-isopropyl dithiocarbonate (14).** EtOH (500 mL) was pour into a 1,000 mL three-neck flask, and degassed by reducing pressure using water aspirator for 10 min. After an addition of **13** (24.2 g, 0.139 mol), the suspension was cooled down to 0 °C. 3-chloro-2-butanone (14.77 g, 14 mL, 0.139 mol) was added and allowed to stir overnight (ca. 16 h) at room temperature. The resulting mixture was filtrated ( $\times 2$ ) to remove the KOH salt. The filtrated solution was evaporated in vacuo and then re-dissolved in  $\text{CH}_2\text{Cl}_2$  (300 mL), which was washed with water (300 mL  $\times 3$ ), saturate NaCl aq (300 mL  $\times 1$ ), and dried with  $\text{MgSO}_4$ . Evaporation in vacuo gave **14** as orange oil (27.3 g, 95%).  $^1\text{H}$  NMR (400 MHz,  $\text{CDCl}_3$ )  $\delta$  = 1.394 (d,  $J$  = 6.3 Hz, 3H), 1.398 (d,  $J$  = 6.3 Hz, 3H), 1.470 (d,  $J$  = 7.3 Hz, 3H), 2.316 (s, 3H), 4.427 (q, 7.3 Hz, 1H), 5.729 (sept,  $J$  = 6.3 Hz, 1H).

**3,4-Dimethyl-1,3-dithiole-2-one (15).** Under  $\text{N}_2$  atmosphere, **14** (27.3 g, 0.132 mol) was added into conc.  $\text{H}_2\text{SO}_4$  (150 mL) at 0 °C before stirred for ca. 1.5 h at 75 °C. At the conclusion of the reaction, the mixture was cooled to room temperature and poured into ice (500 mL) and stirred for a while. The resulting black solution was extracted with  $\text{CH}_2\text{Cl}_2$  (200 mL  $\times 1$ , 100 mL  $\times 2$ ), combined organic phase was washed with water (200 mL  $\times 3$ ), saturated NaCl aq (200 mL), then dried with  $\text{MgSO}_4$ . After evaporation distillation under reduced pressure (135 °C, 12 mmHg) afforded **15** as colorless crystals (18.1 g, 94 %).  $^1\text{H}$  NMR (60 MHz)  $\delta$  = 2.12 (s).

**4,5-Bis(bromomethyl)-1,3-dithiole-2-one (16).** Under  $\text{N}_2$  atmosphere, **15** (14.6 g, 100 mmol) and NBS (35.6 g, 200 mmol) was placed in a 100 mL three-neck flask with  $\text{CCl}_4$  (50 mL), was irradiated with halogen lamp for ca. 1 h. The resulting mixture was evaporated to remove the  $\text{CCl}_4$  and dissolved in  $\text{CH}_2\text{Cl}_2$ . The solution was washed with saturated  $\text{NaHCO}_3$  aq (400 mL  $\times 1$ ), water (300 mL  $\times 3$ ) and sat. NaCl aq (300 mL  $\times 2$ ), it was dried with  $\text{MgSO}_4$ . Recrystallization from  $\text{CHCl}_3$ /hexane gave **16** as white solids (1st crystallization.: 14.5 g, 48 %, 3rd and 4th crystallization.: 2.91 g, 10 %, total: 17.4 g, 57 %).  $^1\text{H}$  NMR (400 MHz)  $\delta$  = 4.39 (s).

**4,6-Dihydro-*N*-tosyl-(1,3)-dithiole[4,5-*c*]pyrrole-2-one (12).** Under nitrogen atmosphere, **16** (9.12 g, 30 mmol) was dissolved in DMF (600 mL) and deaerated by argon stream for 10 min. Finely ground sodium tosylamide (12.2 g, 63 mmol) was added into the solution at 0 °C: the resulting solution immediately turned yellow in color. After 10 min, ice-bath was removed, and the solution was stirred for additional 50 min at room temperature. Then the solution was poured into saturated NaCl aqueous solution (1 L), whereupon a precipitated solid was collected by filtration and washed with water. The solid dried in vacuo was dissolved into  $\text{CH}_2\text{Cl}_2$ , and the solution was filtrated to remove impurity and then purified by column chromatography (silica-gel,  $\text{CH}_2\text{Cl}_2$ ,  $\Phi$  6 cm  $\times$  6 cm,  $R_f$  = 0.4) to give a practically pure sample as white solid (7.10 g, 76 %). Mp 175.6–176.2 °C (174.0–174.5 °C $^{\text{S}2}$ );  $^1\text{H}$  NMR (400 MHz,  $\text{CDCl}_3$ )  $\delta$  =

2.45 (s, 3H), 4.49 (s, 4H), 7.37 (d,  $J = 8.2$  Hz, 2H), 7.75 (d,  $J = 8.2$  Hz, 2H); MS (EI, 70 eV)  $m/z = 313$  ( $M^+$ ); IR (KBr)  $\nu = 1694$   $\text{cm}^{-1}$  (C=O).

***N*-tosyl-1,3-dithiolo[4,5-*c*]pyrrolo-2-one (17).** Synthesis of 17 with DDQ was carried out according to paper with 97%.<sup>99</sup> Here synthesis of 17 with cheaper *o*-chloranil reagent are described. Under nitrogen atmosphere, a mixture of 12 (5.33 g, 17 mmol) and *o*-chloranil (20.9 g, 85 mmol) in *o*-dichlorobenzene (40 mL) was stirred at 195 °C until all the starting material was consumed (ca. 1.5 h). The reaction mixture was concentrated in vacuo, and the resulting solid was dissolved in  $\text{CH}_2\text{Cl}_2$  (100 mL) and filtrated through a Celite pad (1.5 cm). The filtrate was washed consecutively with 10 % sodium hydroxide aqueous solution (200 mL  $\times$  2) and saturated NaCl aqueous solution (200 mL  $\times$  3), and then dried over  $\text{MgSO}_4$ . 17 was purified by column chromatography (silica-gel,  $\text{CH}_2\text{Cl}_2$ ,  $\Phi$  6 cm  $\times$  5 cm,  $R_f = 0.5$ ) and recrystallization from toluene/hexane as a white solid (4.02g, 76 % up to the second crops). Mp 179.3–179.8 °C (178.5–179.0 °C<sup>S2</sup>);  $^1\text{H}$  NMR (400 MHz,  $\text{CDCl}_3$ )  $\delta = 2.44$  (s, 3H), 7.23 (s, 2H), 7.34 (d,  $J = 8.4$  Hz, 2H), 7.79 (d,  $J = 8.4$  Hz, 2H); MS (EI, 70 eV)  $m/z = 311$  ( $M^+$ ); IR (KBr)  $\nu = 1716$   $\text{cm}^{-1}$  (C=O).

**OFET Device Fabrication.** Fabrication of OFET devices was carried out in ambient conditions. Top-contact OFET devices were fabricated on a heavily doped  $n^+$ -Si (100) wafer, with a 200 nm thermally grown  $\text{SiO}_2$  ( $C_i$ ) 17.3 nF  $\text{cm}^{-2}$ ) as dielectric layer. A semiconductor layer was deposited on the substrate by spin-coating for soluble compounds (1c - 1g) and by vacuum-deposition ( $\sim 3 \times 10^{-3}$  Pa) for insoluble compounds (1a - 1b). Toluene was used as the spin-coating solvent except for *n*-icosyl PyTTF (1g) which was dissolved in hot chlorobenzene ( $\sim 80$  °C) due to relatively low solubility. On top of the organic thin-films gold (80 nm thick) was deposited through a shadow mask. Characteristics of the OFET devices were measured at room temperature in air, and  $\mu_{\text{FET}}$  was extracted from a drain current ( $I_d$ ) of transfer characteristics in saturation regime using the equation

$$I_d = (WC_i/2L) \mu_{\text{FET}} (V_g - V_{\text{th}})^2$$

where  $C_i$  is the capacitance of the  $\text{SiO}_2$  insulator, and  $V_g$  and  $V_{\text{th}}$  are the gate and threshold voltages, respectively.

For devices based on P3HT, commercial poly(3-hexylthiophene) (purchased from Aldrich) was used for device fabrication. 0.5 wt% solution of P3HT in chlorobenzene was spun on the OTS-treated Si/SiO<sub>2</sub> substrates (1000 rpm, 30 sec.), followed by the same procedure.<sup>32</sup> The FET characteristics are shown in Figure 2.2.9.

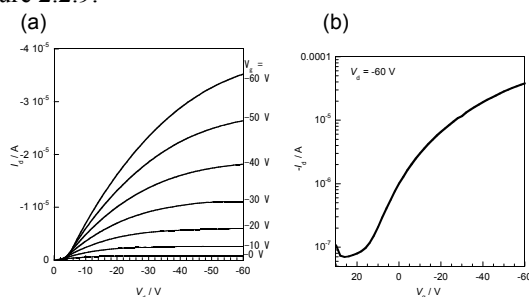


**Figure 2.2.9.** FET characteristics of spin-coated rrP3HT on bare Si/SiO<sub>2</sub> substrates. Typical extracted  $\mu_{\text{FET}}$  is ca. 0.02  $\text{cm}^2/\text{Vs}$ .

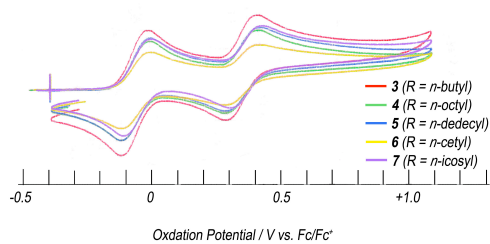
**Solubility Determination.** To a precisely weighed sample (ca. 5 or 10 mg), toluene was added in increments of 0.1 mL, and the resulting mixture was shaken and sonicated at room temperature (20-25 °C). The total amount of toluene required to dissolve the entire solid sample was converted into solubility (g/L)

**X-ray Diffraction (XRD) Measurements.** XRD measurements of thin films fabricated on the Si/SiO<sub>2</sub> substrate were obtained with a Rigaku RINT 2200 diffractometer with a Cu KR source ( $\lambda = 1.541$  Å) in air. The  $d$ -spacings were calculated by the Bragg equation:  $\lambda = 2d\sin\theta$ . Single-crystal X-ray structural analyses were conducted on a Rigaku Rapid-S Imaging Plate (Mo  $K\alpha$  radiation,  $\lambda = 0.71069$  Å, graphite monochromator,  $T = 200$  K, and  $2\theta_{\text{max}} = 55.0^\circ$ ) for 1c-f, and on a Rigaku MSC Mercury CCD (Mo  $K\alpha$  radiation,  $\lambda = 0.71075$  Å, graphite monochromator,  $T = 294$  K,  $2\theta_{\text{max}} = 55.0^\circ$ ) for 1a. Detail crystallographic data are shown in Table A1 (in Appendix). The structure was solved by direct methods (SIR92)<sup>106</sup>. Non-hydrogen atoms were refined anisotropically, and hydrogen atoms were included in the calculations but not refined.<sup>107</sup> All calculations were performed using the crystallographic software package TeXsan.<sup>108</sup>

**Cyclic voltammetry (CVs).** CVs were recorded on a Hokuto Denko HA-301 potentiationstat and a Hokuto Dneko HB-104 function generator in benzonitrile containing tetrabutylammonium hexafluorophosphate (TBAPF6, 0.1 M) as the supporting electrolyte, at a scan rate of 100 mV/s. Counter and working

## 2. Development of Heteroaromatic-fused TTFs

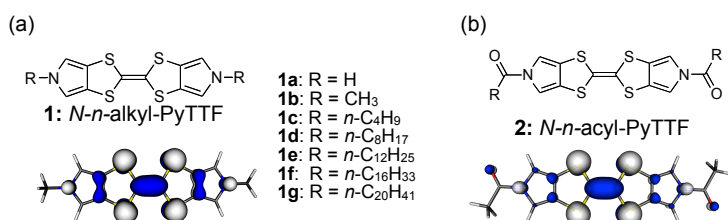
electrodes were made of Pt, and the reference electrode was Ag/AgCl. Cyclic voltammograms of **1c-g** are shown in Figure 2.2.10. Oxidation potentials of **1c-g** were identical with in experimental error (Figure 2.2.10 and Table 2.2.4). **1a** showed slightly lower oxidation potential than those of **1c-g**.



**Figure 2.2.10.** Cyclic voltammograms of **1c-g**.

	oxidation potential <sup>a</sup> / V		
	onset	$E^1_{1/2}$	$E^2_{1/2}$
<b>1a</b>	-0.15	-0.06	0.39
<b>1c-g</b>	-0.18	-0.11	0.31

<sup>a</sup> vs. Fc/Fc<sup>+</sup>.

2.3 Bis(*N*-acyl-pyrrole[3,4-*d*])tetrathiafulvalenes (*N*-acyl-PyTTFs)

**Figure 2.3.1.** Structures of (a) *N*-alkyl- and (b) *N*-acyl-PyTTFs with the calculated HOMOs by DFT method (B3LYP/6-31G(d)).<sup>111</sup> The calculated HOMO energy levels are ca. -4.2 eV for **1** and -4.9 eV for **2**.

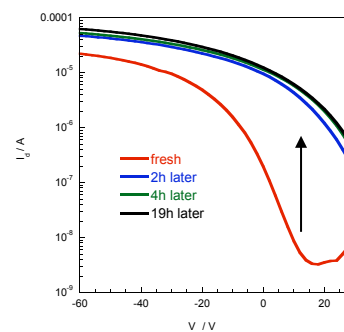


**Figure 2.3.2.** FET characteristics of *N*-*n*-icosyl-substituted PyTTF (**1g**), R = *n*-C<sub>20</sub>H<sub>41</sub>) depending on the duration of exposure to ambient conditions.

**Introduction.** *N*-alkyl-substituted TTF were successfully developed as solution-processible semiconductors, as described in section 2.2 (**1**, Figure 2.3.1a). The fabricated FET devices with the spin-coated thin-films of **1g** showed  $\mu_{\text{FETS}}$  as high as 0.01 cm<sup>2</sup>/Vs in air. Although their FET performances were relatively good for solution-processed OFETs without intensive optimization in device fabrication, their sensitivity to ambient air was a severe drawback: shortly after exposure to air, off-current of the OFETs rose significantly (Figure 2.3.2). The poor stability in air is likely due to their low oxidation potentials ( $E^{1/2} = -0.11$  V vs. Fc/Fc<sup>+</sup>), in other words, the higher-lying energy level of the highest molecular occupied orbital (HOMO) makes **1** susceptible to air oxidation.<sup>109,110</sup>

In order to stabilize **1**-based organic semiconductors, I intended to introduce electron-withdrawing groups on the nitrogen atom instead of rather electron-donating *N*-alkyl groups. Molecular orbital calculations predicted that *N*-acyl-substituted PyTTFs (**2**) would have a lower HOMO energy level than that of **1** with keeping the large HOMO coefficients on the sulfur atoms (2.3.1b).<sup>111</sup> In this section, I describe the synthesis of *N*-acyl-PyTTFs and the characteristics of FET devices using their vapor-deposited thin-films.

**Synthesis and Characterization.** The *N*-alkylation of the parent PyTTF (**1a**) was easily done by the reaction of **1a** with alkyl halide in the presence of sodium hydride.<sup>15</sup> Analogously, introduction of acyl substituents on **1a** was first attempted under a similar condition using acyl chloro-

**Scheme 2.3.1.** Synthesis of **2**. The yields are described in Table 2.3.1.

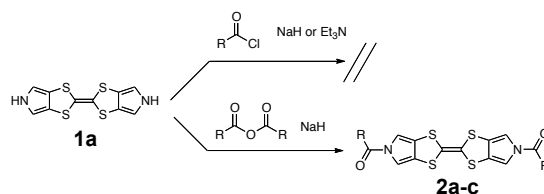


**Table 2.3.1.** Properties of synthesized **2a-c**.

R		yield / %	solubility / g L <sup>-1</sup>	sublimation at ~10 <sup>-3</sup> Pa
<b>2a</b>	CH <sub>3</sub> methyl	60	<10 <sup>-4</sup>	✓
<b>2b</b>	<i>n</i> -C <sub>5</sub> H <sub>11</sub> hexanoyl	56	0.010	✓
<b>2c</b>	<i>n</i> -C <sub>12</sub> H <sub>25</sub> dodecanoyl	74	0.002	-

in toluene at r.t.

## 2. Development of Heteroaromatic-fused TTFs

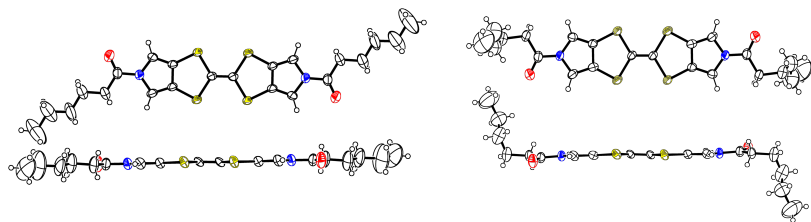


**Figure 2.3.3.** Molecular structure of **2b** in the single crystal. Two crystallographically independent molecules exist.

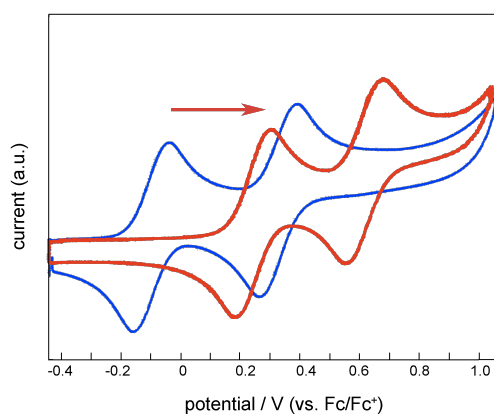


**Figure 2.3.4.** Cyclic voltammograms of (blue line) *N*-alkylated-PyTTF (**1c-g**) and (red line) *N*-hexanyl-PyTTF (**2b**).

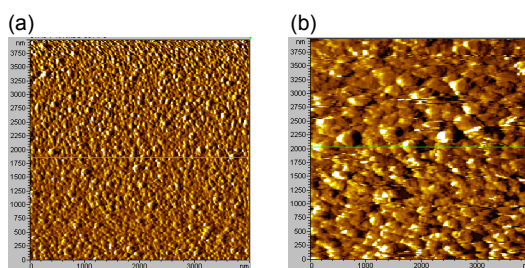


**Figure 2.3.5.** AFM images of evaporated thin films of (a) **2a** on HMDS-treated substrate and (b) **2b** on ODTS-treated substrate ( $T_{\text{sub}} = \text{rt}$ ).

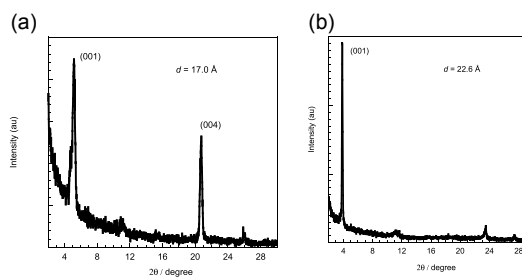


**Figure 2.3.6.** XRD patterns of evaporated thin films of **2a** on HMDS-treated substrate (a) and **2b** on ODTS-treated substrate (b) ( $T_{\text{sub}} = 100\text{ }^{\circ}\text{C}$ ).

rides. The reaction, however, gave a complex mixture, and the acylated **2** was not isolated. Concurrent hydrochloric acid may react with the TTF part, inducing decomposition of the TTF framework. Instead of acyl chloride, the use of acid anhydrides turned out to give **2** successfully in reasonable isolated yields (Scheme 2.3.1). Thus, *N*-acetyl- (**2a**), *n*-hexanoyl (**2b**), and *n*-dodecanoyl-PyTTF (**2c**) were obtained. All new derivatives were fully characterized by spectroscopic and combustion analyses.

Unambiguous structural determination of *N*-*n*-hexanoyl derivative **2b** was achieved by single-crystal X-ray analysis (see Experimental Procedures for detail). In the crystal structure, two crystallographically independent molecules exist (Figure 2.3.3). Although the conformations of *n*-C<sub>5</sub>H<sub>11</sub> chains in two molecules are different, the central core parts of the molecules are similar to each other: the carbonyl moieties are in the same plane that the PyTTF part defines, indicating that the conjugation effectively extends to the *N*-acyl moieties.

**Oxidation Potential.** Cyclic voltammograms of **2** showed two reversible oxidation couples typical for the TTF derivatives (Figure 2.3.4). As expected, the oxidation peaks of **2a-c** ( $E_{1/2}^{1/2} = +0.25\text{ V vs. Fc/Fc}^+$ ) were shifted positively by more than 0.35 V compared with those of *N*-

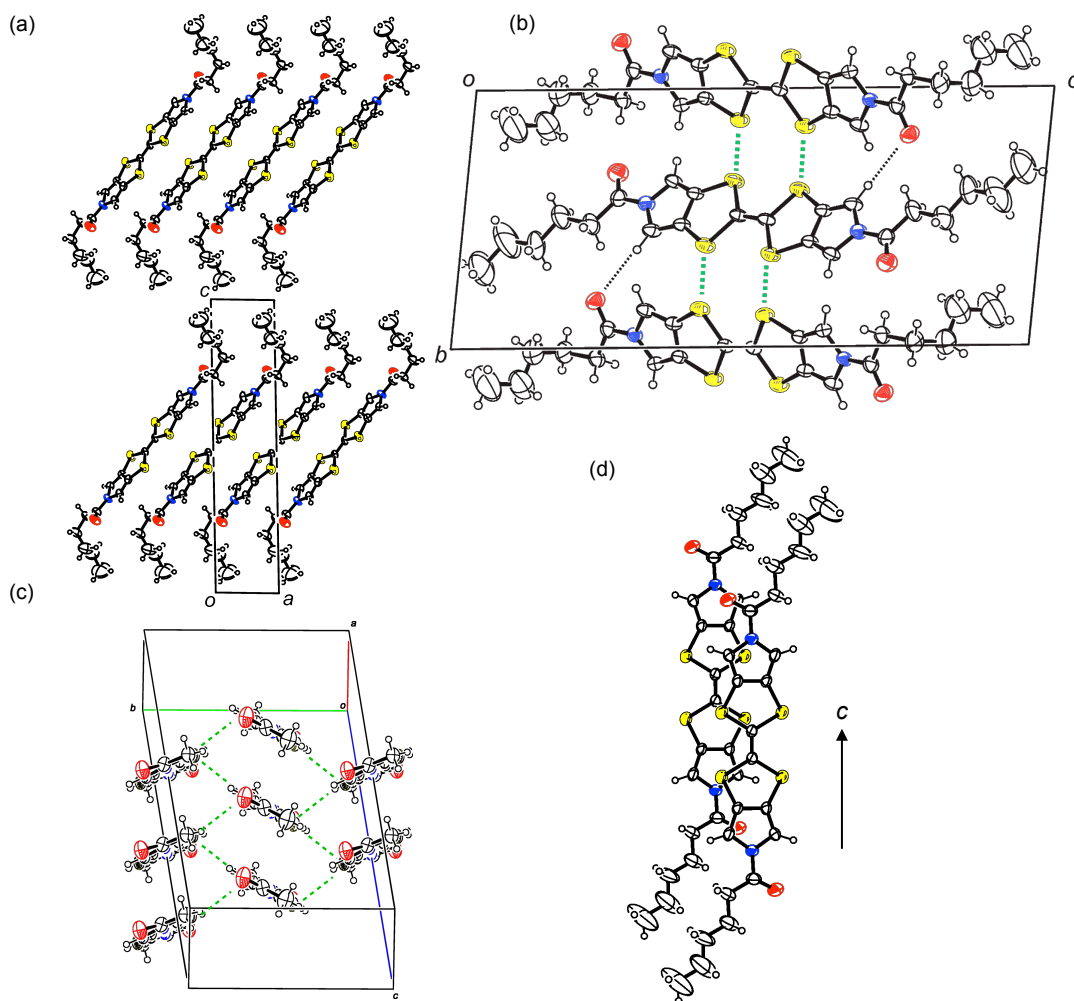


**Figure 2.3.7.** Molecular arrangement of **2b** in crystal. (a) *b*-Axis projection to show layer-by-layer structure along *c*-axis. (b) *a*-axis projection. Stacking columnar structure along the *a*-axis. Black dash lines show inter columnar hydrogen bond like C=O...H-C contacts (2.62 Å). Green dash line show S-S inter columnar contacts shorter than the sum of Van der Waals radii (3.40 ~ 3.57 Å). (c) Molecular long-axis projection to show many S-S contacts (d) View along normal to the  $\pi$ -plane. Overlap of  $\pi$ -core appears small.

alkyl-PyTTFs (**1c-g**), indicating a significant decrease of the energy level of the HOMO ( $E_{\text{HOMO}}$ ). The  $E_{\text{HOMO}}$ s of **2a-c** were estimated from the onset of first oxidation waves ( $E_{\text{onset}} = +0.15$  V) to give  $E_{\text{HOMO}} = -4.95$  eV below the vacuum level, which is almost comparable with that of DT-TTF ( $E_{\text{HOMO}} = -4.98$  eV).<sup>112,113</sup>

**Solubility and Fabrication of Thin-Films, and their Morphologies.** In contrast to the highly soluble *N*-alkyl-PyTTFs (**1c-g**), the solubilities of *N*-acyl-PyTTFs (**2a-c**) even with the long alkyl chains were very poor: the solubilities in toluene at room temperature were 0.01 g/L for **2b** and 0.002 g/L for **2c**, which were lower than those of **1c-g** by more than two orders of magnitude. Although the reason for extremely low solubility of **2a-c** are not clear, I speculate that incorporation of the electron-negative carbonyl groups in the conjugation of PyTTF core and thus induced planer and rigid molecular structure confirmed by X-ray structural analysis.

Poor solubility of **2a-c** in organic solvents prevented deposition of thin-films by solution-process. Instead, vacuum-deposition of **2a-c** gave homogeneous thin-films with metallic luster on Si/SiO<sub>2</sub> substrates except for **2c**, which thermally decomposed during the deposition. The thin-films consist of well-ordered polycrystalline grains as confirmed by the atomic force mi-

croscopy (AFM) images (Figure 2.3.5). Such morphology is generally a prerequisite for high-performance OFETs.<sup>114-116</sup>

The XRD measurements of the thin-films of **2a** and **2b** indicate that the films have crystalline order in the direction of the substrate normal (Figure 2.3.6). The calculated interlayer distances (*d*-spacing) are 17.0 Å for **2a** and 22.6 Å for **2b**. The *d*-spacing of **2b** is almost the same as the length of the crystallographic *c*-axis in the bulk single crystal, which suggests that molecular arrangements in the thin-film and in the bulk single-crystal are similar to each other.

**Molecular Arrangement in the Bulk Single-Crystal.** The molecular arrangement of *N*-hexanoyl-PyTTF (**2b**) consists of layer-by-layer structure along crystallographic *c*-axis as seen in the structures of the long alkyl-substituted PyTTFs (Figure 2.3.7a). The overlap of  $\pi$ -cores is relatively small (Figure 2.3.7d). However, all four sulfur atoms in the TTF core contact with those of the neighboring molecules, indicating strong intermolecular interactions via S-S contacts (Figure 2.3.7b and c). Although all hydrogen atoms are not refined analytically, the hydrogen bond like intermolecular interaction between the pyrrole-H and the acyl-C=O are present, which may contribute the dense packing between the TTF cores.

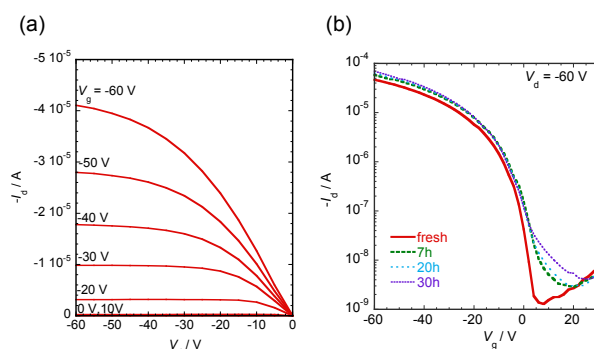


**Figure 2.3.8.** FET characteristics of **2b**-based OFETs. (a) Output characteristic. (b) Transfer characteristics with the dependence of duration of exposure to the ambient conditions.

**Table 2.3.2.** FET characteristics of **2a**- and **2b**-based devices<sup>a</sup>.

compd	substrate <sup>b</sup>	$T_{\text{sub}} / ^\circ\text{C}$	$\mu_{\text{FET}} / \text{cm}^2 \text{V}^{-1} \text{s}^{-1}$	$I_{\text{on}}/I_{\text{off}}$	$V_{\text{th}} / \text{V}$
<b>2a</b>	HMDS	rt	$2.5 \times 10^{-2}$	$10^4$	-25
		60	$6.4 \times 10^{-4}$	$5 \times 10^3$	1.0
		100	$5.2 \times 10^{-2}$	$10^3$	-11
	OTS	rt	$5.1 \times 10^{-4}$	$10^4$	-8.0
		60	$5.5 \times 10^{-3}$	$10^4$	-8.0
		100	$2.1 \times 10^{-3}$	$10^3$	3.0
	ODTS	rt	$1.8 \times 10^{-4}$	$10^3$	1.0
		60	$6.9 \times 10^{-2}$	$5 \times 10^4$	-14
		100	$3.7 \times 10^{-3}$	$5 \times 10^2$	2.0
<b>2b</b>	HMDS	rt	$2.2 \times 10^{-2}$	$5 \times 10^3$	-15
		60	$2.2 \times 10^{-2}$	$10^4$	-7.0
		100	$6.8 \times 10^{-2}$	$10^4$	-8.0
	OTS	rt	$3.3 \times 10^{-2}$	$10^4$	-10
		60	$7.6 \times 10^{-2}$	$10^5$	-3.0
		100	$6.2 \times 10^{-2}$	$5 \times 10^4$	-2.0
	ODTS	rt	$1.5 \times 10^{-2}$	$10^4$	-11
		60	$4.4 \times 10^{-2}$	$5 \times 10^5$	-9.0
		100	$8.1 \times 10^{-2}$	$5 \times 10^5$	-4.0

<sup>a</sup> Top-contact configuration with  $W$  and  $L$  were 1500  $\mu\text{m}$  and 50  $\mu\text{m}$  respectively. <sup>b</sup>  $\text{SiO}_2$  surface were treated with alkylsilyl reagents. See Experimental Procedures.

**FET characteristics.** On the top of the evaporated thin-films, gold source and drain electrodes were thermally deposited through a shadow mask to define the channel of the transistors with a length ( $L$ ) of 50 or 100  $\mu\text{m}$  and width ( $W$ ) of 1.5 mm, respectively. The OFET devices were evaluated under ambient conditions, and the **2a**- and **2b**-based devices showed normally-off FET characteristics (Figure 2.3.8). Extracted FET mobilities from the saturation regime are up to 0.05  $\text{cm}^2/\text{Vs}$  for **2a**-based devices and 0.08  $\text{cm}^2/\text{Vs}$  for **2b**-based devices, respectively (Table 2.3.2).

As already mentioned, the **1g**-based OFETs suffered from severe air-oxidation: although the fresh device showed typical normally-off FET characteristics, off-current increased significantly after exposure to air for 2 h by more than two orders of magnitude (Figure 2.3.2). In contrast, the present **2a**- and **2b**-based devices show improved air-stability. As shown in Figure 2.3.8b, the devices showed typical normally-off FET responses even after exposure to ambient lab conditions for more than 30 h. This stabilization can be accounted for the lowered HOMO energy level of **2** caused by introduction of the electron-withdrawing acyl groups on the PyTTF core.

**Summary.** I successfully synthesized *N*-acyl-PyTTFs (**2**) and evaluated the FET devices based on their vapor-deposited thin-films. The electron-withdrawing acyl groups introduced brought about lower HOMO energy level than those of *N*-alkyl-PyTTFs (**1c-g**), which contributes to stabilization of **2a** and **2b**-based FET devices under ambient conditions without degrading the FET characteristics. These results indicate that the tuning of the energy level of HOMO is important in developing air-stable p-channel organic semiconductors.

## Experimental Procedures

**General:** All chemicals and solvents are of reagent grade unless otherwise indicated. DMF was distilled from  $\text{CaH}_2$  under reduced pressure. Melting points were measured with Yanaco MR approximately. Nuclear magnetic resonance spectra were obtained in deuterated chloroform with a JEOL Lambda 400 spectrometer operating at 400 MHz for  $^1\text{H}$  and 100 MHz for  $^{13}\text{C}$  or a JEOL EX 270 spectrometer operating at 270 MHz for  $^1\text{H}$  and 68 MHz for  $^{13}\text{C}$  with TMS as internal reference; chemical shifts ( $\delta$ ) are reported in parts per million. EI-MS spectra were obtained on a Shimadzu QP-5050A spectrometer using an electron impact ionization procedure (70 eV). The molecular ion peaks of the sulfur-containing compounds showed a typical isotopic pattern, and all the mass peaks are reported based on  $^{32}\text{S}$ .

### Synthesis of *N*-acyl-PyTTFs:

**Bis(*N*-methylpyrrolo[3,4-*d*])tetrathiafulvalene (**2a**).** Under  $\text{N}_2$  atmosphere, anhyd DMF (30 mL) solution of **1a** (1 mmol) in a 100 mL round-bottom flask was degassed by  $\text{N}_2$  stream for 15 min. Acetic anhydride (7.7 mL, 7 mmol) was added, subsequently sodium hydride (168 mg, 7 mmol, washed with hexane) was added in one portion at 0  $^\circ\text{C}$ . The yellow forming solution was allowed to continue stirring for approximately 18 h. The resulting mixture was poured into brine (100 mL) and filtrated with water, then dried in a decicator. The solid was washed with MeOH to give a analytically pure compound of **2a** (298 mg, 81 %). Sample for device fabrication was purified by sublimation under reduced pressure: cold-finger sublimation gave 98 mg from 238 mg (41 %), and subsequent temperature-gradient vacuum sublimation to give yellow crystals (40 mg from 72 mg (56 %)). Mp > 300  $^\circ\text{C}$ ;  $^1\text{H}$  NMR (270 MHz,  $\text{DMSO-}d_6$ , 35  $^\circ\text{C}$ )  $\delta$  = 1.358 (s), 7.479 (s); MS (EI, 70 eV)  $m/z$  = 366 ( $\text{M}^+$ ), 324 ( $\text{M}^+ - \text{COCH}_2$ ), 282 ( $\text{M}^+ - (\text{COCH}_2)_2$ ); IR (C=O) 1708  $\text{cm}^{-1}$ ; Anal. calcd for  $\text{C}_{14}\text{H}_{10}\text{N}_2\text{O}_2\text{S}_4$ : C, 45.88, H, 2.75, N, 7.64%. Found for C, 45.86; H, 2.75; N, 7.64%.

**Bis(*N*-*n*-hexanoylpyrrolo[3,4-*d*])tetrathiafulvalene (**2b**).** Under  $\text{N}_2$  atmosphere, **1a** (0.5 mmol) in a 50 mL round-bottom flask was dissolved in anhyd DMF (30 mL), cooled to 0  $^\circ\text{C}$ , and degassed by argon stream for 15 min. Hexanoic anhydride (1.07 g, 1.16 mL, 5 mmol) was added, and then sodium hydride (120 mg, 5 mmol, washed with hexane) was added in one portion. The foaming, yellow mixture was stirred for 1 h at 0  $^\circ\text{C}$  and then allowed to warm up to room temperature. The mixture was poured into brine (150 mL). The formed sticky and olive-color precipitates were collected by filtration, and washed with water, and then dried in a decicator. The olive-color solids were dissolved in heated  $\text{CHCl}_3$  and filtrated using a celite (1 cm) in hot. Recrystallization from  $\text{CHCl}_3$  gave **16** as olive-color solids (133 mg, 56 %). Higher purified sample was obtained by temperature-gradient vacuum sublimation (source temperature: 220  $^\circ\text{C}$  under  $\sim 10^{-3}\text{Pa}$ ) as yellow solids (83 mg from 127 mg, yield of sublimation: 65 %). Mp. 166.7 - 168.2 (with decomposition);  $^1\text{H}$  NMR (400 MHz,  $\text{CDCl}_3$  at 50 $^\circ\text{C}$ )  $\delta$  = 0.917 (t,  $J$  = 6.8 Hz, 6H),

1.3568/1.3653/1.3745/1.3812/1.3928 (m, 7H), 1.772 (t,  $J = 7.4$  Hz, 4H), 2.715 (t,  $J = 7.4$  Hz, 4H), 7.109 (bs, 4H);  $^{13}\text{C}$  NMR (400 MHz,  $\text{CDCl}_3$  at  $50^\circ\text{C}$ )  $\delta = 14.0, 22.5, 24.5, 34.3, 52.0, 109.7, 121.3, 126.7$ ; MS (EI, 70 eV)  $m/z = 478$  ( $\text{M}^+$ ), 380 ( $\text{M}^+ - \text{COC}_5\text{H}_{11}$ ), 282 ( $\text{M}^+ - 2 \times \text{COC}_5\text{H}_{11}$ ): Anal. calcd for  $\text{C}_{22}\text{H}_{26}\text{N}_2\text{O}_2\text{S}_4$ : C, 55.20; H, 5.47; N, 5.85; S, 26.79%. Found: C, 55.02; H, 5.58; N, 6.12; S, 26.67%. IR  $1699\text{ cm}^{-1}$ .

**Bis(*N-n*-dodecanoyl[3,4-*d*])tetrathiafulvalene (2c).** Under  $\text{N}_2$  atmosphere, anhyd DMF (50 mL) solution of a **1a** (0.5 mmol) in a 100 mL round-bottom flask was degassed by argon stream for 15 min. Lauric anhydride (1.34 g, 3.5 mmol) was added and the vessel was warmed up ( $\sim 40^\circ\text{C}$ ) to dissolve the reagent, then cooled to room temperature before sodium hydride (84 mg, 3.5 mmol, washed with hexane) was added in one portion. The foaming and yellow mixture was stirred for 3 h at room temperature. After addition of sodium hydride ( $\sim 80$  mg) it was allowed to stir overnight (ca. 16 h) at room temperature. The resulting forming and yellow reaction mixture was poured into brine (100 mL) and filtrated with water, and then the solids were dried in a decicator. The yellow solids were reprecipitated from  $\text{PhCl}$  / hexane, and pass through flash column-chromatography in hot (silite - silica-gel – silite three layers,  $\text{CHCl}_3$ ) followed by recrystallization from  $\text{PhCl}$  to give yellow crystals (238 mg, 74%). Mp.  $147.7 - 149.6^\circ\text{C}$ ;  $^1\text{H}$  NMR (270 MHz,  $\text{CDCl}_3$ , at  $50^\circ\text{C}$ )  $\delta = 0.880$  (t,  $J = 6.7$  Hz, 6H), 1.269 (m), 1.763 (t,  $J = 6.9$  Hz, 3H), 2.712 (t,  $J = 7.1$  Hz, 3H), 7.107 (s, 3H); MS (EI, 70eV)  $m/z = 646$  ( $\text{M}^+$ ); IR (KBr)  $1697\text{ cm}^{-1}$ ; Anal. calcd for  $\text{C}_{34}\text{H}_{50}\text{N}_2\text{O}_2\text{S}_4$ : C, 63.11; H, 7.79, N, 4.33. Found for C, 63.11, H, 7.62, N, 4.31.

**Lauric anhydride (Dodecanoic anhydride) ( $\text{CH}_3(\text{CH}_2)_{10}\text{CO}_2\text{O}$ ).** A mixture of lauric anhydride (5.01 g, 0.25 mmol) and acetic anhydride (5.01 g, 50 mmol, 4.7 mL) was refluxed over 2 h. Then the leaving acetic anhydride and forming acetic acid were distilled out under atmospheric pressure and then reduce pressure at  $\sim 170^\circ\text{C}$ . A white solid, obtained by cooling down the remaining solution to room temperature, was recrystallized from  $\text{Et}_2\text{O}$  (room temperature  $\rightarrow \sim 50^\circ\text{C}$ ). Lauric anhydride was collected by filtration using a Büchner funnel and washing with cooled  $\text{Et}_2\text{O}$  as colorless plates (4.31 g, 90 %).  $^1\text{H}$  NMR (270 MHz,  $\text{CDCl}_3$ )  $\delta = 0.879$  (t,  $J = 6.4$  Hz, 6H), 1.258 (m, 32 H), 1.655 (quint,  $J = 7.2$  Hz, 4.2H), 2.441 (t,  $J = 7.4$  Hz, 4H);  $^{13}\text{C}$  NMR (400 MHz,  $\text{CDCl}_3$ )  $\delta = 14.2, 22.8, 24.3, 29.0, 29.4, 29.5, 29.68, 29.70, 32.0, 35.4$ ; mp  $42.0 - 42.5^\circ\text{C}$ ; MS (EI, 70eV)  $m/z = 382$  ( $\text{M}^+$ ,  $< 1\%$ ), 183 ( $\text{C}_{11}\text{H}_{23}\text{CO}^+$ , 100 %).

**X-ray diffraction (XRD) measurement of thin-films and single-crystal.** XRD patterns of spin-coated thin films deposited on  $\text{Si}/\text{SiO}_2$  substrates were obtained with a Rigaku RiNT-2200 diffractometer with a  $\text{Cu K}\alpha$  source ( $\lambda = 1.541 \text{ \AA}$ ) in air. The  $d$ -spacings were calculated by the bragg equation:  $\lambda = 2d\sin\theta$ . Single crystals of *N-n*-hexanoyl-PyTTF (**2b**) suitable for structural analysis were obtained by vapor sublimation. The single-crystal analysis was made on Rigaku MSC Mercury CCD. The structure was solved by direct methods (SIR92).<sup>106</sup> Non-hydrogen atoms were refined anisotropically, and hydrogen atoms were included in the calculations but not refined.<sup>107</sup> All calculations were performed using the crystallographic software package TeXsan.<sup>108</sup> Detailed condition and crystallographic data are listed in Table A1 (in Appendix).

**Cyclic voltammograms (CVs).** CVs were recorded on a Hokuto Denko HA-301 potentiostat and a Hokuto Denko HB-104 function generator in dichloromethane containing tetrabutylammonium hexafluorophosphate ( $\text{Bu}_4\text{NPF}_6$ , 0.1 M) as supporting electrolyte at a scan rate of 100 mV/s. Counter and working electrodes were made of Pt, and the reference electrode was  $\text{Ag}/\text{AgCl}$ . All the potentials were calibrated with the standard ferrocene/ferrocenium redox couple ( $E^{1/2} = +0.46\text{ V}$  measured under identical conditions). Oxidation potentials of **2a–2c** were identical with in experimental error.

**Atomic Force Microscopy (AFM).** The AFM images were measured with a Molecular Imaging PicoPlus microscope in air.

**Device fabrications and evaluations.** OFETs were fabricated in a top-contact configuration on a heavily doped  $n^+$ -Si (100) wafer with 200-nm-thick thermally grown  $\text{SiO}_2$  ( $C_i = 17.3\text{ nF cm}^{-2}$ ). The surface of the  $\text{SiO}_2$  dielectrics was treated with silane-based self-assembled monolayer (SAM) reagents with following methods; the substrates with an octyltrichlorosilane (OTS)- or octadecyltrichlorosilane (ODTS)- was obtained by immersing the  $\text{Si}/\text{SiO}_2$  substrate in 0.1 M OTS or ODTS in toluene at  $60^\circ\text{C}$  for 20 min. HMDS (hexamethyldisilazane)-treatments were carried out by exposing the  $\text{SiO}_2$  to HMDS vapor at room temperature in a box under nitrogen for 12 h. A thin film (50 nm thick) of *N*-acetyl- (**2a**) or *N-n*-hexanoyl-PyTTF (**2b**) as the active layer was vacuum-deposited on the  $\text{Si}/\text{SiO}_2$  substrates under a pressure of  $\sim 2 \times 10^{-3}$  Pa. Substrate temperature ( $T_{\text{sub}}$ ) was varied at rt,  $60^\circ\text{C}$ , and  $100^\circ\text{C}$ . Deposition rate was  $\sim 1.0 \text{ \AA s}^{-1}$ . On top of the organic thin film, gold (80 nm) as drain and source electrodes was deposited through a shadow mask. For a typical device, the drain-source channel length ( $L$ ) and width ( $W$ ) are 50 or 100  $\mu\text{m}$  and ca. 1.5 mm, respectively. The characteristics of the OFET devices were measured at room temperature in air with a Keithley 4200 semiconductor parameter analyzer. Field-effect mobility ( $\mu_{\text{FET}}$ ) was calculated in the saturation regime ( $V_d = -60\text{ V}$ ) of the  $I_d$  using the following equation:  $I_d = (W C_i / 2L) \mu_{\text{FET}} (V_g - V_{\text{th}})^2$ , where  $C_i$  is the capacitance, and  $V_g$  and  $V_{\text{th}}$  are the gate and threshold voltages, respectively. Current on/off ratio ( $I_{\text{on}}/I_{\text{off}}$ ) was determined from the  $I_d$  at  $V_g = 0\text{ V}$  ( $I_{\text{off}}$ ) and  $V_g = -60\text{ V}$  ( $I_{\text{on}}$ ). The  $\mu_{\text{FET}}$  data reported in Table 2.3.2 are values from more than 10 different devices.

## 2.4 Bis(thieno[2,3-*d*])tetrathiafulvalenes ( $\alpha$ DT-TTFs)

**Introduction.** Pyrrolo[3,4-*d*]tetrathiafulvalenes (PyTTFs, **1** and **2**, Figure 2.4.1) described in section 2.2 and 2.3 were developed as solution processible p-type semiconductors. *N*-alkyl-PyTTF with long alkyl chains (**1g**) is highly soluble and form a crystalline thin-film that arranged with layer-by-layer structure.<sup>15</sup> *N*-hexanoyl-PyTTF (**2b**) that showed improved air-stability and mobilities in air, however, were low solubility.<sup>16</sup> The field-effect mobilities ( $\mu_{\text{FETs}}$ ) up to  $\sim 0.08$  cm<sup>2</sup>/Vs of PyTTFs-based OFETs are lower than that of DT-TTF. That is regarded as the prototypical compound of the heteroaromatic-fused TTF ( $\mu_{\text{FET}} = \sim 1.4$  cm<sup>2</sup>/Vs in single-crystal OFETs).<sup>14</sup> In fact, OFETs based on vacuum-deposited thin-films of DT-TTF showed performances with  $\mu_{\text{FETs}}$  up to 0.3 cm<sup>2</sup>/Vs (see Experimental Procedures, Figure 2.4.9). The superior performances of DT-TTF to those of the PyTTFs impelled me to investigate thieno[2,3-*d*]TTF ( $\alpha$ DT-TTF, **3a**), an isomer of DT-TTF, which could be platform for introducing alkyl chains at the  $\alpha$ -positions (C( $\alpha$ )) of the thiophene (Figure 2.4.2).

**3a** has been reported as a donor material as an unseparable mixture of the *cis/trans* isomers depending on the direction of the thiophene because of the easy rotation of the central double bond of the TTF core promoted by a protonation of the bond to give the isomer.<sup>97,118-120</sup> For this reason,  $\alpha$ DT-TTF should contains two *cis/trans* isomers rings in the solid state. Nevertheless, relative positions of the  $\alpha$ -carbon atoms in the two isomers should not be changed so much (Figure 2.4.3a). This is because the  $\alpha$ -carbons are on the apex of the five-membered ring, as was reported for 5-hexylthiophene-fused porphyrazines (C<sub>6</sub>H<sub>2</sub>Pc) by Miyazaki *et al.* (Figure 2.4.3).<sup>117</sup> Indeed C<sub>6</sub>H<sub>2</sub>Pc has well-ordered direction of the hexyl groups substituted at the  $\alpha$ -carbons, in spite of the completely disordered thiophene moieties (Figure 2.4.3b and c). In addition, strong intermolecular interaction can be expected regardless of the direction of the thiophene rings, because the HOMO coefficients of **3a** are mostly located on the TTF core (Figure 2.4.2, right).

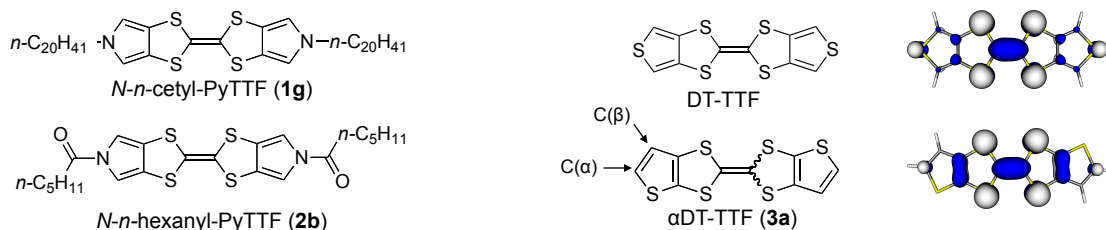


**Figure 2.4.1.** Structures of pyrrole-fused TTFs

**Figure 2.4.2.** Structures of thiophene-fused TTFs (left) and their HOMOs calculated by DFT (B3LYP/6-31G(d))<sup>111</sup> (right).

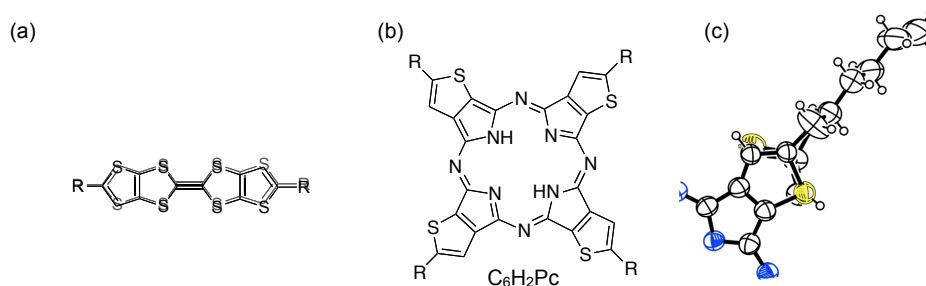
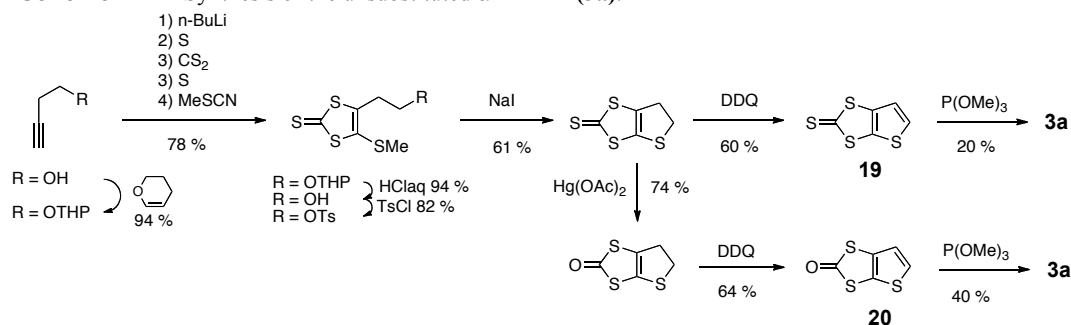


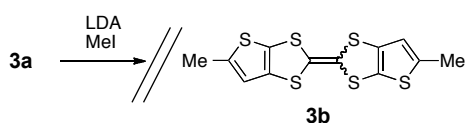
**Figure 2.4.3.** Explanation of disordered model. (a) Illustration of alkylated **3** with superimposed *cis* and *trans* isomers. (b) Structure of 5-hexylthiophene-fused porphyrazine and (c) the 5-hexylthiophene moiety in crystal, where two thiophene ring with different directions are superimposed.

## 2. Development of Heteroaromatic-fused TTFs

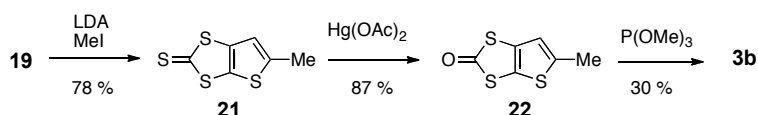
### Scheme 2.4.1. Synthesis of the unsubstituted $\alpha$ DT-TTF (**3a**).



### Scheme 2.4.2. Attempt to synthesize of methyl-substituted $\alpha$ DT-TTF (**3b**) from **3a**.



### Scheme 2.4.3. Synthesize of methyl-substituted $\alpha$ DT-TTF (**3b**)



### Scheme 2.4.4. Synthesize of octylthio-substituted $\alpha$ DT-TTF (**3c**)

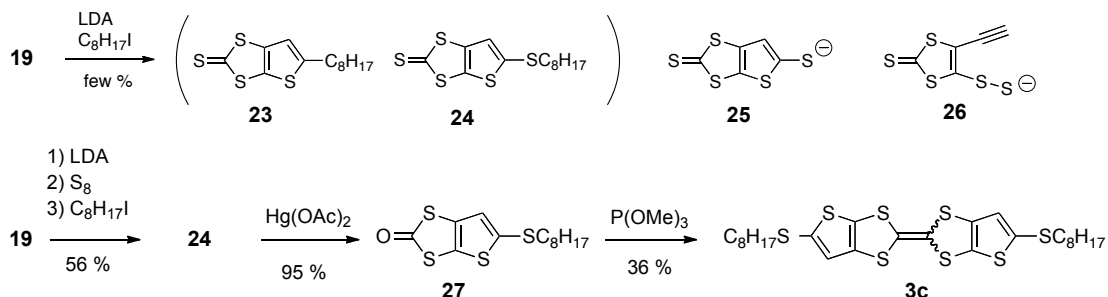


Table 2.4.1. Solubility of **3a-c**

	R	solubility <sup>a</sup> / g L <sup>-1</sup>	sublimation at ~10 <sup>-3</sup> Pa
<b>3a</b>	H	1	✓
<b>3b</b>	Me	<0.1	✓
<b>3c</b>	S-C <sub>8</sub> H <sub>17</sub>	25	-

<sup>a</sup> in toluene at r.t.

In this section, I describe syntheses, solid-state structures, and FET characteristics of  $\alpha$ DT-TTFs substituted with alkyl chains.

**Synthesis.** According to the reported procedure,<sup>97</sup> **3a** was synthesized (Scheme 2.4.1). I first tried to synthesize methyl-substituted  $\alpha$ DT-TTF from **3a** as a model alkylating reaction. Methylation of **3a**, however, did not proceed via a lithiation reaction followed by a reaction with methyl iodide (Scheme 2.4.2). Since chemical instability of the TTF skeleton was thought to cause the failure, I methylated intermediate **19** or **20**. Although the lithiation reaction of **20** did not give methylated compound, the reaction of **19** gave the desired methylated compound **21**

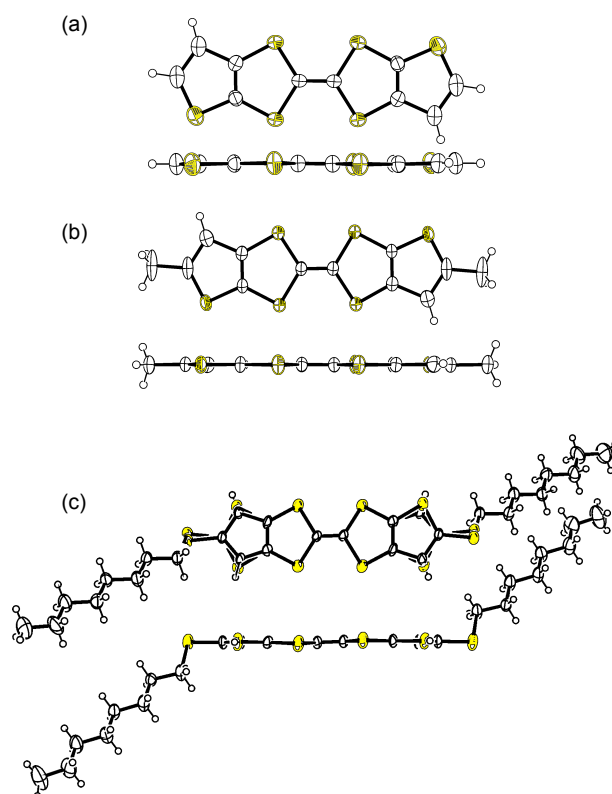


**Figure 2.4.4.** Molecular structures of (a) **3a**, (b) **3b**, and (c) **3c** illustrated with thermal ellipsoids at 50 % probability. The structures of different direction of thiophene rings are included in the *trans* form structure for **3a** and **3b**, and superimposed on the each thiophene site for **3c**.

(Scheme 2.4.3). Subsequent conversion to the ketone (**22**) and the following coupling reaction successfully gave methyl-substituted  $\alpha$ DT-TTF (**3b**). The similar reaction was then carried out using octyl iodide to synthesize the octyl derivative (Figure 2.4.4). The reaction, however, afforded a mixture of octyl-substituted compound (**23**) and the compound that seems to be *n*-octylthio-substituted compound (**24**) as a byproduct together with a large amount of unidentifiable polymeric product. This result suggests that the reaction involves unintended decomposition such as a ring-opening reaction and an attack to the substrates to give intermediate like **25** and **26**, which reacts with the octyl iodide reagent to give **24**. This result indicates that the lithiated **19** is not so reactive and tends to decompose via the ring-opening reaction to form elemental sulfur. At the same time, the thiolate intermediate **25** may be stable and reactive enough to afford **24**. Therefore, I added elemental sulfur into this reaction mixture, which resulted in a successful synthesis of **24** with an acceptable yield (56 %). The following reactions from **24** gave *n*-octylthio-substituted  $\alpha$ DT-TTF (**3c**). **3c** is highly soluble in contrast to virtually insoluble **3b** (Table 2.4.1).

**Disorder in Crystal Structures.** **3a-c** afforded single crystals that could be fully characterized by X-ray analysis (Figure 2.4.4). All molecular structures have disordered thiophene moieties, as seen in the other thiophene-fused crystals.<sup>14b,121</sup> The two thiophenes with different direction are drawn with two methods: the structures of **3a** and **3b** are depicted as the *trans* isomers where occupancies of the S and C( $\beta$ ) are mixed up with each other, and the structure of **3c** is shown with superimposing the two thiophene rings. Although the crystal analysis do not inform whether the *cis* isomers are contained or not, this *trans*-form-based disordered model gave de-

## 2. Development of Heteroaromatic-fused TTFs

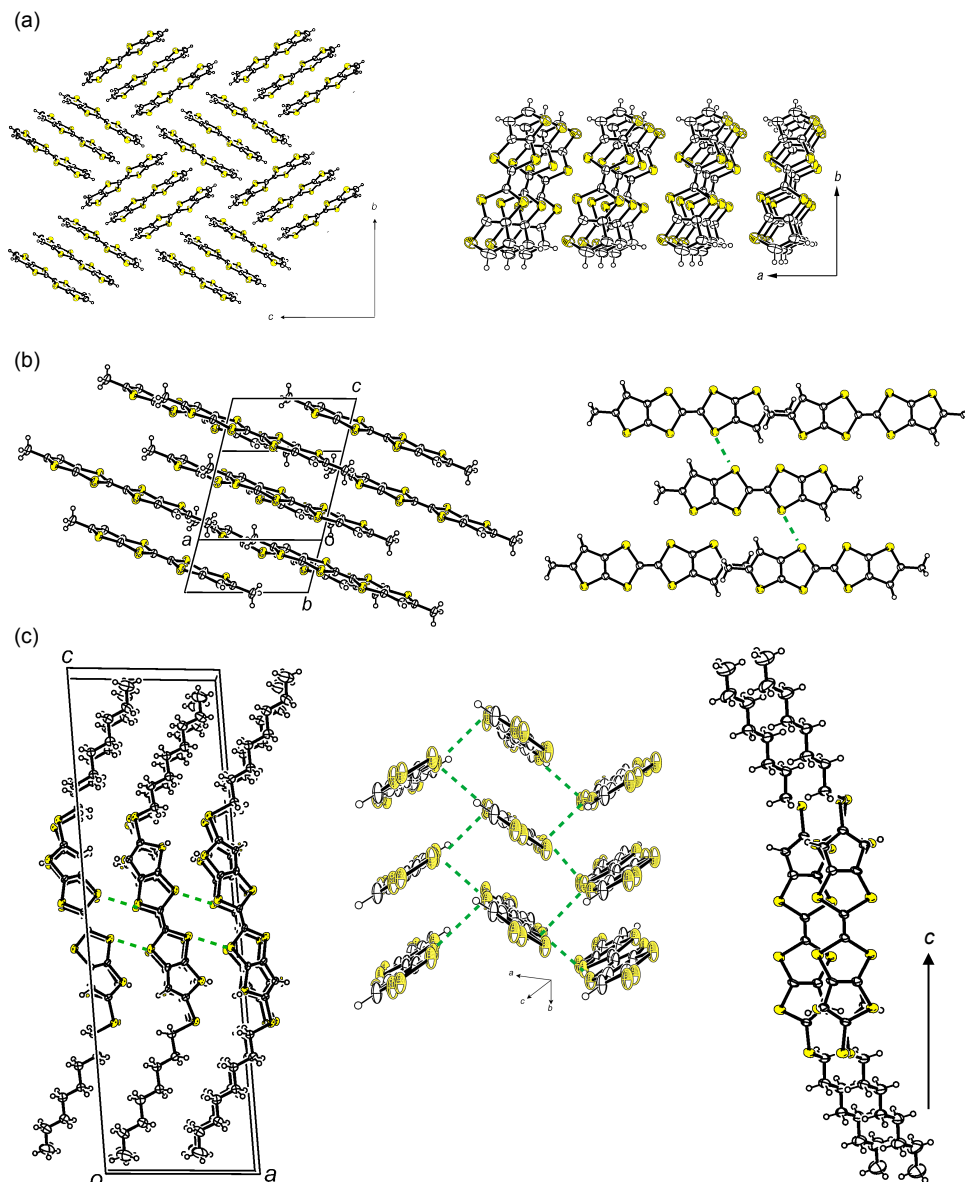


**Figure 2.4.5.** (a) Molecular arrangement of **3a** with *c*-axis projection (left) and depiction of one trimer-unit (right). (b) Arrangement of **3b** with view along the molecular short axis (left) and projection of one layer normal to the  $\pi$ -plane (right). (c) Arrangement of **3c** with *b*-axis projection (left), the molecular-long axis projection (middle, alkyl moieties are omitted), and normal to the  $\pi$ -plane (right). Green dash lines show S-S short contacts of 3.47 Å for **3b** and 3.46 Å for **3c**.

cent result for crystallographic analysis (see Table A1 in Appendix). Probabilities of the different directions of thiophene ring are 30%, 50%, and 33% for **3a**, **3b**, and **3c**, respectively. In spite of these disorders of the thiophene rings, **3a-c** are highly crystalline as evidenced by the ease of crystallization from solution. The *n*-octyl groups of **3c** is directed to anti-conformation with small disorders, which allows the well-ordered packing structure in the solid state (*vide infra*).

**Molecular Arrangement in the Bulk Single-Crystals.** In the single crystal of **3a**, molecular trimer units are packed in a herringbone like manner (Figure 2.4.5a). The molecules of **3b** are packed in a so-called “slipped herringbone-like packing” with completely no overlapped  $\pi$ -core, although short S-S contacts are observed (Figure 2.4.5b). As a result, neither arrangement of **3a** nor **3b** has an effective conducting layer. In contrast, the molecules of **3c** in the crystal are regu-

larly packed to form a layer-by-layer (alkyl -  $\pi$ -core - alkyl) structure (Figure 2.4.5c). The change in the molecular arrangements in the single crystals of **3a-c** are similar to those of PyTTFs (**1**), where the long alkyl groups play an important role in constructing a desirable structure for carrier transport as discussed in the previous section 2.2. The  $\pi$ -cores in the crystal of **3c** are interacted with each other in all neighboring molecules via side-by-side short S-S contacts (3.46 Å) (Figure 2.4.5, middle). Since **3c** takes the herringbone packing, the direct overlap of  $\pi$ -core is relatively small, the motif of which is similar to that of **2b** showing moderately high mobility (Figure 2.3.7).

**Thin-Film Fabrication.** A thin film of **3b** could not be fabricated by spin-coating method because of the low solubility (Table 2.4.1). Thin films of **3b** were fabricated by vacuum-deposition on Si/SiO<sub>2</sub> substrates to give lustrous films of **3b**. Although **3a** has relatively good solubility (~1 g/L in toluene at room temperature), fabrication of thin films with spin-coating method was not possible. Thin films of **3a** were fabricated by vacuum-deposition, which gave clouded films, which implies that, however, homogeneous thin films were not obtained. In contrast, highly soluble **3c** can be spin-coated at room temperature to give lustrous thin films of **3c** on the bare Si/SiO<sub>2</sub> substrate from 0.6 wt % toluene or benzene solution.

**Orientations and Morphologies of Thin Films.** The thin-films of **3a-c** showed sharp XRD peaks assignable to crystallographic (00 $l$ ) reflections, indicating formation of crystalline thin films (Figure 2.4.6). The peak positions of (001) and calculated  $d$ -spacings are listed in Table 2.4.2. The  $d$ -spacing of spin-coated **3c** film is 34 Å, which corresponds to the crystallographic  $c$ -

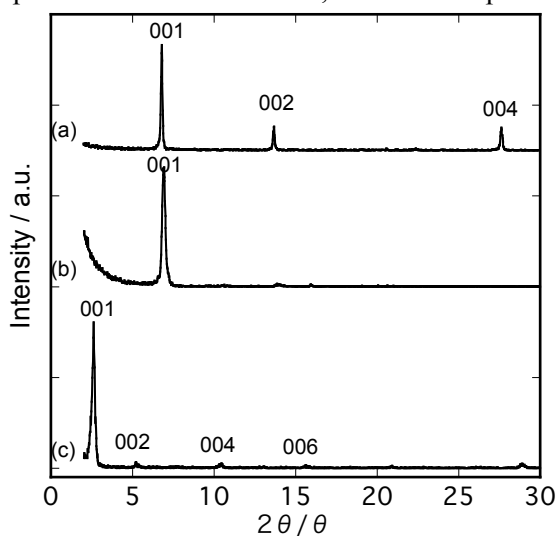


**Figure 2.4.6.** XRD pattern of (a) **3a**, (b) **3b**, and (c) **3c**.

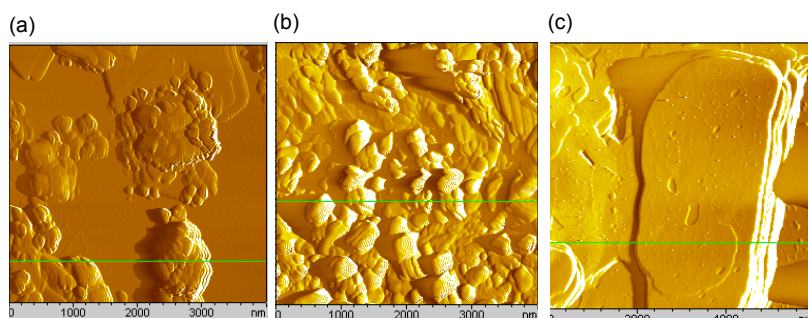


**Figure 2.4.7.** AFM images of (a) **3a**, (b) **3b**, and (c) **3c**. Difference of height on the green lines are as high as 400 nm for **3a**, 180 nm for **3b**, and 40 nm for **3c**.

**Table 2.4.2.** Interlayer distance of XRD pattern and FET characteristics of **3a-c** and DT-TTF.

R	process <sup>a</sup>	XRD patterns		OFET characteristics <sup>e</sup>		
		2 $\theta^d$ / $^\circ$	$d$ -spacing / $\text{\AA}$	$V_{th}$ / V	$\mu$ / $\text{cm}^2\text{V}^{-1}\text{s}^{-1}$	$I_{on}/I_{off}$
<b>3a</b> H	<i>vac</i>	6.8	13.0	-	-	-
<b>3b</b> Me	<i>vac</i>	6.9	12.8	-	-	-
<b>3c</b> S-C <sub>8</sub> H <sub>17</sub>	<i>spin</i> <sup>b</sup>	2.6	34	57	0.19	10 <sup>2</sup>
DT-TTF	<i>vac</i> <sup>c</sup>	6.7	13.1	3	0.3	10 <sup>5</sup>

<sup>a</sup> *vac* = vacuum-deposition, *spin* = spin-coat. <sup>b</sup> from 0.4 wt % toluene solution. <sup>c</sup> SiO<sub>2</sub> surface was treated with HMDS. <sup>d</sup> (001) peak in XRD pattern. <sup>e</sup> Typical value on top-contact devices with  $W = 50 \mu\text{m}$  and  $L = 1500 \mu\text{m}$ .

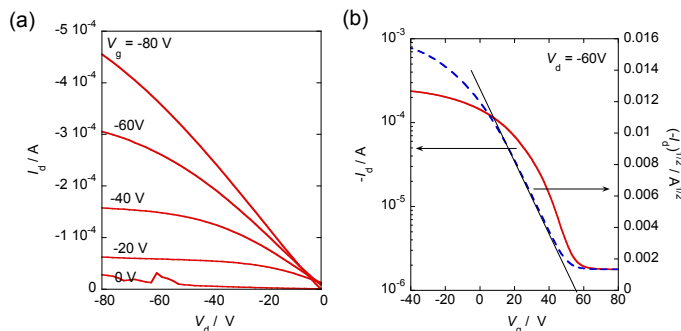


**Figure 2.4.8.** FET characteristics of **3c** on bare SiO<sub>2</sub> substrate: (a) output (b) transfer characteristics.

axis of the bulk crystal (34.06  $\text{\AA}$ ). This correspondence indicates formation of the layer-by-layer structure in the thin film as in the bulk crystal. On the other hand, the  $d$ -spacings of the thin films of **3a** and **3b** are different from any of the lengths of crystallographic axes, indicating that the structures of **3a** and **3b** in thin films are different from those of the bulk crystals. The  $d$ -spacings are almost equal to the molecular lengths, which implies that molecules stand upright to the substrate to form crystalline films with different arrangement from those in the bulk crystals.

Surface morphologies of the thin-film were studied by an atomic force microscopy (AFM) to examine quality of the films (Figure 2.4.7). The AFM image of thin film of **3a** deposited on the bare Si/SiO<sub>2</sub> substrate shows large crystalline grains with very large height differences (ca. 400 nm), indicating that non-uniform crystalline grains form. This is certainly due to too high crystallinity of **3a**. The AFM image of deposited thin film of **3b** shows crystalline grains with lower height differences (ca. 180 nm) than that of **3a**. This indicates that the uniformity of thin-film is improved, although the surface is fairly rough. In contrast, the AFM image of spin-coated **3b** film shows a relatively smooth surface with ca. 40 nm in step height. In general, uniform crystalline film is essential for a FET channel to achieve better performances.<sup>122</sup>

**FET Characteristics.** OFET devices were fabricated by deposition of gold source-drain electrodes on top of the thin films to give top-contact devices (see Experimental Procedures). The OFETs based on **3a** and **3b** showed no field-effect responses. Non-uniformity of the thin films should be responsible for the former, whereas the lack of  $\pi$ -overlap in the molecular orientation as discussed above is supposed for the latter. On the other hand, **3c**-based OFETs showed typical p-channel FET characteristics under ambient conditions (Table 2.4.2, Figure 2.4.8). The extracted  $\mu_{FETS}$  are up to 0.2  $\text{cm}^2/\text{Vs}$ , which are higher than those of PyTTF derivatives (**1g** and **2b**) and are almost comparable to those of devices based on DT-TTF fabricated by vacuum-deposition. The **3c**-based FETs are, however, suffered from heavily normally-on behavior ( $V_{th} \sim 50$  V), probably owing to its relatively low oxidation potential (*vide infra*).

**Table 2.4.3.** Oxidation potential<sup>a</sup> and the estimated HOMO levels.

	R	onset	$E_{1/2}^1$	$E_{1/2}^2$	$\Delta E$	$E_{\text{HOMO}}^b / \text{eV}$
<b>3a</b>	H	-0.05	0.03	0.38	0.35	-4.75
<b>3b</b>	Me	-0.12	-0.04	0.32	0.36	-4.68
<b>3c</b>	S-C <sub>8</sub> H <sub>17</sub>	-0.04	0.03	0.34	0.31	-4.77
	DT-TTF	0.18	0.30	0.63	0.33	-4.98

<sup>a</sup> Vs Fc/Fc<sup>+</sup>. <sup>b</sup>  $E_{1/2}(\text{Fc}/\text{Fc}^+) = -4.8 \text{ eV}$  under vacuum level as a criteria.

**Oxidation Potentials.** In order to estimate molecular electronic structures, oxidation potentials of the thiophene-fused TTFs were measured with cyclic voltammetry (Table 2.4.3). First oxidation potential of **3a** ( $E_{1/2}^1 = +0.03 \text{ V}$  vs Fc/Fc<sup>+</sup>) is lower by 0.27 V than that of DT-TTF ( $E_{1/2}^1 = 0.30 \text{ V}$ ). This large difference indicates that the electronic structure of **3a** markedly differs from that of DT-TTF. The lower oxidation potential of **3a** may be related to the resonance structure where TTF moiety can obtain  $6\pi$ -aromaticity in the cationic state, in contrast to that of DT-TTF that may become  $10\pi$ -aromaticity or break aromaticity of thiophene moiety in the cationic state.

The methyl groups increase the oxidation potential of **3a** slightly by 0.07 V ( $E_{1/2}^1$  of **3b** = -0.04 V). On the other hand, the oxidation potential of **3c** ( $E_{1/2}^1 = 0.03 \text{ V}$ ) is almost equal to that of the **3a**, indicating electronically neutral character of alkylthio group in this case, as a consequence of compensation of the inductive effect by the resonance effect. The energy level of the HOMO ( $E_{\text{HOMO}}$ ) of **3c** estimated from the oxidation onsets are -4.77 eV. This value is, unfortunately, higher than that of DT-TTF ( $E_{\text{HOMO}} = -4.98 \text{ eV}$ ) and *N*-acyl-substituted PyTTF (**2b**,  $E_{\text{HOMO}} = -4.95 \text{ eV}$ ) which showed good air-stability in their devices. This higher  $E_{\text{HOMO}}$  (low oxidation potential) is presumably responsible for the normally-on characteristics of the OFET devices. The low oxidation potential makes the molecule susceptible to the air-oxidation similar to that observed for the *N*-alkyl-PyTTF (**1g**).

**Summary.** The methyl (**3b**)- and *n*-octylthio (**3c**)-substituted  $\alpha$ DT-TTF were successfully synthesized. Single-crystal X-ray analysis revealed small positional disorders in the  $\alpha$ -positions of the thiophene rings and the *n*-octylthio groups of **3c**, which promotes well-ordered layer-by-layer molecular arrangement in the solid state. This can be understood by considering hydrophobic interaction between the alkyl chains. In the structure, the TTF core of **3c** are interacted with all neighboring ones via the short S-S contacts, which is similar to that of DT-TTF. The solution-processed OFETs based on **3c** showed high  $\mu_{\text{FETS}}$  up to  $0.2 \text{ cm}^2/\text{Vs}$ , which is comparable to those of vacuum-processed DT-TTF-based OFETs. The heavily normally-on behavior of **3c**-based devices can be attributed to its lower oxidation potential caused by the different contribution of the fused thiophene ring to the electronic structure of the whole molecules. Further improvement of molecular design strategy is required to keep the HOMO energy level lower.

## Experimental Procedures

### Synthesis:

**General:** All chemicals and solvents are of reagent grade unless otherwise indicated. DMF was distilled from CaH<sub>2</sub> under reduced pressure. THF was distilled from Na before use. Trimethylphosphite was treated with sodium for 24 h, then distilled in an inert atmosphere and stored with activated molecular sieves 4 Å. Melting points were not collected. Nuclear magnetic resonance spectra were obtained in deuterated chloroform with a JEOL EX 270 spectrometer operating at 270 MHz for <sup>1</sup>H with TMS as internal reference; chemical shifts ( $\delta$ ) are reported in parts per million. EI-MS spectra were obtained on a Shimadzu QP-5050A spectrometer using an electron impact ionization procedure (70 eV). The molecular ion peaks of the sulfur-containing compounds showed a typical isotopic pattern, and all the mass peaks are reported based on <sup>32</sup>S.

**5-Methylthieno[2,3-*d*]-1,3-dithiole-2-thione (21).** Under N<sub>2</sub> atmosphere, thieno[2,3-*d*]-1,3-dithiole-2-thione (**19**) (952 mg, 5 mmol) was dissolved in THF (35 mL). The mixture was then cooled down to -80 °C before addition of 0.5 M lithium diisopropyl amide (LDA) in THF (12 mL, 6 mmol). Iodomethane (1.87 mL, 30 mmol) was added and stirred for 30 min, the mixture was kept stirring for 2 h at 60 °C. After quench the reaction by addition of water, the resulting mixture was extracted by CH<sub>2</sub>Cl<sub>2</sub> (50 mL × 4). The organic layer was washed with sat. NaCl<sub>aq</sub> (75 mL) and dried with anhydrous MgSO<sub>4</sub>. Yellow solids, obtained by evaporation of the solvent, were purified by column-chromatography (SiO<sub>2</sub>, CH<sub>2</sub>Cl<sub>2</sub>/hexane=1:1, *R<sub>f</sub>* = 0.79) to give yellow crystals of **21** (797 mg, 78 %). <sup>1</sup>H-NMR (270 MHz, CDCl<sub>3</sub>, TMS) δ 6.76 (q, *J* = 1.16 Hz, 1 H), 2.58 (d, *J* = 1.15 Hz, 3 H).

**5-Methylthieno[2,3-*d*]-1,3-dithiole-2-one (22).** Mercury (II) acetate (3.73 g, 11.7 mmol) was added to a solution of compound **21** (797 mg, 3.9 mmol) in CHCl<sub>3</sub> (150 mL), and the mixture was stirred for 6 h at rt. The resulting mixture was filtered through celite, and the filtrate was evaporated. The resulting yellow solids were purified by column-chromatography (SiO<sub>2</sub>, CH<sub>2</sub>Cl<sub>2</sub>/Hexane = 1:1, *R<sub>f</sub>* = 0.79) to give **22** as white crystals (636 mg). <sup>1</sup>H-NMR (270 MHz, CDCl<sub>3</sub>, TMS) δ 6.79 (q, *J* = 1.20 Hz, 1 H), 2.56 (d, *J* = 1.23 Hz, 3 H).

**(Z)/(E)-Bis(5,5'-dimethylthieno)[3,4-*d*]tetrathiafulvalene (3b).** Under N<sub>2</sub> atmosphere, **22** (636 mg, 3.38 mmol) was added into trimethylphosphite (5 mL). The coupling reaction was completed by refluxing mixture at 140 °C for 2.5 h. After cooling down the mixture, the trimethylphosphite was removed by evaporation in vacuum. The resulting red solids were purified by column-chromatography (SiO<sub>2</sub>, CS<sub>2</sub>, *R<sub>f</sub>* = 0.85) followed by recrystallization from toluene/hexane. **3b** was obtained as red crystals (175 mg, 30 %). <sup>1</sup>H-NMR (270 MHz, CDCl<sub>3</sub>, TMS) δ 1.26 (s), 6.55 (bs). DI-MS (70 eV, EI) *m/z* = 344 (M<sup>+</sup>).

**5-octylthiothieno[2,3-*d*]-1,3-dithiole-2-thione (24).** Under N<sub>2</sub> atmosphere, 0.5 M LDA in THF (5.5 mL, 2.75 mmol) was added to a solution of **19** (480 mg, 2.5 mmol) in THF (23 mL) at 0 °C. Subsequently elemental sulfur (88 mg, 2.75 mmol) was added to the mixture and stirred for 10 min at 0 °C, which is followed by addition of iodoctane (2.7 mL, 15 mmol). The reaction mixture was warmed up ~60 °C and then kept stirring for 2 h. After that, the reaction was quenched by addition of water. The mixture was extracted with CH<sub>2</sub>Cl<sub>2</sub> (50 mL × 4). The resulting organic phase was washed with NaCl<sub>aq</sub> (75 mL) and dried with anhydrous MgSO<sub>4</sub>. Evaporation of the solvent gave red solids, which was purified by column-chromatography (SiO<sub>2</sub>, CH<sub>2</sub>Cl<sub>2</sub>/hexane = 1:4, *R<sub>f</sub>* = 0.65). **3c** was obtained as red crystals (477 mg, 57 %). <sup>1</sup>H-NMR (270 MHz, CDCl<sub>3</sub>, TMS) δ 7.07 (s, 1H), 2.84 (t, 2H) 1.54~1.65 (m, 7H) 0.88 (t, 3H)

**5-Octylthiothieno[2,3-*d*]-1,3-dithiole-2-one (27).** Mercury (II) Acetate (1.36 g, 4.3 mmol) was added to a solution of **24** (477 mg, 1.43 mmol) in CHCl<sub>3</sub> (160 mL), and the solution was stirred for 2 h at rt. The resulting mixture was filtered through celite, and subsequent evaporation gave yellowy solids. The crude product was purified by column-chromatography (SiO<sub>2</sub>, CH<sub>2</sub>Cl<sub>2</sub> = 1:1, *R<sub>f</sub>* = 0.65) to give compound **27** as brown oil (454 mg, 95 %). <sup>1</sup>H-NMR (270 MHz, CDCl<sub>3</sub>, TMS) δ 7.07 (s, 1H), 2.84 (t, 2H) 1.54 - 1.65 (m, 7H) 0.88 (t, 3H).

**(Z)/(E)-Bis(5,5'-dioctylthiothieno[2,3-*d*]tetrathiafulvalene (3c).** Under N<sub>2</sub> atmosphere, **27** (430 mg, 1.35 mmol) was added to trimethylphosphite (3 mL). After reflux of the mixture at 140 °C for 2.5 h, the solvent was evaporated to give red solids. The solids were purified by column-chromatography (SiO<sub>2</sub>, CS<sub>2</sub>, *R<sub>f</sub>* = 0.85) followed by recrystallization from cool toluene/hexane. **3c** was obtained as orange crystals (146 mg, 36 %) For device fabrication, the product was recrystallized twice. MS (70 eV, EI) *m/z* = 604 (M<sup>+</sup>). <sup>1</sup>H-NMR (270 MHz, CDCl<sub>3</sub>, TMS) δ 7.07 (s, 1H), 2.84 (t, 2H) 1.54 - 1.65 (m, 7H) 0.88 (t, 3H).

**X-ray diffraction (XRD) measurements of thin-films and single-crystals.** XRD patterns of spin-coated thin films deposited on Si/SiO<sub>2</sub> substrates were obtained with a Rigaku RiNT-2200 diffractometer with a Cu K $\alpha$  source ( $\lambda$  = 1.541 Å) in air. The *d*-spacings were calculated by the Bragg equation:  $\lambda = 2d\sin\theta$ . The single crystal XRDs were measured on a Rigaku Rapid-S Imaging Plate with graphite monochromated ( $2\theta_{\max}$  = 55°) Mo K $\alpha$  source ( $\lambda$  = 0.71069 Å) for **3a** and **3b**. The X-ray analysis of crystal of **3c** was made on Rigaku DSC imaging plate system by using Si-monochromated synchrotron ( $\lambda$  = 1.00000 Å) at beam line BL8B of Photon Factory (PF) in High Energy Accelerator Research Organization (KEK). Detailed crystallographic data are listed in Table A1 (p62). The structure was solved by direct methods (SIR92).<sup>106</sup> Non-hydrogen atoms were refined anisotropically, and hydrogen atoms were included in the calculations but not refined.<sup>107</sup> Calculations were performed using the crystallographic software package TeXsan<sup>108</sup> and Yadocari software package for **3a-b** and **3c**, respectively.

**Atomic Force Microscopy (AFM).** The AFM images were measured on a Molecular Imaging PicoPlus microscope in air.

**Table 2.4.4.** FET characteristics of **3c**.

solvent	wt %	rpm	V <sub>th</sub> / V	$\mu$ / cm <sup>2</sup> V <sup>-1</sup> s <sup>-1</sup>	I <sub>on</sub> /I <sub>off</sub>
toluene	0.6	2000	57	0.19	10 <sup>2</sup>
	2.0	4000	55	0.15	10 <sup>1</sup>
benzene	0.6	2000	66	0.27	10 <sup>1</sup>
	2.0	4000	77	0.14	10 <sup>1</sup>

**Device Fabrications and Evaluations.** OFETs were fabricated in a top-contact configuration on a heavily doped  $n^+$ -Si (100) wafer with 200-nm-thick thermally grown  $\text{SiO}_2$  ( $C_i = 17.3 \text{ nF cm}^{-2}$ ). The 50 nm in thickness of thin films of **3a**, **3b**, and DT-TTF were fabricated on the substrates by vacuum-deposition with room substrate temperature and deposition rate of  $\sim 1.0 \text{ \AA/s}$ . The thin films of **3c** was fabricated by spin-coating from the 0.6 and 2.0 wt % of benzene or toluene solution with the spin-coat rate of 2000 and 4000 rpm, respectively (Table 2.4.4). The OFET devices were fabricated by deposition of gold source-drain electrodes on the thin films. The channel width ( $W$ ) and length ( $L$ ) are  $50 \mu\text{m}$  and  $1500 \mu\text{m}$ , respectively. The characteristics of the OFET devices were measured in air with a Keithley 4200 semiconductor parameter analyzer. Field-effect mobility ( $\mu_{\text{FET}}$ ) was calculated in the saturation regime ( $V_d = -60 \text{ V}$ ) of the  $I_d$  using the following equation:  $I_d = (WC_i/2L) \mu_{\text{FET}} (V_g - V_{\text{th}})^2$ , where  $C_i$  is the capacitance, and  $V_g$  and  $V_{\text{th}}$  are the gate and threshold voltages, respectively. The FET characteristics of **3c**-based devices fabricated with different spin-coat conditions are described in Table 2.4.4. The characteristics are averaged values of more than three devices. The FET characteristics of DT-TTF was shown Figure 2.4.9. The extracted  $\mu_{\text{FET}}$ s are up to  $0.3 \text{ cm}^2/\text{Vs}$  on the HMDS treated substrates.

**Molecular orbital (MO) calculation.** Geometry optimization and normal mode MO calculation of **3a-c** were carried out by the DFT method at the B3LYP/6-31G(d) level using the Gaussian03 program.<sup>111</sup> The HOMO of **3c** (alkyl moiety is converted to methyl group) is depicted in Figure 2.4.10.

**Cyclic voltammetry (CV).** CVs were recorded on a Hokuto Denko HA-301 potentiostat and a Hokuto Denko HB-104 function generator in  $10^{-3} \text{ M}$  benzonitrile solution containing  $0.1 \text{ M Bu}_4\text{N}^+\text{PF}_6^-$  as a supporting electrolyte with scan rate is  $100 \text{ mV/s}$ , by using Pt work/counter electrodes and Ag/AgCl reference electrode. All the potentials were calibrated with the standard ferrocene/ferrocenium ( $\text{Fc}/\text{Fc}^+$ ) redox couple ( $E^{1/2} = +0.43 \text{ V}$  measured under identical conditions). Cyclic voltammogram of **3a-c** and DT-TTF are shown in Figure 2.4.11.

**UV-Vis absorption spectrum.** UV-Vis spectra of **3a-c** in dichloromethane solution are recorded on Shimadzu UV-3100 spectrophotometer. The spectra are shown in Figure 2.4.12.

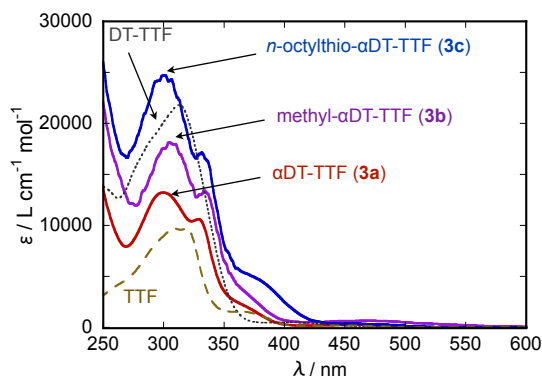


Figure 2.4.12. UV-Vis spectra of **3a-c**, DT-TTF, and TTF.

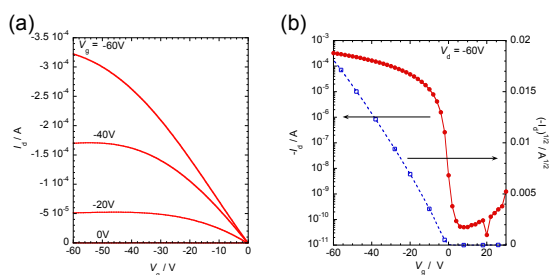


Figure 2.4.9. FET characteristics of thin-film-based DT-TTF devices on the HMDS treated  $\text{SiO}_2$  substrate: (a) output (b) transfer characteristics.

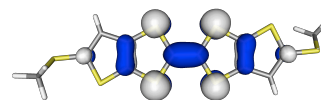


Figure 2.4.10. HOMO of methylthio-substituted  $\alpha$ DT-TTF estimated by single point calculation based on the crystal structure of **3c** with DFT (B3LYP/6-31G\*) method.

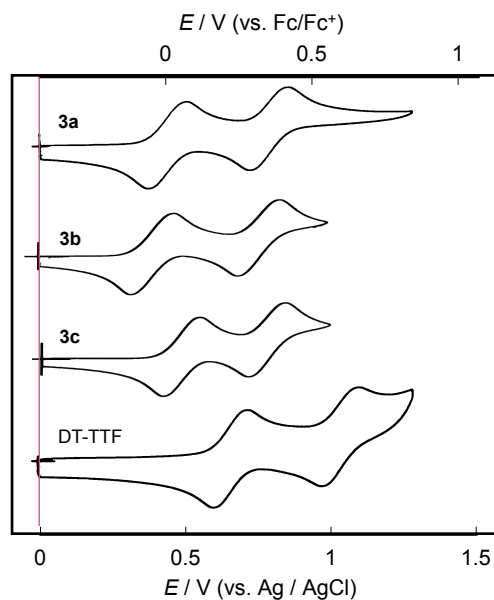


Figure 2.4.11. Cyclic voltammograms of **3a-c** and DT-TTF.

## 2.5 Correlation between Electronic Structure in Solid State and Field-Effect Mobility

### Introduction.

The synthesis, properties, and structures of the heteroaromatic-fused TTFs substituted with long alkyl groups were described in section 2.2 - 2.4. The correlation between the FET characteristics and the structures of the TTF derivatives clearly demonstrated that such molecular design as the TTF  $\pi$ -cores with long alkyl group successfully give solution processible organic semiconductors.

The two-dimensional (2-D) electronic structures via  $\pi$ - $\pi$  and/or S-S interactions between the TTF-cores may be realized in the solid states for the present TTF derivatives, which results in relatively good FET characteristics, e.g., *N-n*-cetyl-PyTTFs (**1f**), *N-n*-hexanoyl-PyTTF (**2b**) and *n*-octylthio- $\alpha$ DT-TTF (**3c**) (Figure 2.5.1). Nevertheless, the  $\mu_{\text{FETs}}$  of the derivatives are lower than those of recently developed superior semiconductors such as pentacene,<sup>47,123</sup> dinaphtho[2,3-*b*:2',3'-*f*]thieno[3,2-*b*]thiophene (DNNT),<sup>17</sup> 2,7-didodecyl[1]dibenzothieno[3,2-*b*][1]benzothiophene (C<sub>12</sub>-BTBT),<sup>124,125</sup> and hexamethylenetetrafulvalene (HM-TTF)<sup>88</sup> (Figure 2.5.2). The FET characteristics of these materials are summarized in Table 2.5.1.

Among these superior  $\mu_{\text{FET}}$  semiconductors, the solution-processible C<sub>12</sub>-BTBT are developed along with the same molecular design strategy as the present heteroaromatic-fused TTFs. There-

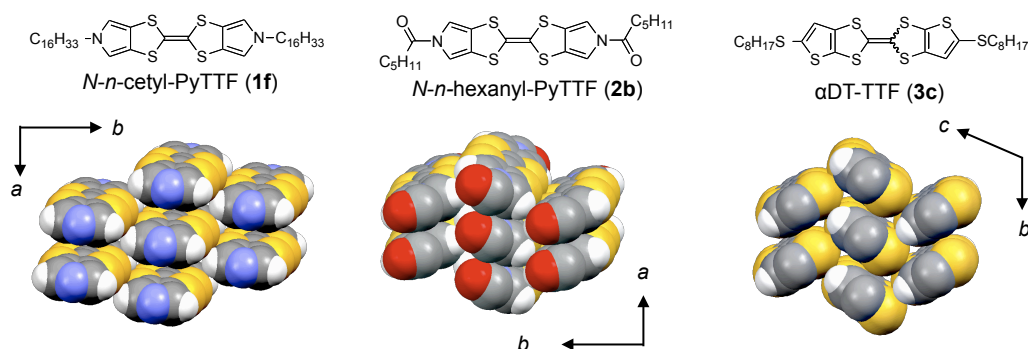


**Figure 2.5.1.** Structures of the **1f**, **2b**, and **3c** (top) with their molecular arrangement viewed along the molecular-long axis with space-filling model (bottom, alkyl(thio) moieties are omitted for clarity).

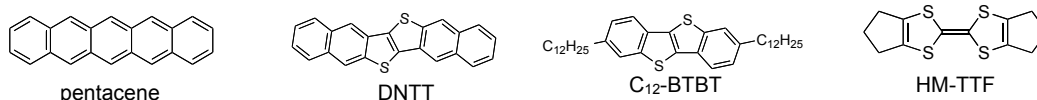


**Figure 2.5.2.** Structure of high performance organic semiconductors recently reported.

**Table 2.5.1.** Summary of FET characteristics of the heteroaromatic-fused TTFs and high performance materials reported recently.

	process <sup>a</sup>	TFT characteristics <sup>b</sup>		
		$V_{\text{th}} / \text{V}$	$\mu / \text{cm}^2\text{V}^{-1}\text{s}^{-1}$	$I_{\text{on}}/I_{\text{off}}$
<b>1d</b> <i>N-n</i> -octyl-PyTTF	<i>spin</i>	-	<i>no field effect</i>	-
<b>1f</b> <i>N-n</i> -cetyl-PyTTF	<i>spin</i>	10	0.008	10 <sup>4</sup>
<b>2b</b> <i>N-n</i> -hexanoyl-PyTTF	<i>vac</i>	-4	0.08	10 <sup>5</sup>
<b>3b</b> methyl- $\alpha$ DT-TTF	<i>vac</i>	-	<i>no field effect</i>	-
<b>3c</b> <i>n</i> -octylthio- $\alpha$ DT-TTF	<i>spin</i>	50	0.2	10 <sup>2</sup>
DT-TTF	<i>vac</i>	3	0.3	10 <sup>5</sup>
pentacene	<i>vac</i>	-11	0.30	10 <sup>8</sup>
DNNT	<i>vac</i>	-10	2.9	10 <sup>7</sup>
C <sub>12</sub> -BTBT	<i>spin</i>	-20	1.7	10 <sup>8</sup>
HM-TTF <sup>c</sup>	<i>vac</i>	27	3.6	10 <sup>3</sup>

<sup>a</sup> *vac* = vacuum-deposition, *spin* = spin-coat. <sup>b</sup> All top-contact configuration with Au electrodes ( $W = 1500 \mu\text{m}$ ,  $L = 50 \mu\text{m}$ ) measured in air. <sup>c</sup> Reported value.<sup>88</sup>

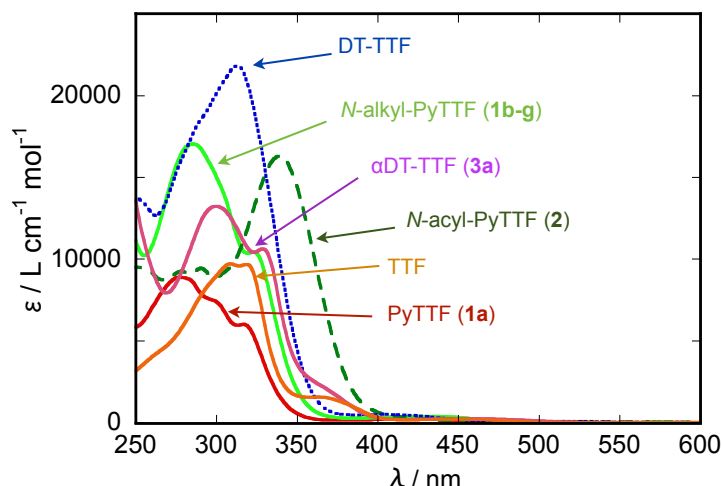


**Figure 2.5.3.** UV-Vis spectra of the TTF derivatives in  $\text{CH}_2\text{Cl}_2$  solution. The spectra of **3b** and **3c** is shown in Figure 2.4.12, which is similar to that of **3a**.

**Table 2.5.2.** HOMO and LUMO levels estimated experimentally from CV and UV-Vis spectra.

		oxidation potential <sup>a</sup> / V			$E_{\text{HOMO}}^b$ / eV	abs / nm		$\Delta E_g^c$ / eV	$E_{\text{LUMO}}^d$ / eV
		onset	$E^1_{1/2}$	$E^2_{1/2}$		$\lambda_{\text{max}}$	$\lambda_{\text{edge}}$		
<b>1f</b>	<i>N-n</i> -cetyl-PyTTF <sup>e</sup>	-0.18	-0.11	0.31	-4.62	284	481	2.58	-2.04
<b>2b</b>	<i>N-n</i> -hexanoyl-PyTTF	0.15	0.22	0.59	-4.95	337	449	2.76	-2.19
<b>3b</b>	methyl- $\alpha$ DT-TTF	-0.12	-0.04	0.32	-4.68	306	550	2.25	-2.43
<b>3c</b>	<i>n</i> -octylthio- $\alpha$ DT-TTF	-0.04	0.03	0.34	-4.76	300	520	2.38	-2.39
	DT-TTF	0.18	0.30	0.63	-4.98	312	521	2.38	-2.60
	TTF	-0.18	-0.11	0.34	-4.62	311	500	2.48	-2.14
	pentacene	-0.17	-	-	-4.97	-	600	2.06	-2.91
	DNTT <sup>f</sup>	0.64	0.75	-	-5.44	401	420	2.95	-2.49
	C <sub>12</sub> -BTBT <sup>g</sup>	0.7	0.89	NA	-5.5	NA	NA	3.5	-2.0
	HM-TTF <sup>h</sup>	NA	-0.19	0.29	-4.5	NA	NA	NA	NA

<sup>a</sup> vs. Fc/Fc<sup>+</sup>. <sup>b</sup>  $E_{\text{HOMO}} = -4.8 - \text{onset voltage (eV)}$ . <sup>c</sup>  $E_g = 1240 / \lambda_{\text{edge}}$ . <sup>d</sup>  $E_{\text{LUMO}} = E_{\text{HOMO}} + E_g$ . <sup>e</sup> The same as that of **1c**. <sup>f-h</sup> referred from the reports<sup>17,124,88</sup>.

fore, it should be very interesting to see the difference in the packing structure in qualitatively. In order to clarify the difference in the electronic structures of  $\pi$ -cores at the molecular level and then correlate the crystal structures and transport properties in OFETs, molecular orbitals (MOs), reorganization energy ( $\lambda$ ), and transfer integrals ( $t$ ) in bulk single crystal structure are calculated for the heteroaromatic-fused TTFs together with the high performance OFET materials.<sup>126-128</sup> The theoretically determined electronic structures are correlated to experimentally determined electrochemical and optical properties to confirm the suitability of the calculations. Comparisons of the electronic structures will give insight into understanding the performance of the TTF-based semiconductors and will give a new design strategy for better materials.

**Oxidation Potential and UV-Vis Spectra.** Figure 2.5.3, Table 2.5.2 summarized the electronic properties of the heteroaromatic-fused TTFs experimentally by measuring their cyclic voltammeteries and UV-Vis absorption spectra. As already described in the previous sections, oxidation potential of the **1f** and **3b** are low, which makes their devices susceptible to air-oxidation. **2b**-based OFETs showed improved air-stability because of the higher oxidation potential. The HOMO energy level ( $E_{\text{HOMO}}$ ) of **2b** estimated from first oxidation onset is ca. -4.95 eV.<sup>112</sup> Nevertheless, the  $E_{\text{HOMO}}$  of **2b** is still higher by more than 0.4 eV than those of DNTT and

C<sub>12</sub>-DNNT. DNNT-based devices do not degrade at least six or more months under ambient conditions. This fact indicates that the introduction of electron-withdrawing carbonyl group to the TTF framework is insufficient for lowering the  $E_{\text{HOMO}}$  to fully air-stable level. Further development of methods for introducing strongly electron-deficient moieties into the TTF  $\pi$ -core should be required<sup>83,75</sup>

UV-Vis spectra of the TTF derivatives are shown in Figure 2.5.3. Most of the TTF derivatives have weak absorptions on their shoulders, which is ascribed to forbidden HOMO-LUMO excitations as seen for the parent TTF.<sup>129</sup> Optical HOMO-LUMO energy gaps ( $\Delta E_g$ ) were estimated from the edge of the weak absorption, and then the energy level of the LUMOs ( $E_{\text{LUMOS}}$ ) are estimated by using  $E_{\text{HOMOS}}$  and  $\Delta E_g$ s.<sup>113</sup> Among the present TTF derivatives, **2b** shows an extraordinary spectrum, which has no shoulder. Because the same spectra were obtained in the different solvents or concentrations for **2b**, the HOMO-LUMO excitation of **2b** is thought to be allowed, and has become the main peak ( $\lambda_{\text{max}} = 337$  nm). Thus the  $E_{\text{LUMO}}$  of **2b** was estimated from the absorption edge and the  $E_{\text{HOMO}}$  to be -2.19 eV, which is lower than that of **1f** reasonably. Since no further information for the electronic structure related to the FET characteristics was obtained from the experimental analyses, theoretical calculations were carried out as follows.

**Molecular Electronic Structures: MO Calculation.** Molecular orbital (MO) calculation were carried out to examine shapes and energy levels of frontier orbitals, which related to the electron transport properties. It should be noted that molecular structure experimentally determined by X-ray analysis were used for initial molecular coordinates except for **2b**. This approach is very important for TTF derivatives, because the geometrical optimization of TTF molecules by DFT calculation often results in bended molecular shapes, which is far away from real molecular in the solid states.<sup>130</sup>

The calculated  $E_{\text{HOMOS}}$  are in good agreements with the experimental results, indicating the calculations give the decent results (Table 2.5.3). The tendency of the calculated  $E_{\text{LUMOS}}$  is also consistent with

**Table 2.5.3.** Calculated frontier orbitals<sup>a</sup>.

		$E_{\text{HOMO}} / \text{eV}$	$E_{\text{LUMO}} / \text{eV}$
<b>1f</b>	<i>N-n</i> -cetyl-PyTTF	-4.22	-0.56
<b>2b</b>	<i>N-n</i> -hexanoyl-PyTTF	-4.92	-1.24
<b>3a</b>	$\alpha$ DT-TTF	-4.66	-2.32
<b>3b</b>	methyl- $\alpha$ DT-TTF	-4.51	-1.01
<b>3c</b>	<i>n</i> -octylthio- $\alpha$ DT-TTF <sup>b</sup>	-4.63	-1.27
	DT-TTF	-4.94	-1.19
	TTF	-4.52	-0.95
	pentacene	-4.60	-0.94
	DNNT	-5.18	-1.81
	C <sub>12</sub> -BTBT	-5.40	-1.14
	HM-TTF	-4.32	-0.72

<sup>a</sup> Based on DFT with B3LYP/6-31G(d) basis set. The alkyl groups are inverted to methyl groups for ease of calculations. All molecules were kept in planar geometry while calculation.  
<sup>b</sup> single-point calculation.

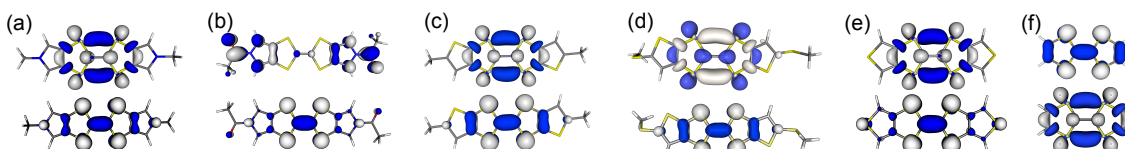


**Figure 2.5.4.** Coefficients of LUMO (top) and HOMO (bottom) of (a) **1f**, (b) **2b**, (c) **3b**, (d) **3c**, (e) DT-TTF, and (f) TTF.

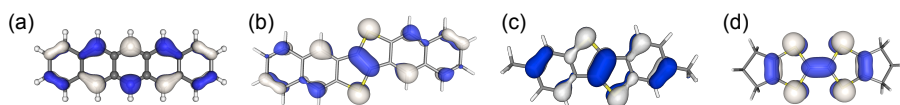


**Figure 2.5.5.** Coefficients of HOMO of (a) pentacene (b) DNNT, (c) BTBT, and (d) HM-TTF.

experimental results, although the absolute values are different from experimental results because the DFT calculation does not consider a configured interaction in an excited state.<sup>131</sup>

The MO calculation together with time-dependent DFT calculation supports the allowed HOMO-LUMO excitation of **2b** (HOMO → LUMO: oscillator strength = 0.51 at 377 nm)<sup>131</sup>, which consistent with the distinct absorption spectra for **2b**, probably reflecting the LUMO shape of **2b** which fairly differed from those of the other TTF derivatives (Figure 2.5.4).

On the other hand, the calculated HOMOs of the TTF derivatives are similar to each other, where the coefficients are largely on the sulfur atoms. All the derivatives thus could strongly interact intermolecularly via S-S contacts in solid states. Note that the large HOMO coefficients on the sulfur atoms and/or on the periphery of the molecules are also found in the high  $\mu_{\text{FET}}$  materials (Figure 2.5.5).<sup>132</sup>

The overview of molecular electronic structures indicates capability of the heteroaromatic-fused TTF to realize high  $\mu_{\text{FET}}$  comparable to those of the state-of-the-art materials, whereas the air-stability should be no good.

**Parameters in Charge-Transport in OFETs.** Understanding the theory of charge-transport in OFETs is necessary for further evaluation of the electronic properties in the solid state.<sup>133</sup> It is rationally believed that carrier transport in the majority of organic semiconductors can be classified into the hopping model.<sup>134</sup> The hopping  $\mu_{\text{FET}}$  can be expressed by<sup>135</sup>

$$\mu_{\text{FET}} = \frac{qd^2}{k_{\text{B}}T} k_{\text{ET}} \dots (1)$$

$$k_{\text{ET}} = t^2 \sqrt{\frac{\pi}{\hbar k_{\text{B}} T \lambda}} \exp\left(-\frac{(\Delta E - \lambda)^2}{4\lambda k_{\text{B}} T}\right) \dots (2)$$

where  $q$  is the number of charge,  $d$  is intermolecular distance,  $\hbar$  is Plank constant,  $k_{\text{B}}$  is Boltzmann constant,  $T$  is temperature,  $k_{\text{ET}}$  is electron-transfer rate,  $t$  is transfer integral (intermolecular electronic coupling),  $\lambda$  is reorganization energy, and  $\Delta E$  is site-energy difference of initial and final state (which also depend on  $t$ ).<sup>136</sup> The eq (2) is so-call the Marcus equation,<sup>137</sup> which expresses that  $\mu_{\text{FET}}$  depends on  $\lambda$  and  $t$ .

Hopping process can be depicted as a model picture where an electron (or hole) is transferred from one molecule to the neighboring one. Figure 2.5.6 explains the transfer reaction when the carrier is hole (p-type). After the charge transfer, relaxation of the structure of each molecule (+1 charged and neutral) allows the molecule to take each optimal geometry of each charged state. The reorganization energy for hole ( $\lambda^{\text{h}}$ ) correspond to the sum of the two structural relaxation energies ( $\lambda^{\text{h}} = \lambda_{\text{rel}}^{(1)} + \lambda_{\text{rel}}^{(2)}$ ).<sup>138,139</sup> These two portions are typical nearly identical ( $\lambda^{\text{h}} \approx 2\lambda_{\text{rel}}$ ). The  $\lambda$  in fact gives a measure of energy loss (or hopping efficiency). More strictly,  $\lambda$  includes *intermolecular* reorganization energy, that is polarization energy and molecular vibration of surrounding molecules.<sup>136</sup> However, the *intermolecular*  $\lambda$  can be neglect because the value is expected to be much smaller than the *intramolecular*  $\lambda$ . That is why I consider only the *intramolecular*  $\lambda$ . Here I estimated *intramolecular*  $\lambda^{\text{h}}$  values on a isolated molecule based on the same DFT method (B3LYP/6-31G(d)). The  $\lambda^{\text{h}}$  values of the compounds are compared with each other in order to evaluate the hole transport ability.

On the other hand, transfer integral ( $t$ ) is electronic coupling between two molecules. The  $t$  is an energy gain when a charge is delocalized (or transferred) between two molecular orbitals. The meaning of  $t$  is similar to a resonance integral ( $\beta$ ) when two atomic orbitals give molecular orbital on the basis of linear combination of atomic orbitals (LCAO) approximation. Here I consider hole mobility, thus the  $t$  related to hole transport is important. That value can be estimated by considering interaction of HOMO of neutral dimer ( $t_{\text{HOMO}}$ , Figure 2.5.7).

The calculation of  $t_{\text{HOMOs}}$  in dimers in the crystals are based on DFT with the PW91 functional and Slater-type triple- $\zeta$  plus polarization (TZP) basis set by using a Amsterdam Density

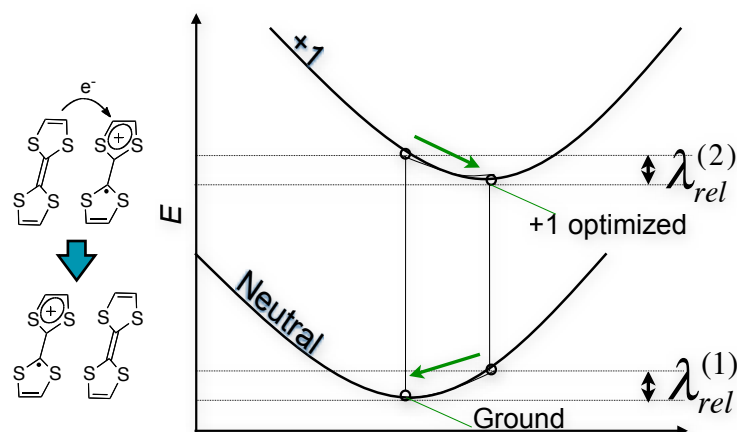


**Figure 2.5.6.** Explanation of hopping model and reorganization energy.

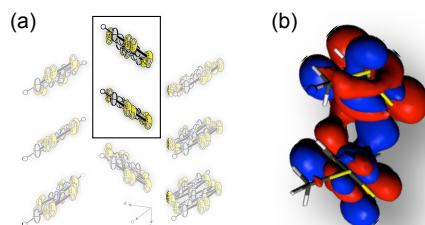


**Figure 2.5.7.** Explanation of calculation of a transfer integral. (a) A dimer is picked up from a crystal structure (b) Schematic image of the interaction of HOMOs in a crystal structure.

Functional (ADF) program package.<sup>138-141</sup> The ADF program gave plausible results as compared to the program based on the extend Hückel method developed by Mori *et al.*<sup>142,143</sup> The extend Hückel program tends to overestimate  $t_{\text{HOMO}}$  in the case of sulfur-containing compounds (see Supporting Information). It should be mentioned that the  $t_{\text{HOMOs}}$  in this report are absolute values,  $|t_{\text{HOMO}}|$ . The phase (+ or -) are neglected in order to discuss the strength of electronic coupling simply.

**Table 2.5.4.**  $\lambda^{\text{h}}$  on isolated molecules<sup>a</sup>.

		$\lambda_{\text{rel}}^{(1)} / \text{meV}$	$\lambda_{\text{rel}}^{(2)} / \text{meV}$	$\lambda^{\text{h}} / \text{meV}$
<b>1f</b>	<i>N-n</i> -cetyl-PyTTF	137	143	280
<b>2b</b>	<i>N-n</i> -hexanoyl-PyTTF	180	170	350
<b>3b</b>	methyl- $\alpha$ DT-TTF	130	125	255
<b>3c</b>	<i>n</i> -octylthio- $\alpha$ DT-TTF		<sup>b</sup>	
	DT-TTF	125	127	252
	TTF	142	137	279
	pentacene	48	49	97
	DNTT	67	63	130
	C <sub>12</sub> -BTBT	120	119	239
	HM-TTF	137	147	284

<sup>a</sup> calculated based on DFT with B3LYP/6-31G(d) basis set. <sup>b</sup> could not be calculated a appropriate value owing to take boat conformation during the calculation.

**Reorganization energy.** The calculated  $\lambda^{\text{h}}$  of the TTF derivatives ( $> 250$  meV) are higher than those of pentacene and DNTT ( $< 130$  meV) (Table 2.5.4). This is responsible for the general electronic character of TTF core, that is, the TTF has non-aromatic structure in the neutral state and gain aromaticity in the cationic state. Thus, the structural difference between the neutral and cationic states should be large. In addition, **2b** has larger  $\lambda^{\text{h}}$  (350 meV) than those of the other TTF derivatives, which is attributable to its large structural freedom caused by single bond in the conjugation. The high  $\lambda^{\text{h}}$ s of the TTF compounds could cause low  $\mu_{\text{FETS}}$  of the heteroaromatic-fused TTFs. HM-TTF and C<sub>12</sub>-BTBT, nevertheless, also have high  $\lambda^{\text{h}}$ s  $\sim 250$

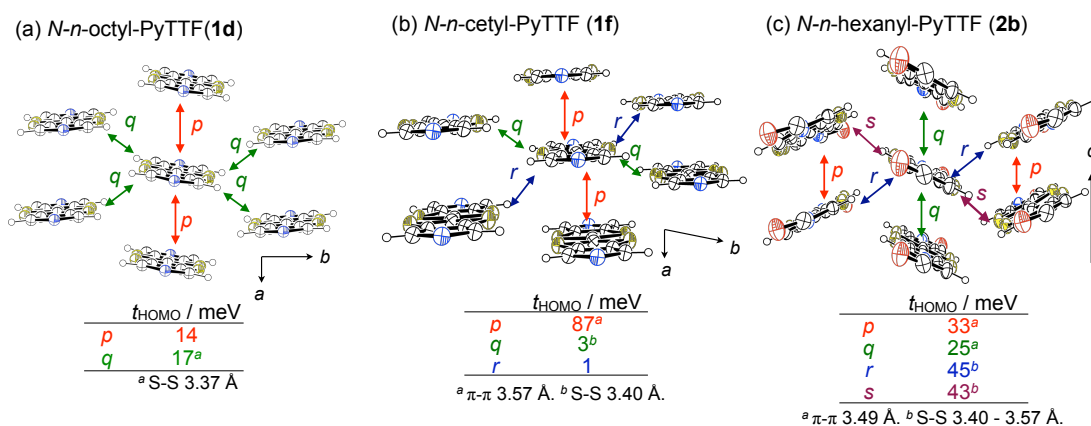


**Figure 2.5.8.** Molecular arrangement viewed along long-molecular axis together with transfer integrals of (a) **1d**, (b) **1f**, and (c) **2b** (alkyl moieties are omitted for clarity).

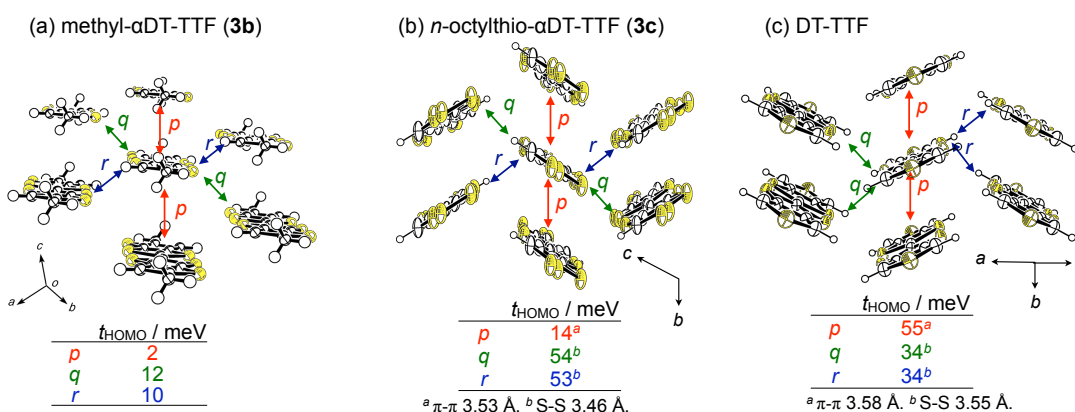


**Figure 2.5.9.** Molecular arrangement viewed along long-molecular axis together with transfer integrals of (a) **3b**, (b) **3c**, and (c) DT-TTF (alkyl moieties are omitted for clarity).

meV. These facts indicate a relationally small contribution of  $\lambda^{\text{h}}$  to  $\mu_{\text{FET}}$ , which may be related to small  $\lambda^{\text{h}}$  in actual solid state, because molecules are embedded into surrounding molecular lattice.<sup>130</sup>

**Transfer Integrals in Crystal Structures.** The calculated  $t_{\text{HOMO}}$  values are shown in figures of crystal structures viewed along the molecular-long axis direction (Figure 2.5.8 - 2.5.9). Intermolecular interactions related to FET characteristics can be expressed with interactions between the surrounding six molecules for most cases. In addition, the six interactions frequently include the identical pair(s) owing to the crystallographic symmetry. Thus, the interaction can be explained, in general, with two transverse (S-S) directions and one perpendicular ( $\pi$ -staking) direction.

For **1d** that gives no FET response with low  $I_{\text{d}}$  current, very small  $t_{\text{HOMOS}}$  ( $< 22$  meV) are found in all directions (Figure 2.5.8a). In contrast, the large  $t_{\text{HOMOS}}$  (87 meV) is found along the  $\pi$ -staking direction (designated as *p*) for **1f** that give moderate  $\mu_{\text{FETS}}$  (Figure 2.5.8b). These results are reasonable to consider the relation between the structure and properties of the FET characteristics. This result also indicates very weak electronic interactions at the transverse direction, in which S-S short contacts are present ( $q = 17$  meV for **1d**,  $q = 3$  meV for **1f**). The small interaction is probably explained for the slipping  $\pi$ -cores along the molecular long-axis, and thus HOMOs on the sulfur atoms do not spread over the molecules in such direction. The calculation asserts that not all S-S short contacts give electronic interaction.

## 2. Development of Heteroaromatic-fused TTFs

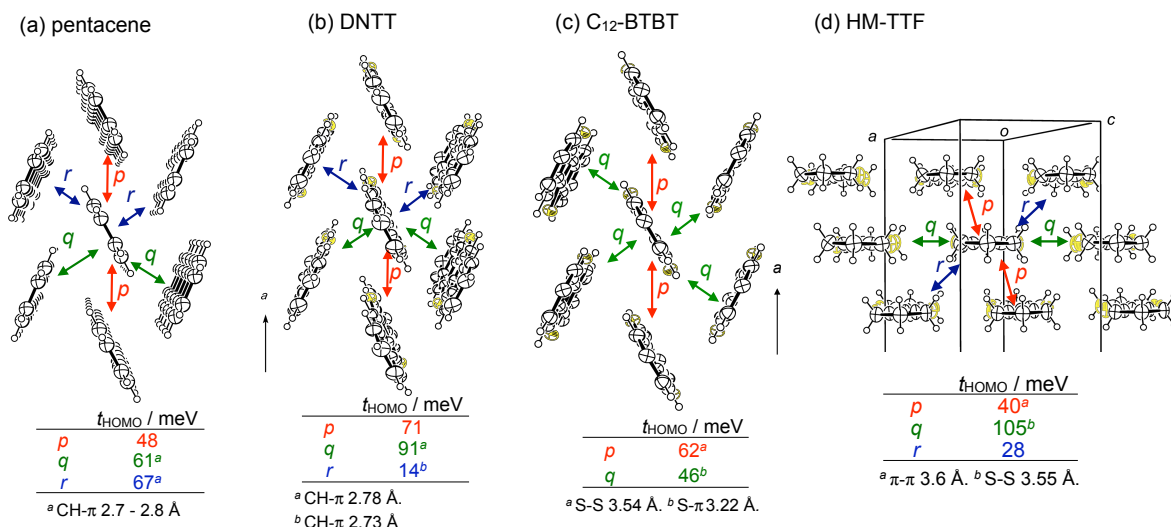


**Figure 2.5.10.** Molecular arrangement viewed along long-molecular axis together with transfer integrals of (a) pentacene, (b) DNNT, (c) C<sub>12</sub>-BTBT (alkyl moieties are omitted for clarity), and (d) HM-TTF.

In the structure of **2b**, moderate  $t_{\text{HOMOS}}$  (25 - 45 meV) in all directions are calculated in the herringbone-like structure (Figure 2.5.8c). The isotropic electronic coupling within the  $\pi$ -core layer ought to form 2-D conducting layer parallel to the substrate. This is contrasted to the structure of **1f** which has 1D intermolecular interaction. With considering the better  $\mu_{\text{FETS}}$  of **2b** than those of **1f**, 2-D electronic structure is suitable for thin-film OFETs.<sup>14b</sup> This is in good agreement with the 2-D electronic structure in pentacene film (Figure 2.5.10a).

Calculation of transfer integrals of thiophene-fused TTFs also show good agreement with the FET characteristics (Figure 2.5.9). Very small  $t_{\text{HOMOS}}$  (< 12 meV) were calculated for **3b** that gives no FET characteristics. In contrast, moderately large  $t_{\text{HOMOS}}$  ( $q$  and  $r = 54$  meV) in **3c** were calculated along the transverse directions. Similar  $t_{\text{HOMOS}}$  were calculated in the DT-TTF packing structure along the  $\pi$ - $\pi$  interaction ( $p = 55$  meV), in addition to moderate transverse interaction ( $q$  and  $r = 34$  meV). The 2-D electronic interaction with moderately large  $t_{\text{HOMOS}}$  for **3c** and DT-TTF is consistent with their good  $\mu_{\text{FETS}} \sim 0.3 \text{ cm}^2/\text{Vs}$ .

On the other hand, the high performance materials such as pentacene, DNNT, C<sub>12</sub>-BTBT, and HM-TTF has generally larger  $t_{\text{HOMOS}}$  than those in the present heteroaromatic-fused TTF (Figure 2.5.10). Pentacene and C<sub>12</sub>-BTBT have the moderately large  $t_{\text{HOMOS}}$  (ca. 50 - 65 meV) in all directions in the solid states. DNNT has large  $t_{\text{HOMOS}}$  along the two directions ( $p = 71$  meV and  $q = 91$  meV). Pentacene, C<sub>12</sub>-BTBT, and DNNT are estimated to form 2-D conducting layers with strong electronic coupling. For HM-TTF, a very large  $t_{\text{HOMO}}$  ( $q = 105$  meV) along the transverse direction and a moderate  $t_{\text{HOMO}}$  ( $p = 40$  meV) along the  $\pi$ -stacking direction are calculated, indicating the formation of a 1-D-like quasi 2-D electronic structure (*vide infra*).

Regardless of the kind of material, the present calculations of  $t_{\text{HOMOS}}$  indicate that  $t_{\text{HOMOS}}$  in the solid state is well-correlated with  $\mu_{\text{FETS}}$  of OFETs, having polycrystalline thin-film channel with grain boundaries. First, a 2-D semi-conducting layer is necessary for high  $\mu_{\text{FETS}}$ , which is achieved by  $t_{\text{HOMOS}}$  more than 20 meV along more than two directions. In other words, field-effect response in the thin-film-based OFETs seems to require  $t_{\text{HOMO}}$  at least  $\sim 20$  meV, which might be boarder region of whether carriers hop or not between molecules beyond the energy barrier such as  $\lambda^{\text{h}}$  and or other carrier traps. Second, stronger electronic coupling give higher  $\mu_{\text{FET}}$ , in which a ca. 60 meV of  $t_{\text{HOMO}}$  in one direction appears to correspond to  $\mu_{\text{FETS}}$  1  $\text{cm}^2/\text{Vs}$ .

**Discussion for Developing Semiconductors for OFETs.** The experimental and theoretical evaluations suggest that the lower mobility of the OFETs based on the heteroaromatic-fused

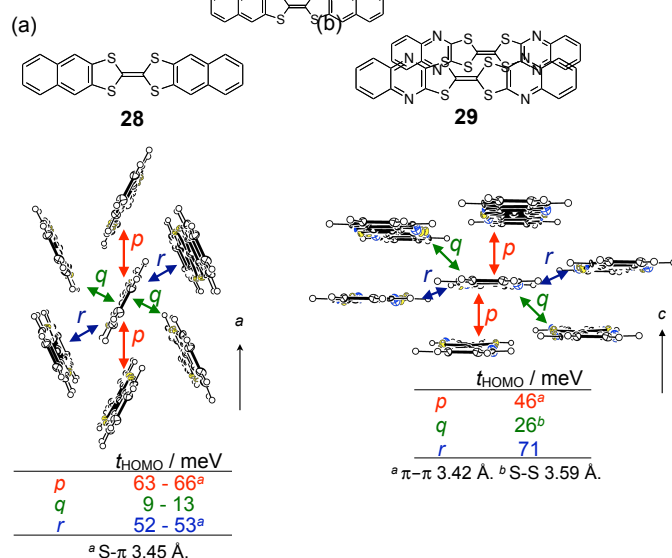


**Figure 2.5.11.** Structures and molecular arrangements viewed along the molecular-long-axis with calculated  $t_{\text{HOMO}}$  values: (a) Naphthalene-fused TTF (**28**). (b) Quinoxaline-fused TTF (**29**).

TTFs than that based on the high performance semiconductors is ascribed to the smaller  $t_{\text{HOMO}}$  values in the solid states. The  $t_{\text{HOMOS}}$  are much smaller than those expected from the existence of short S-S contacts for **2b**, **3c**, and DT-TTF. I suggest that their packing fashion (can be classified into  $\theta$ -type, Figure 2.1.8) is disadvantageous to take electronic coupling between TTF cores. On the basis of these results and consideration, I shall suggest a strategies for molecular design of TTF-based materials as follows.

*DNTT type: herringbone packing.* High performance acene and heteroacene-based semiconductors are packed in herringbone fashion. The densely packed herringbone structure driven by the CH- $\pi$  pseudo-hydrogen bonds should be one of the most promising strategy for large  $t_{\text{HOMOS}}$  with neighboring molecules to give 2-D semi-conducting layers. In general, a molecule having benzene ring tend to take the herringbone structure. For instance, naphthalene-fused TTF (**28**) is packed in the herringbone fashion in the solid state (Figure 2.5.11a).<sup>91</sup> The calculated  $t_{\text{HOMOS}}$ , nevertheless, are moderate with  $\sim 50$  meV in all directions. In this case, fused benzene rings probably perturb the S-S interactions sterically. Accordingly, the  $\mu_{\text{FETS}}$  of OFETs based on **28** are up to 0.4 cm<sup>2</sup>/Vs, which indicate that the strategy for herringbone structure seems to be unsuitable for TTF derivatives.

*HM-TTF type:  $\pi$ -stacking.* It is remarkable that HM-TTF has the large  $t_{\text{HOMOS}}$  (105 meV). The large  $t_{\text{HOMO}}$  is found in the S-S contact direction, in spite of the longer S-S distance (3.55 Å) than those in **2b** or **3c**. This fact indicates the importance of relative position of the  $\pi$ -cores (vide supra for **1d** and **1f**). In addition, the highly conductive charge-transfer salts based on TTF derivative so far reported are often packed with  $\pi$ -stacking structure (so-call  $\beta$ -sheet structure) rather than the herringbone-like  $\theta$ -type structure.<sup>73,143</sup> Therefore, the  $\pi$ -stacking structure seems to be suitable for TTF derivatives to realize high  $\mu_{\text{FET}}$ . For the formation of  $\pi$ -stacking structure, introducing bulky substituents into a molecule is one of the potential strategies (see Figure 2.1.6).<sup>49</sup> On the other hand, the other strategy includes annulation of electron-deficient moiety such as nitrogen-containing ring. For instance, quinoxaline-fused TTF (**29**) formed  $\pi$ -stacking structure (Figure 2.5.11b). This molecular design strategy is in agreement with decrease in  $E_{\text{HOMO}}$  for improving air-stability. However, polarization in molecules often gives low solubility<sup>75</sup> and unpredictable structures in the solid state owing to local interaction between electron-donating and accepting moieties.<sup>72,144</sup> In fact the OFETs based on **29** showed the moderate  $\mu_{\text{FETS}}$

(0.2 cm<sup>2</sup>/Vs), relating to the packing slipped along to the molecular long axis. A molecular structure should be designed carefully.

**Summary.** The electronic structure of the heteroaromatic-fused TTFs are determined experimentally and theoretically. Evaluations on molecular characteristics relating to hole transport in terms of coefficients and energy levels of HOMO and reorganization energy suggest that the energy level should be decreased to obtain air-stable operation, and relatively high  $\lambda^h$  can be attributed to low  $\mu_{\text{FET}}$ . However, the molecular electronic structures are not correlated with  $\mu_{\text{FET}}$  strongly. On the other hand, calculated electronic structures in the solid state, transfer integrals for HOMO ( $t_{\text{HOMO}}$ ), indicated that the  $\mu_{\text{FETS}}$  of thin-film-based OFETs can be well-correlated to the  $t_{\text{HOMOS}}$ . The  $t_{\text{HOMOS}}$  larger than ~25 meV in more than two direction seem to be a critical factor for high performance materials as indicated by **2b**, **3c**, and DT-TTF. The  $t_{\text{HOMOS}}$  in **2b**, **3c**, and DT-TTF are, however, lower than those of the state-of-the-art high performance materials. This result means that the intermolecular interaction between TTF cores is rather smaller than those expected from the packing structure, where S-S short contacts and/or  $\pi$ -stacking are present. It indicates that the present heteroaromatic-fused TTF core is not suitable for the present molecular design. Another molecular design strategy is necessary for developing further better TTF-based semiconductors.

## Supporting Information

**Transfer Integrals calculated based on an Extend Hückel method.** Transfer integrals in **1f**, **2b**, and DT-TTF were calculated by using a program developed by Mori *et al.*, which are shown in Table 2.5.4. The program calculates overlap integral for HOMO, and then transfer integrals ( $t_{\text{HOMOS}}$ ) are calculated by the following equation:  $t_{\text{HOMO}} = -10 \times S_{\text{HOMO}}$  (eV). Parameters in the extend Hückel calculation is shown in Table 2.5.5.

The calculated  $t_{\text{HOMOS}}$  show similar tendency with those calculated by DFT method. The value of  $t_{\text{HOMOS}}$ , however, tends to have large values in the direction of side-by-side S-S directions. For instance, **1f** was calculated to be relatively large interaction (53 meV) in the direction of S-S contact (designated by  $q$ ), in contrast to quite few value (3 meV) calculated by the DFT method.

**Table 2.5.4** Transfer integrals calculated by extend Huckel program

molecule	contact <sup>a</sup>	$t$ (meV)
<b>1f</b>	$p$	-135
	$q$	53
	$r$	0.08
<b>2b</b>	$p$	-40
	$q$	-45
	$r$	-47
	$s$	-45
DT-TTF	$p$	30
	$q$	47
	$r$	50

<sup>a</sup>Contact directions are equal to 2.5.8 and 2.5.9.

**Table 2.5.5.** Parameters in extend Huckel transfer integral calculations

atom	orbital	Slater exponent $\zeta$	ionization potential
S	3s	2.122	-1.47
	3p	1.827	-0.808
	3d	1.5	-0.4
O	2s	2.275	-2.38
	2p	2.275	-1.09
N	2s	1.95	-0.191
	2p	1.95	-0.990
C	2s	1.625	-1.573
	2p	1.625	-0.838
H	1s	1.0	-1.0

## 2.6. Conclusion for Chapter 2

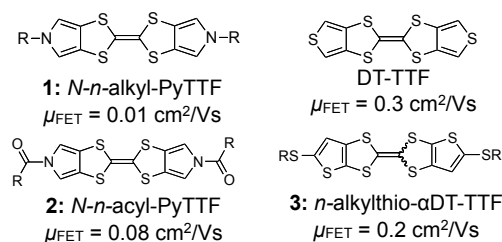


**Figure 2.6.1.** Heteroaromatic-fused TTFs with their  $\mu_{\text{FET}}$ s as high as obtained.

I designed, synthesized, and characterized a series of heteroaromatic-fused TTFs as semiconductors for OFETs (Figure 2.6.1, with the highest  $\mu_{\text{FET}}$ s obtained). This study successfully demonstrated the promising molecular design for solution-processible semiconductors (**1** and **3**). The small and cohesive TTF-cores with long alkyl chains along the  $\pi$ -core are highly soluble, and formed layer-by-layer structures on the substrates with spin-coat process. The longer alkyl derivatives showed the better FET characteristics than those of short or unsubstituted derivatives, which completely agreed with the well-ordered layer-by-layer structure of the latter suitable for OFET operations. In the solid-state structures, 2-D intermolecular interactions between the TTF-cores via  $\pi$ - $\pi$  and/or S-S interactions can be observed. In addition, the hydrophobic interaction between the long alkyl chains effected the large overlaps between the TTF-cores.

On the other hand, the drawbacks of the heteroaromatic-fused TTFs are mainly two fold; incompatibility of solubility with air-stability (**2**) and the relatively low  $\mu_{\text{FET}}$ s of the devices as compared to those of the state-of-the-art high performance semiconductors. The elucidation of the electronic structures indicates that the weaker electronic couplings between the TTF-cores in the solid states than expected from the 2-D packing structures is most likely responsible. However, the strategy described here is utilized in other  $\pi$ -cores, and gave the high performance semiconductors for both solution-process<sup>124</sup> and vacuum-process<sup>22</sup> (Chapter 3). Although **1-3** were not used in the following study owing to the inferior performances, TTF derivatives are still excellent candidates for high performance semiconductors and very interesting as research subjects.

## 2. Development of Heteroaromatic-fused TTFs

## Chapter 3

### Evaluation of C<sub>10</sub>-DNTT as a Organic Semiconductor for High Performance Thin-Film Transistors

#### 3.1 Introduction for Alkylated DNTT

Organic thin-film transistors (OTFTs) have attracted interest because of the possibility for realizing flexible electronic devices.<sup>5</sup> Among the many organic semiconductors reported so far, pentacene is the most common organic semiconductors as it shows the highest field effect mobility ( $\mu_{\text{FET}} > 3.0 \text{ cm}^2/\text{Vs}$ ).<sup>48,145-147</sup> On the other hand, Takimiya's group has developed several new heteroacene-based organic semiconductors that show high  $\mu_{\text{FET}}$  in the TFT configuration: 2-7-diphenyl[1]benzothieno[3,2-*b*]benzothiophene (DPh-BTBT,  $2.0 \text{ cm}^2/\text{Vs}$ ),<sup>148</sup> dinaphtho[2,3-*b*:2'3'-*f*]thieno[3,2-*b*]thiophene (DNTT)<sup>17</sup>, and alkylated BTBTs (C<sub>*n*</sub>-BTBT,  $3.9 \text{ cm}^2/\text{Vs}$ )<sup>124</sup> (Figure 3.1.1).

DNTT has been reported as the high performance and air-stable vacuum-processed organic semiconductor. Flexible transistors and integrated circuits based on DNTT have been reported.<sup>18</sup> Some people call DNTT as *post-pentacene* due to the reproducible and the stable high performance. On the other hand, C<sub>*n*</sub>-BTBT was developed along with the same molecular design-strategy as the heteroaromatic-fused TTFs (comparison of the characteristics was discussed in section 2.5), which has long alkyl chains along the  $\pi$ -core. The alkyl chains can act as the driving force for molecular ordering in solid state owing to the van der Waals intermolecular interaction between the alkyl groups, or the so-called molecular fastener effect, that renders the semiconducting core to pack tightly, thereby enhancing carrier mobility (Figure 3.1.2).<sup>125</sup> The application of the molecular design strategy to the DNTT framework is considered to be a promising approach for much higher performances and solution-processible organic semiconductors.

M. J. Kang in Takimiya's group synthesized di-*n*-alkyl-substituted DNTT (C<sub>*n*</sub>-DNTT) and investigated their basic properties and characteristics. Although C<sub>*n*</sub>-DNTT has low solubility, vacuum-processed C<sub>*n*</sub>-DNTT-based TFT devices showed higher performances than those based on DNTT. In particular, di-*n*-decyl-DNTT (C<sub>10</sub>-DNTT) gives the highest mobility over  $5 \text{ cm}^2/\text{Vs}$  at least. However, our conventional device configuration is somewhat inappropriate in evaluating such high mobility organic semiconductors as C<sub>10</sub>-DNTT, owing to over estimation of drain-current ( $I_d$ ) thereby field-effect mobility ( $\mu_{\text{FET}}$ ). Furthermore, TFT characteristics of C<sub>10</sub>-DNTT-based devices on plastic substrates should be interesting. Although many of organic semiconductors that show high performances on the silicon substrates have been reported so far, demonstrating high performance OTFTs with  $\mu_{\text{FETS}}$  over  $1 \text{ cm}^2/\text{Vs}$  on flexible substrates is very

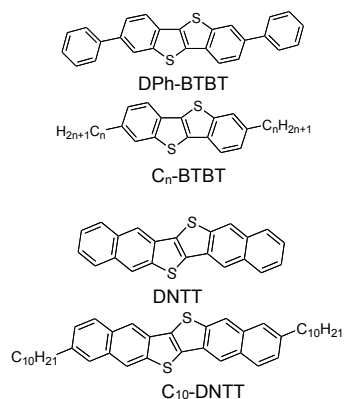


**Figure 3.1.1.** Structure of the heteroacene-based semiconductors.

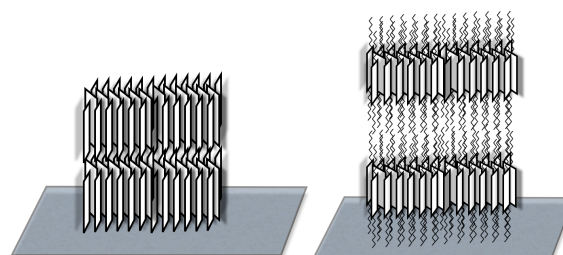


**Figure 3.1.2.** Schematic representation of the molecular orientation on Si/SiO<sub>2</sub> substrates (a) for DNTT (b) for alkylated DNTT.

### 3. Evaluation of C<sub>10</sub>-DNTT

limited; pentacene is in fact almost only the semiconductor that well evaluation on plastic substrates.

In this chapter, evaluation of a high performance C<sub>10</sub>-DNTT semiconductor is described: first, I improved the device structure by designing new shadow masks, and determined the  $\mu_{\text{FETS}}$  on the silicon substrate. Second, I established fabrication and evaluation system of polymer dielectrics on the plastic substrates. Finally, the high performance C<sub>10</sub>-DNTT-based OTFTs on plastic substrates are demonstrated.

### 3.2 Evaluation on Silicon Substrates

**Designing Shadow Mask.** Our conventional top-contact/bottom-gate device with a parallel S/D electrode configuration is fabricated by deposition of gold source-drain electrode through a shadow mask on the organic thin film coated over the substrate (Figure 3.2.1). The conventional device system is easy to fabricate many devices in one deposition (12 arrays, 3 devices of each array). However, it has some problems. First, fringe current may give overestimation of  $\mu_{\text{FET}}$  (Figure 3.2.2).<sup>149</sup> Second, large areas of electrodes ( $\sim 1.5 \text{ mm}^2$  for each) often brings large off-current and frequently give rise breakdown when voltage is applied to the device.<sup>150</sup> Third, the channel is defined with tungsten wires, which gives inaccurate channel width ( $W$ ) and ( $L$ ). The rough shadow mask also prohibits fabrication of multi-layer electrodes, e.g., a  $\text{MoO}_3$  injection-layer beneath the Au electrode.<sup>151</sup>

I designed a new device structure shown in Figure 3.2.3 to address these issues. This device geometry needs two masks; for the organic layer and for the S-D electrodes. The organic mask defines the organic layers in a square shape. The width of organic layer regulates the width of channel region  $W$  of a device with this comb-type electrode structure. Therefore, overestimation of  $\mu_{\text{FETS}}$  caused by the fringe current can not occur with this device geometry. The separated organic layer also contributes lowering the off-current ( $I_{\text{off}}$ ) because it can exclude leakage currents generated in the other organic region. The area of S-D electrode of this device ( $\sim 0.6 \text{ mm}^2$  for each) is smaller than that of our conventional one, which contributes to reduce  $I_{\text{off}}$  significantly and prevent dielectric breakdown. In particular, the  $I_{\text{off}}$  can be minimized when gate-electrodes are patterned, which is quite important for fabrication of devices on polymer dielectrics (see section 3.3 and 3.4). On one substrate, 10 devices can be fabricated by using the mask with various  $L$  (20, 40, 90, 140, and 190  $\mu\text{m}$ , measured) and  $W$  (1500  $\mu\text{m}$ ) dimensions, which allows evaluation of the contact and channel resistance of the devices separately. Eight squares ( $2 \text{ mm} \times 2 \text{ mm}$  dimension) on the side of the pattern are metal-insulator-metal (MIM) devices for capacitance-measurement and metal-insulator-semiconductor-metal (MIS) devices for I-V characteristics of semiconductors, respectively. The shadow mask is made of stainless (SUS304-H). Its moderately magnetic character allows the mask to stick to a substrate that placed on a piece of strong neodymium magnets. This is important for ease of the fabrication of devices and preventing a damage to the mask during the peeling.

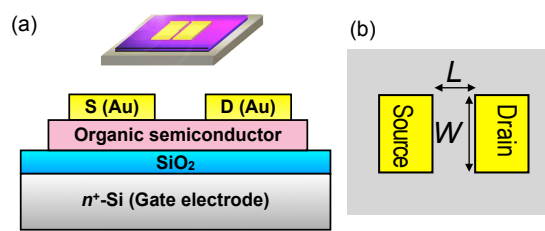


**Figure 3.2.1.** Schematic representation of the conventional OFET device (a) structure (b) top-view of source-drain electrodes. Channel width ( $W$ ) and length ( $L$ ) are 1500  $\mu\text{m}$  and 50  $\mu\text{m}$ , respectively.

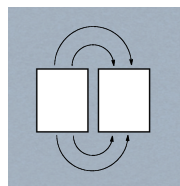


**Figure 3.2.2.** Schematic image fringe current.

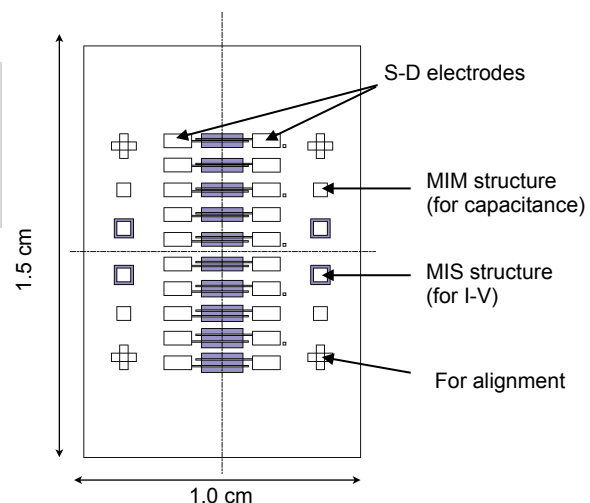


**Figure 3.2.3.** New designed device. Shadow area represents organic layer.

**Table 3.2.1** Characteristics of DNTT<sup>a</sup>-based OFET devices fabricated by the conventional mask ( $W = 1500 \mu\text{m}$ ,  $L = 50 \mu\text{m}$ ).

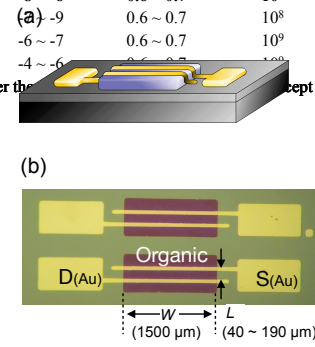
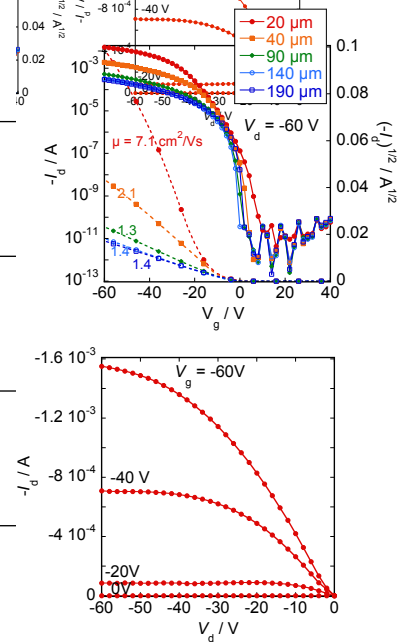
substrate <sup>b</sup>	$L / \mu\text{m}$	$V_{\text{th}} / \text{V}$	$\mu / \text{cm}^2\text{V}^{-1}\text{s}^{-1}$	$I_{\text{on}}/I_{\text{off}}$
bare Si/SiO <sub>2</sub> <sup>c</sup>	50	-10 ~ +6	0.015 ~ 0.57	10 <sup>3</sup>
OTS	50	-16 ~ -4	1.2 ~ 2.2	10 <sup>7</sup>
ODTS	50	-18 ~ 0	0.48 ~ 1.1	10 <sup>6</sup>
HMDS	50	-32 ~ -10	0.59 ~ 1.0	10 <sup>6</sup>
$\beta$ -PTS	50	+5 ~ +26	0.034 ~ 0.011	10 <sup>5</sup>
PTS	50	+2 ~ +11	0.029 ~ 0.055	10 <sup>5</sup>

<sup>a</sup> Purified by sublimated twice after the Soxhlet extraction. Deposition rate ( $R_{\text{dep}}$ ) was  $1.5 \sim 2.0 \text{ \AA/s}$ . <sup>b</sup>  $T_{\text{sub}} = 60 \text{ }^\circ\text{C}$ , except for <sup>c</sup> at r.t.. See Experimental Procedures for treated reagents.

**Table 3.2.2.** Characteristics of DNTT<sup>a</sup>-based OFET devices fabricated by the new mask ( $W = 1500 \mu\text{m}$ ).

substrate <sup>b</sup>	$L / \mu\text{m}$	$V_{\text{th}} / \text{V}$	$\mu / \text{cm}^2\text{V}^{-1}\text{s}^{-1}$	$I_{\text{on}}/I_{\text{off}}$
bare Si/SiO <sub>2</sub> <sup>c</sup>	20	-6 ~ -8	0.6 ~ 0.8	10 <sup>8</sup>
	<b>40</b>	<b>-7 ~ -9</b>	<b>0.4 ~ 0.5</b>	<b>10<sup>8</sup></b>
	90	-7 ~ -8	0.3 ~ 0.4	10 <sup>7</sup>
	140	-7 ~ -8	0.4 ~ 0.5	10 <sup>7</sup>
	190	-7 ~ -8	0.4 ~ 0.5	10 <sup>7</sup>
OTS	20	-11 ~ -14	4.4 ~ 7.1	10 <sup>9</sup>
	<b>40</b>	<b>-4 ~ -7</b>	<b>1.9 ~ 2.1</b>	<b>10<sup>9</sup></b>
	90	-7	1.3 ~ 1.9	10 <sup>9</sup>
	140	-7	1.3 ~ 1.4	10 <sup>8</sup>
	190	-5 ~ -7	1.4 ~ 1.5	10 <sup>9</sup>
ODTS	20	+6 ~ +8	0.2	10 <sup>6</sup>
	<b>40</b>	<b>+1 ~ +4</b>	<b>0.1</b>	<b>10<sup>6</sup></b>
	90	-13 ~ +1	0.1 ~ 0.2	10 <sup>6</sup>
	140	-6 ~ +1	0.1 ~ 0.2	10 <sup>7</sup>
	190	+1 ~ +3	0.1	10 <sup>6</sup>
HMDS	20	-6 ~ -5	0.9 ~ 1.1	10 <sup>8</sup>
	<b>40</b>	<b>-8 ~ -6</b>	<b>0.6 ~ 0.7</b>	<b>10<sup>7</sup></b>
	90	-7 ~ -9	0.6 ~ 0.7	10 <sup>8</sup>
	140	-6 ~ -7	0.6 ~ 0.7	10 <sup>9</sup>
	190	-4 ~ -6	0.6 ~ 0.7	10 <sup>9</sup>

<sup>a</sup> DNTT was sublimated twice after the Soxhlet extraction.  $R_{\text{dep}} = 1.5 \sim 2.0 \text{ \AA/s}$ . <sup>b</sup>  $T_{\text{sub}} = 60 \text{ }^\circ\text{C}$ , except for <sup>c</sup> at r.t.

**Figure 3.2.4.** (a) Schematic representation of the device (b) a top view of the TFTs.**Figure 3.2.5.** Characteristics of DNTT-based OTFT on OTS-treated Si/SiO<sub>2</sub> substrates fabricated by the new designed mask. (a) Transfer (b) Output characteristics.

**Characteristics of DNTT-based OTFTs.** In order to examine the new shadow mask, I fabricated the OFET devices with DNTT using both conventional mask (old ones) and newly designed mask (new ones, Figure 3.2.4). The old ones showed typical p-type performances with  $\mu_{\text{FETS}}$  up to  $2.2 \text{ cm}^2/\text{Vs}$  on the octyltrichlorosilane (OTS)-treated Si/SiO<sub>2</sub> substrates (Table 3.2.1, see Experimental Procedures, Figure 3.2.8). On the other hand, the new ones  $L = 40 \mu\text{m}$  fabricated by the same conditions gave  $\mu_{\text{FETS}}$  up to  $2.1 \text{ cm}^2/\text{Vs}$  and on-off ratio ( $I_{\text{on}}/I_{\text{off}}$ ) of ca.  $10^9$  (Table 3.2.2, in bold). Although the calculated  $\mu_{\text{FETS}}$  of both devices are similar to each other, the device-to-device deviation regarding to the  $\mu_{\text{FETS}}$  and the threshold voltages ( $V_{\text{th}}$ ) of the new ones are smaller, and  $I_{\text{on}}/I_{\text{off}}$  of the new ones are higher by  $\sim 10^2$  than those of the old ones (Table 3.2.2). Additionally, the drain-current ( $I_d$ ) of the new one increased rapidly in the transfer char-

acteristics (Figure 3.2.5), which is better than those of the old ones. The characteristics of the devices with  $L = 20 \mu\text{m}$ , however, lack reproducibility. The short  $L$  devices frequently gave high  $I_{\text{off}}$  ( $\sim 10^8$ ) and short circuits (the S-D electrodes are connected). These fact indicates that such a small gap by  $20 \mu\text{m}$  is difficult to achieve reproducibly with the technique using the shadow mask, although the extracted  $\mu_{\text{FETs}}$  up to  $7 \text{ cm}^2/\text{Vs}$  in the devices with  $L = 20$  is very interesting. I concluded that the newly designed mask could give reliable devices, except for the ones with  $L = 20 \mu\text{m}$ .

**Characteristics of  $\text{C}_{10}$ -DNTT-based OTFTs.**  $\text{C}_{10}$ -DNTT-based OFET devices were fabricated for several times under the conditions that Kang optimized; substrate temperature ( $T_{\text{sub}}$ ) of  $60 \text{ }^\circ\text{C}$  and deposition rate ( $R_{\text{dep}}$ ) of ca.  $0.1 \text{ \AA}/\text{s}$ . Table 3.2.3 and Figure 3.2.6 summarize the characteristics of the devices. The  $\text{C}_{10}$ -DNTT-based devices showed higher performances than those of DNTTs with  $\mu_{\text{FETs}}$  more than  $2 \text{ cm}^2/\text{Vs}$  regardless of the dielectric surfaces; bare, OTS, octa-

**Table 3.2.3.** Characteristics of  $\text{C}_{10}$ -DNTT-based OTFT devices fabricated by the new mask ( $W = 1500 \mu\text{m}$ )<sup>a</sup>.

substrate	$L / \mu\text{m}$	$V_{\text{th}}^b / \text{V}$	$\mu_{\text{FET}}^b / \text{cm}^2\text{V}^{-1}\text{s}^{-1}$	$I_{\text{on}}/I_{\text{off}}$
bare Si/SiO <sub>2</sub>	40	-20 ~ -13 [-16]	2.3 ~ 2.7 [2.9]	10 <sup>9</sup>
	90	-17 ~ -7 [-13]	2.0 ~ 3.7 [2.8]	10 <sup>8</sup>
	140	-15 ~ -10 [-13]	2.3 ~ 3.4 [2.8]	10 <sup>9</sup>
	190	-16 ~ -7 [-12]	2.2 ~ 3.3 [2.8]	10 <sup>8</sup>
OTS	40	-17 ~ -3 [-9]	2.0 ~ 3.9 [3.0]	10 <sup>9</sup>
	90	-15 ~ -3 [-9]	2.8 ~ 3.2 [3.0]	10 <sup>9</sup>
	140	-14 ~ -3 [7]	2.5 ~ 3.4 [3.0]	10 <sup>8</sup>
	190	-12 ~ 3 [-6]	2.5 ~ 3.7 [3.4]	10 <sup>9</sup>
ODTS	40	-24 ~ -6 [-14]	3.4 ~ 4.9 [4.0]	10 <sup>9</sup>
	90	-19 ~ -3 [-13]	4.2 ~ 6.5 [5.7]	10 <sup>10</sup>
	140	-21 ~ +1 [-12]	4.9 ~ 7.6 [6.9]	10 <sup>10</sup>
	190	-15 ~ +1 [-5]	6.6 ~ 7.8 [7.3]	10 <sup>9</sup>
HMDS	40	-20 ~ 0 [-13]	2.3 ~ 3.5 [2.9]	10 <sup>9</sup>
	90	-12 ~ -1 [-8]	1.8 ~ 2.8 [2.3]	10 <sup>9</sup>
	140	-9 ~ -1 [-6]	1.8 ~ 3.1 [2.5]	10 <sup>9</sup>
	190	-7 ~ +1 [-4]	2.3 ~ 3.1 [2.6]	10 <sup>9</sup>

<sup>a</sup>  $T_{\text{sub}} = 60 \text{ }^\circ\text{C}$ ,  $R_{\text{dep}} = 1.5 \sim 2.0 \text{ \AA}/\text{s}$ .  $\text{C}_{10}$ -DNTT was sublimed twice before use.

<sup>b</sup> Average values are in the parentheses.

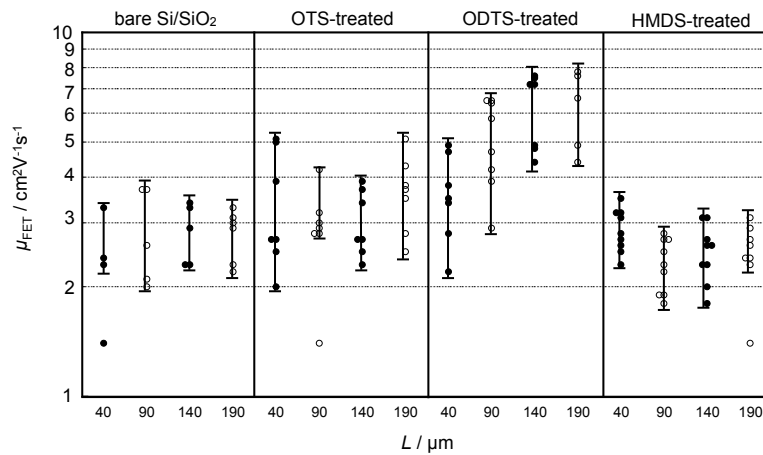


**Figure 3.2.6.** Distribution map of the extracted  $\mu_{\text{FETs}}$  of  $\text{C}_{10}$ -DNTT-based OTFTs.

### 3. Evaluation of C<sub>10</sub>-DNTT

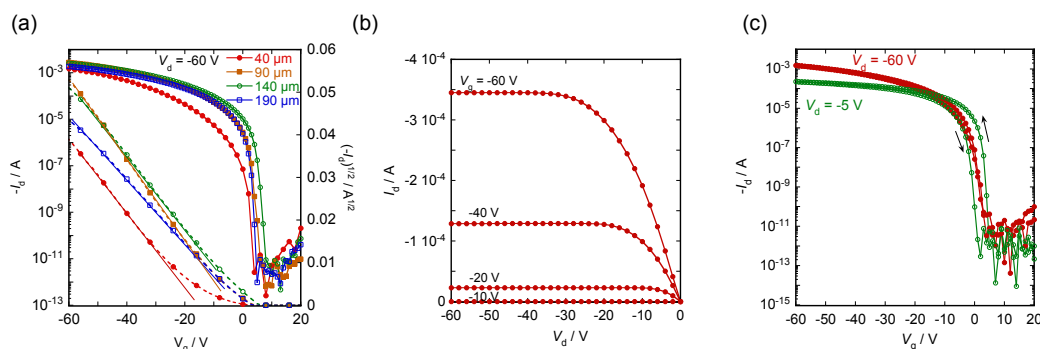


**Figure 3.2.7.** Characteristics of C<sub>10</sub>-DNTT-based devices. (a) Transfer characteristics in saturation regime with various  $L$ . The extracted  $\mu_{\text{FET}}$  from the transfer are 2.8, 6.4, 7.6, 7.8 cm<sup>2</sup>/Vs at  $L$  are 40, 90, 140, 190 μm, respectively. (b) Output characteristic of device with  $L = 190$  μm. (c) Hysteresis of transfer characteristics in the linear ( $V_d = -60$  V, red line with filled circle) and saturate ( $V_d = -5$  V, green line with open circle) region. The  $\mu_{\text{FETS}}$  is calculated to be 5.1 cm<sup>2</sup>/Vs in linear region.

decyltrichlorosilane (ODTS), and hexamethylenedisilazane (HMDS)-treated Si/SiO<sub>2</sub>. It is interesting to note that the devices on ODTS-treated substrate showed pronounced increase of  $\mu_{\text{FET}}$  with increasing  $L$ , the  $\mu_{\text{FET}}$  reaches more than 7.0 cm<sup>2</sup>/Vs, and the highest observed  $\mu_{\text{FET}}$  is 7.8 cm<sup>2</sup>/Vs with quite small hysteresis in the saturate region (Figure 3.2.7). This very high mobility difference can be ascribed to better molecular ordering on the ODTS substrate, effectively reducing the channel resistance between the S and D electrodes. In case of the short  $L$  devices on the ODTS-treated substrates, it is expected that relatively large contact-resistance limits the  $I_d$  of the on-state, resulting in the lower  $\mu_{\text{FETS}}$  calculated from the device characteristics.<sup>152</sup> These unique characteristics are in good agreements with those of devices fabricated by Kang, which showed  $\mu_{\text{FETS}}$  up to 7.9 cm<sup>2</sup>/Vs. With the good reproducibility we concluded that C<sub>10</sub>-DNTT-based OFET devices show very high  $\mu_{\text{FETS}}$  close to 8 cm<sup>2</sup>/Vs, which are among the highest reported for organic thin-film-based transistors.<sup>153,154</sup>

**Summary.** I designed the shadow masks for patterning S-D electrodes and organic layers. The DNTT-based OTFTs fabricated with the new mask showed better performances reproducibly than those fabricated with the conventional mask. The OTFTs based on C<sub>10</sub>-DNTT were fabricated with the new mask, and the performances of the devices with  $\mu_{\text{FETS}}$  up to 8 cm<sup>2</sup>/Vs were definitely characterized, which is among the highest mobilities of thin-film-based OFETs. The present results indicate that the combination of a  $\pi$ -extended heteroacene core with long alkyl groups is promising approach to develop superior organic semiconductors.

### Experimental Procedures

**Fabrication of OTFT devices:** OTFTs were fabricated in a top-contact configuration on a heavily doped n<sup>+</sup>-Si (100) wafer with 200-nm-thick thermally grown SiO<sub>2</sub> ( $C_i = 17.3$  nF cm<sup>-2</sup>). The surface of the SiO<sub>2</sub> dielectrics was treated with silane-based self-assembled monolayer (SAM) reagents with following methods: the Si/SiO<sub>2</sub> substrate was washed in acetone and isopropanol with sonication for ca. 5 min and then exposed in UV/O<sub>3</sub> for 15 min. Subsequently the substrate was immersed in a toluene solution of 0.1 M octyltrichlorosilane (OTS) or octadecyltrichlorosilane (ODTS) at 60 °C for 20 min.<sup>155</sup> HMDS (hexamethyldisilazane)-treatment was carried out by exposing the substrate to HMDS vapor at room temperature in a box under nitrogen for 12 h. A thin film of DNTT or C<sub>10</sub>-DNTT (ca. 50 nm in thick, counted with a quartz oscillator) as the active layer was vacuum-deposited on the Si/SiO<sub>2</sub> substrates under a pressure of  $\sim 2 \times 10^{-3}$  Pa, substrate temperature ( $T_{\text{sub}}$ ) at 60 °C, and deposition rate ( $R_{\text{dep}}$ ) of 1.5 ~ 2.0 Å/s for DNTT and 0.1 Å/s for <sub>10</sub>-DNTT. On top of the organic thin film, gold (80 nm) was deposited through the shadow mask to give S-D electrodes. The characteristics of the OTFT devices were measured at room temperature in air with a Keithley 4200 semiconductor parameter analyzer. Field-effect mobility ( $\mu_{\text{FET}}$ ) was calculated in the saturation ( $V_d = -60$  V) or linear regime ( $V_d = -5$  V) of the  $I_d$  using the following equation,

Saturation regime:  $I_d = (WC_i / 2L)\mu_{\text{FET}} (V_g - V_{\text{th}})^2$

Linear regime:  $I_d = V_d (WC_i / L)\mu_{\text{FET}} (V_g - V_{\text{th}})$

where  $C_i$  is the capacitance, and  $V_g$  and  $V_{\text{th}}$  are the gate and threshold voltages, respectively.

Typical characteristics of DNTT-based OTFT devices with the conventional device structure is shown in Figure 3.2.8.

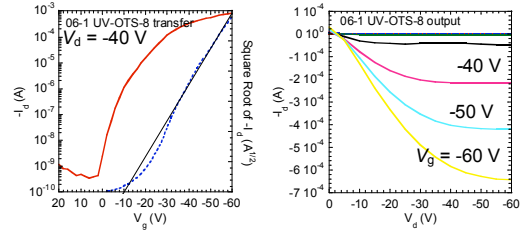


**Figure 3.2.8.** Transfer (a) and output (b) characteristic of a DNTT-based OTFT.

### 3.3 Fabrication of Polymer Dielectric films

#### Introduction.

The gate dielectric material plays a crucial part in the OFET operation, because charge-carriers move in a few layer close to the interface between the gate dielectric and the semiconductor.<sup>114-116</sup> In addition, the molecular arrangement in the first few layers are much influenced by the structure and surface energy of the dielectric.<sup>156,157</sup> The gate dielectric requires such characteristics as (i) high dielectric constant ( $k$ ) (= relative permittivity,  $\epsilon_r$ ) (ii) low leakage current, (iii) smooth surface, (iv) low surface energy, (v) absence of carrier-trap (vi) stability, and (vii) mechanical flexibility.<sup>158</sup> Over the past decade, a wide range of dielectric materials have been developed (Table 3.3.1 and 3.3.2).<sup>28,159</sup>

The commercially available Si/SiO<sub>2</sub> is the most reliable test bed for organic semiconductors as it was readily available from conventional Si technology. The SiO<sub>2</sub> has an excellent smooth surface (roughness < 0.1 nm), stability, low leakage current, and high- $k$ . The Si/SiO<sub>2</sub> gate-dielectric is, however, much differed from possible applications of OFETs because of its less flexibility.

Flexible dielectrics have been developed based on both inorganic and organic materials. The surface-modified alumina on aluminum (Al/AIO<sub>x</sub>) with self-assembled monolayers (SAM) is one of the superior inorganic flexible dielectric.<sup>48</sup> DNTT-based OTFT devices on the Al/AIO<sub>x</sub> showed 0.3 cm<sup>2</sup>/Vs with low-operating voltage according to Klauk *et al.*<sup>18</sup> The fabrication of the dielectrics, however, requires vacuum-process and special techniques similar to the other inorganic dielectrics.

On the other hand, organic dielectrics are expected as inexpensive and flexible gate-dielectrics because a variety of solution-processible polymer insulators have been demonstrated. In general, OTFT devices on the polymer dielectrics show higher  $\mu_{\text{FETS}}$  compared to those of inorganic ones.<sup>160</sup> Also, polymer dielectrics are compatible with general plastic substrates.

In this section, I examined several polymer dielectrics to OTFTs; Cytop, polyimide, and parylene N (Figure 3.3.1). The fabrication of the polymer dielectrics followed by evaluations of

**Table 3.3.1.** Classification of gate-dielectrics.

	material	general features
Gate dielectrics	Inorganic	High- $k$ (high polar)
	Organic (polymers)	Low- $k$ (non-polar)
	SAM	High- $k$ , low-voltage
	Ionic liquid	Very high- $k$ , liquid
	Multi-component	

**Table 3.3.2.** Dielectric constant ( $k$ ) of various gate insulators.

compound	$k$
Inorganic	
SiO <sub>2</sub>	3.9
Si <sub>3</sub> N <sub>4</sub>	7
Al <sub>2</sub> O <sub>3</sub>	9
ZrO <sub>2</sub>	23
HfO <sub>2</sub>	24
Ta <sub>2</sub> O <sub>5</sub>	25
TiO <sub>2</sub>	58
.....	
Organic	
polyvinylalcohol (PVA)	3.3
polyvinylphenol (PVP)	3.5
poly(methyl methacrylate) (PMMA)	3.5
polyimide	3.5
parylene N	3.1
parylene C	2.7
Cytop <sup>TM</sup>	2.1

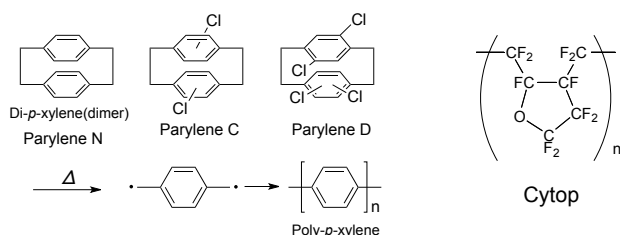


**Figure 3.3.1.** Structure of Parylenes and Cytop. The structure of the polyimide in this work is unknown.

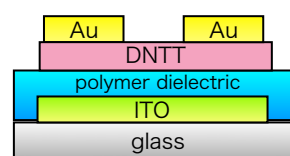


**Figure 3.3.2.** Device structure.

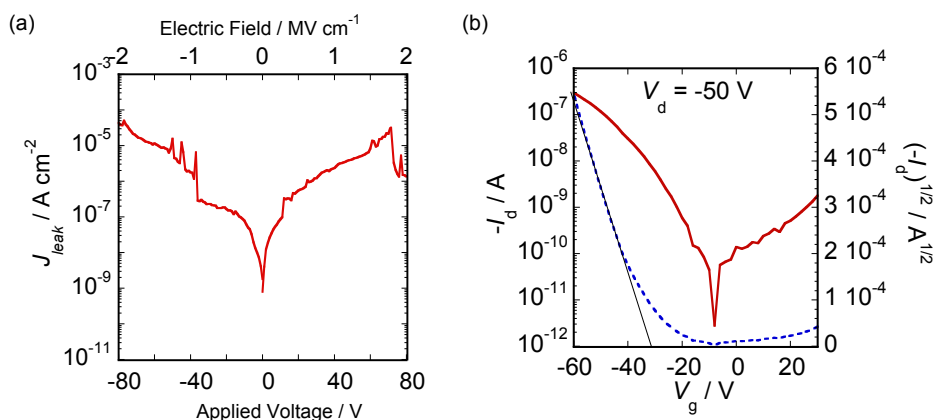


**Figure 3.3.3.** (a) Plot of leakage current density vs both applied voltage of Parylene N dielectric. (b) A FET characteristics of DNTT-based OTFT on parylene N dielectric.

the dielectrics by means of measuring the insulating characteristics, capacitance, and TFT characteristics of DNTT-based devices on the dielectrics are described (Figure 3.3.2).

**Parylene N.** Parylenes (di-*p*-xylenes) are commercially available coating precursors that has in three forms: parylene N, C, and D.<sup>161-163</sup> The monomer pyrolyzes in high temperature ( $\sim 650^\circ\text{C}$ ) and then polymerizes at room temperature, under  $\sim 10$  Pa to give a transparent film on a substrate, which has low air- and water-permeability. Parylenes have frequently been used as dielectrics in top- or bottom-gate transistors or as protecting layer in devices.<sup>164,165</sup>

I built up an apparatus, and ca. 400 nm in thick of transparent parylene films on indium-tin oxides (ITO) glass substrates were fabricated. The parylene films showed  $C_i$  of  $\sim 10$  nF/cm<sup>2</sup> ( $k \sim 4.7$ ). The DNTT-based OTFTs with the parylene films, however, showed poor characteristics owing to the large gate-leakage current density ( $J_{\text{leak}}$ ) over  $10^{-7}$  A/cm<sup>2</sup> at  $-40$  V (Figure 3.3.3a). One device showed an appreciable characteristic with  $\mu_{\text{FET}}$  of  $2 \times 10^{-3}$  cm<sup>2</sup>/Vs and  $I_{\text{on}}/I_{\text{off}}$  of  $\sim 10^3$  (Figure 3.3.3b). The low performances are responsible for low quality of the parylene films. Fabrication procedure should be improved.

### 3. Evaluation of C<sub>10</sub>-DNTT

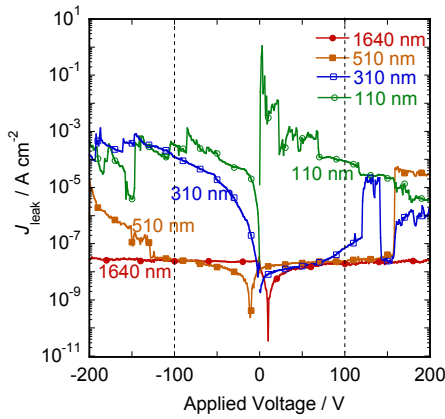


**Figure 3.3.4.** Leakage current of Cytop films with different thickness.

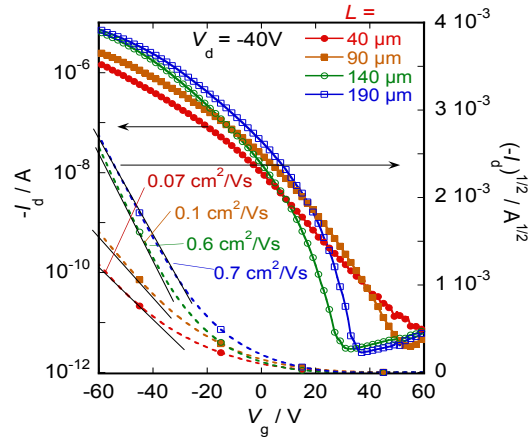


**Figure 3.3.5.** Transfer characteristics of DNTT-based OTFTs on Cytop films of 1460 nm in thickness.

**Table 3.3.3.** OFET characteristics of DNTT<sup>a</sup> on Cytop films fabricated on ITO glass substrate.

conc. <sup>b</sup>	d / nm	L <sup>c</sup> / μm	V <sub>th</sub> / V	μ <sub>FET</sub> / cm <sup>2</sup> V <sup>-1</sup> s <sup>-1</sup>	I <sub>on</sub> /I <sub>off</sub>
9	1460	40	-25	0.05 - 0.07	10 <sup>5</sup>
		90	-19	0.12 - 0.13	10 <sup>6</sup>
		140	-20	0.59	10 <sup>6</sup>
		190	-8	0.09 - 0.69	10 <sup>6</sup>
6	510	40	-30	0.004 - 0.02	10 <sup>6</sup>
		90	-20	0.67 - 0.82	10 <sup>6</sup>
		140	-29	0.82 - 0.83	10 <sup>8</sup>
		190	-24	0.85 - 0.91	10 <sup>7</sup>
5	310	140	-16	0.06	10 <sup>5</sup>
3	110		no field-effect response		

<sup>a</sup> DNTT layer was deposited at  $T_{sub} = 60$  °C,  $R_{dep} = 1.0$  Å/s, thickness ca. 500 Å.

<sup>b</sup> Dissolved in fluoro CTL-180v. <sup>c</sup>  $W = 1500$  μm.

**Cytop.** Cytop™ is the fluoropolymer developed by Asahi Glass Chemical. Since Cytop provides highly hydrophobic surface (low surface energy), transparent, and low- $k$  dielectric film, several researchers have reported high performance OTFTs on Cytop films.<sup>166-174</sup> The OTFTs on Cytop include DNTT-based bottom-gate devices that showed μ<sub>FET</sub>s up to 0.2 cm<sup>2</sup>/Vs.<sup>175</sup>

Cytop films were fabricated by spin-coating followed by annealing process (see Experimental Procedures). Various thickness of Cytop films were prepared by changing concentration (9 % - 3 %). All films showed typical dielectric constant of  $k = \sim 2.0$  nF/cm<sup>2</sup>. The Cytop dielectrics with relatively larger thickness (1460 and 510 nm) showed good insulating properties with  $J_{leak} < 10^{-7}$  A/cm<sup>2</sup> at 100 V, although thinner ones (310 and 110 nm) showed poor characteristics with large  $J_{leak}$ s up to 10<sup>-3</sup> A/cm<sup>2</sup> at  $V_g < 100$  V (Figure 3.3.4).

The OTFTs were fabricated by deposition of DNTT on the Cytop layer followed by deposition of gold S-D electrodes. The OTFTs on 1460 nm- thick of Cytop dielectrics showed good μ<sub>FET</sub>s up to 0.7 cm<sup>2</sup>/Vs and  $I_{on}/I_{off} \sim 10^6$  (Table 3.3.3). The OTFT devices on the 510 nm of Cytop/ITO-glass also showed good performances with μ<sub>FET</sub>s  $\sim 0.9$  cm<sup>2</sup>/Vs. The characteristics on the Cytop dielectrics, however, have positively higher turn-on voltage ( $> +30$  V) and large sub-threshold swing ( $> 10$  V/dec) than those on the Si/SiO<sub>2</sub> (Figure 3.3.5). The OTFTs on the thinner Cytop films (310 nm and 110 nm) showed large  $I_d$  in the subthreshold regions. The devices on 110 nm of Cytop were no field-effect response at all. This is attributable to low quality (many pin-holes, etc) of the Cytop films. Realizing TFTs characteristics on polymer dielectrics as good as those on the SiO<sub>2</sub> dielectric is more difficult than expected.

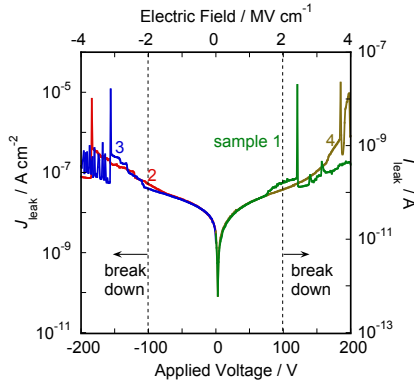


**Figure 3.3.6.** Plot of leakage current density (leakage current) vs applied voltage (electric field) of 500 nm in thickness of the polyimide film.

**Table 3.3.4.** Characteristics of DNNT-based OTFTs on polyimide dielectrics.<sup>a</sup>

$d / \text{nm}$	$L^b / \mu\text{m}$	$V_{\text{th}} / \text{V}$	$\mu_{\text{FET}} / \text{cm}^2\text{V}^{-1}\text{s}^{-1}$	$I_{\text{on}}/I_{\text{off}}$
870 - 880	40	-2 - +17	0.40 - 0.53	$10^7$
	90	+7 - +18	0.44 - 0.56	$10^7$
	140	+4 - +18	0.38 - 0.67	$10^7$
	190	0 - +22	0.27 - 0.63	$10^7$
490 - 500	40	0 - +6	0.45 - 0.55	$10^8$
	90	+5 - +10	0.41 - 0.50	$10^7$
	140	+9 - +11	0.43 - 0.44	$10^7$
	190	+3 - +12	0.08 - 0.50	$10^7$
405 - 410	40	+2 - +6	0.38 - 0.52	$10^7$
	90	+3 - +5	0.30 - 0.55	$10^7$
	140	+4 - +8	0.24 - 0.53	$10^8$
	190	+4 - +8	0.45 - 0.50	$10^7$

<sup>a</sup> top-contact configuration. DNNT was deposited with  $T_{\text{sub}} = 60$  °C and  $R_{\text{dep}} = \text{ca. } 1.0 \text{ \AA/s}$ . <sup>b</sup>  $W = 1500 \mu\text{m}$ ,

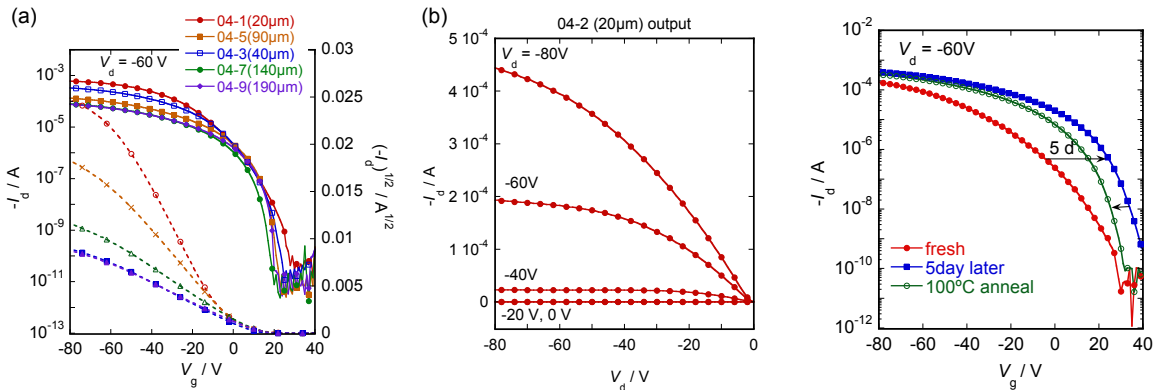


**Figure 3.3.7.** Transfer (a) and output characteristics (b) of DNNT-based TFT on the polyimide dielectric. The extracted  $\mu_{\text{FETS}}$  in saturate region are  $0.67 \text{ cm}^2/\text{Vs}$ ,  $0.55 \text{ cm}^2/\text{Vs}$ ,  $0.43 \text{ cm}^2/\text{Vs}$ ,  $0.40 \text{ cm}^2/\text{Vs}$ , and  $0.49 \text{ cm}^2/\text{Vs}$  in devices with  $L$  of  $20 \mu\text{m}$ ,  $40 \mu\text{m}$ ,  $90 \mu\text{m}$ ,  $140 \mu\text{m}$  and  $190 \mu\text{m}$ , respectively.

**Figure 3.3.8.** Transfer characteristics of DNNT devices on the polyimide being stored for 5 days, followed by annealing in  $\text{N}_2$  atmosphere at  $100^\circ\text{C}$ .

**Polyimide.** Polyimide is one of the popular insulating materials widely used in electronics, because of their high chemical resistance and mechanical properties.<sup>176-179</sup> Although high curing temperature ( $\sim 300^\circ\text{C}$ ) prevented application to TFTs for the decades, recent progress in polymer technology makes it possible to commercialize a class of polyimide precursors, which can be cross-linked at temperature as low as  $180^\circ\text{C}$ . Someya *et al* have reported high performance pentacene-based OTFTs on polyimide gate-dielectrics with mobilities up to  $1 \text{ cm}^2/\text{Vs}$ .<sup>180</sup> The OTFTs are integrated into complex electronics devices.<sup>165</sup>

Polyimide films were fabricated on ITO-glass substrates by spin-coating polyimide precursor followed by annealing procedure  $\sim 180^\circ\text{C}$ . Thickness of the polyimide films are measured to be  $880 \text{ nm}$  to  $410 \text{ nm}$  depending on the spin rates (see Experimental Procedures, Table 3.3.11), all of which showed typical  $k$  (ca. 3.1) and high insulating properties with  $J_{\text{leak}} < 10^{-7} \text{ A/cm}^2$  at  $V_g < 100 \text{ V}$  (Figure 3.3.6).

Independent of the channel length ( $L$ ) and dielectric thickness, DNNT-based OTFTs on the polyimide dielectrics showed high performances with  $\mu_{\text{FETS}}$  of ca.  $0.5 \text{ cm}^2/\text{Vs}$ ,  $I_{\text{on}}/I_{\text{off}}$  of  $\sim 10^7$  (Table 3.3.4, Figure 3.3.7). Large turn-on voltage ( $V_{\text{on}}$ ) up to  $+30 \text{ V}$  were observed in all characteristics, which were shifted positively after allowing the device to stand in ambient air (Figure 3.3.8). The shift was recovered by annealing the device in  $\text{N}_2$  atmosphere at  $\sim 100^\circ\text{C}$ . The resulting transfer characteristics of annealed devices were better than those of fresh devices. The  $V_{\text{on}}$  shift can be explained by absorption of impurities such as  $\text{H}_2\text{O}$  and  $\text{O}_2$ .<sup>160</sup>

### 3. Evaluation of C<sub>10</sub>-DNTT

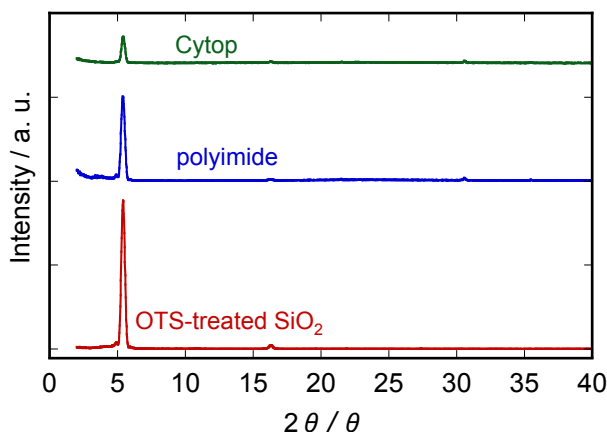


**Figure 3.3.9.** XRD patterns of thin films of DNTT on Cytop, polyimide, and OTS-treated Si/SiO<sub>2</sub>. *d*-Spacings calculated from first peak are 16.3 Å.

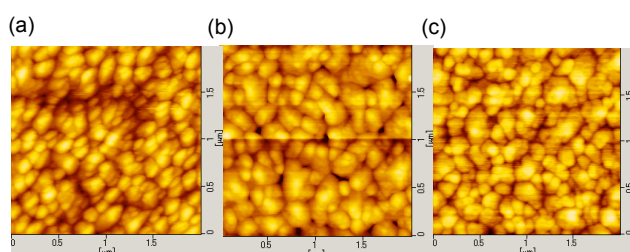


**Figure 3.3.10.** AFM images of thin films of DNTT on (a) Cytop (b) OTS-treated SiO<sub>2</sub> (c) polyimide.

**Thin-film structures.** The surface morphologies and the crystallinity were investigated by X-ray diffraction (XRD) and atomic force microscopy (AFM), respectively. The XRD patterns of DNTT films showed the same sharp reflections which assignable to crystallographic (001) diffractions on ITO/Cytop, ITO/polyimide, and OTS-treated Si/SiO<sub>2</sub> (Figure 3.3.9). The intensities of peaks are, however, in the order of OTS > polyimide > Cytop, indicating crystallinity of the thin films are slightly different with this order. On the other hand, the AFM images showed that ca. 100 nm size crystalline grains grew on the surfaces on all dielectrics (Figure 3.3.10). These structures indicates the difference of the characteristics of devices depending on the dielectrics may be attributed the the difference of the crystallinity of the films and subtle structural difference of dielectric and organic layer near the interface.

**Summary.** Three kind of polymer dielectrics, Parylene N, Cytop and polyimide, were fabricated on the ITO-glass substrates and evaluated their properties including TFT characteristics of DNTT-based devices on the dielectrics. Fundamental techniques of fabrication/evaluation of polymer dielectrics were established.

Parylene N showed poor performances as the gate-dielectric and consequently poor TFT characteristics. In contrast, Cytop and polyimide showed good dielectric properties and TFT characteristics with high  $\mu_{\text{FETS}}$  of up to 0.9 cm<sup>2</sup>/Vs and 0.5 cm<sup>2</sup>/Vs, respectively. The Cytop-based OTFTs showed higher  $\mu_{\text{FETS}}$  and air-stability, however, which also showed low-reproducibility and large subthreshold swing, especially short channel devices. On the other hand, the polyimide-based OTFT showed steady  $\mu_{\text{FET}}$  and  $I_{\text{on}}/I_{\text{off}}$  values regardless of the thickness of dielectric films or  $L$  of the devices. I thus decided to use polyimide as a dielectric material for fabrication of flexible C<sub>10</sub>-DNTT devices on plastic substrates in section 3.4, although relatively

high curing temperature ( $\sim 180^\circ\text{C}$ ) of polyimide could be a potential problem in the application to a flexible substrate.

## Experimental Procedures

### Fabrication of dielectric films:

**Parylene N:** The parylene N was placed on a quartz glass tube, and reduced pressure under  $\sim 5$  Pa. The tube near the sample was heated slowly from  $80^\circ\text{C}$  to  $170^\circ\text{C}$  over ca. 1h while the tube far from the sample was heated to  $660^\circ\text{C}$ .

**Cytop:** Glass plates coated with indium-tin oxides (ITO-glass) were used for substrates. The ITO were patterned as gate-electrodes (see Section 3.4). The Cytop dielectrics were simply fabricated on the ITO-glass substrates by spin-coating of Cytop as purchased (CTL-809M, 9%) or diluted with the attached fluorocarbon-based solvent for spin-coating (CTL-180v). Cytop films are also fabricated on Si/SiO<sub>2</sub> substrates for comparison. The spin-coated Cytop were cured at  $50^\circ\text{C}$  for 1 h,  $80^\circ\text{C}$  1h, and  $120^\circ\text{C}$  2 h in nitrogen atmosphere.

The Cytop films with some different thicknesses from 1460 nm to 110 nm were obtained from different concentration of Cytop solvent from 9 % to 3 % (Table 3.3.10)

**Table 3.3.10** Properties of Cytop dielectrics

conc.	spin rate	$d$ / nm	$C_i$ / nF cm <sup>-2</sup>	$k$
9%		1460	1.3	2.1
6%	500 rpm 10s	510	3.4	2.0
4.5%	1000 rpm 30 s	310	5.5	1.9
3%		110	14.6	1.8

**Polyimide.** The polyimide precursor (KEMI-TITE CT4112, Kyocera Chemical) was spin-coated onto the gate-patterned ITO-glass substrates with various spin rate: 1000 rpm (2 s) then 2000 rpm (58 s), 2000 rpm (2 s) then 4000 rpm (58 s), and 3000 rpm (2 s) then 6000 rpm (58 s) (Figure 3.3.11). The substrates were cured at  $80^\circ\text{C}$  for 1 h,  $120^\circ\text{C}$  1h, and  $180^\circ\text{C}$  1h under nitrogen atmosphere to give the transparent polyimide films.

**Table 3.3.11** Properties of Polyimide Dielectrics

spin rate	$d$ / nm	$C_i$ / nF cm <sup>-2</sup>	$k$
2000 rpm	870 - 880	2.9 - 3.2	2.8 - 3.2
4000 rpm	490 - 500	5.4 - 5.6	3.0 - 3.1
6000 rpm	405 - 410	3.1	3.1

**Fabrication of OTFT devices.** DNTT was deposited for 50 nm onto the dielectrics under the conditions of  $T_{\text{sub}} = 60^\circ\text{C}$  and  $R_{\text{dep}} = \sim 2.0 \text{ \AA/s}$ . Au S-D electrodes were deposited with  $R_{\text{dep}} = \sim 2.0 \text{ \AA/s}$  through the shadow mask to give top-contact OTFT devices and MIM devices for measurement of characteristics dielectrics.

**Dielectric characteristics.** A film capacitance ( $C_i$ ) was measured on a ITO-dielectric-Au structure which fabricated together with OTFT devices by using a Keithley 4200-SCS Semiconductor analyzer. Standard measurement condition are DC bias 0 V, presoak 0 V, frequency 10 kHz, AC voltage 30 mV RMS, sampling interval 0.5 s, sampling number 10 in voltage bias mode. The frequency ( $f$ ) should approximately be equal to the sweep speed ( $S$ ) of gate-voltage ( $V_g$ ) of the transfer characteristics measurement. e.g., if  $V_g$  is swept from 40 V to -80 V in 2 sec,  $S$  would be 60 V/s. The 60 V/s corresponds to  $f = 1$  kHz when AC = 30 mV RMS. Hint is  $(60 \text{ [V/s]}) = (15 \text{ m[V]}) / ((1 / 4f)[\text{s}])$ . Average of measured value ( $C_{\text{DUT}}$ ) is divided by the area of electrode ( $2.90 (\pm 0.04) \times 10^{-3} \text{ cm}^2$ ) to give  $C_i$ . The dielectric constant is estimated by  $k = (C_i \cdot d) / \epsilon_0$ , where  $\epsilon_0 = \text{permittivity of vacuum} (= 8.85 \times 10^{-14} \text{ F/cm})$ ,  $d = \text{film thickness (cm)}$ .

$C_i$  of SiO<sub>2</sub> (200 nm) were measured first for certification of the system. The resulting  $C_i = 16.1 \text{ nF/cm}^2$  is most likely as a value of SiO<sub>2</sub>, although the value is different with  $17.3 \text{ nF/cm}^2$  that usually I employed.

**Measurement of Insulating Properties.** The measurement was carried out by connection of one side of a MIM device with the probe that usually used as gate, and another side of the MIM device with the probe that used as source (ground). Electric field ( $E$ ) in leakage characteristics is calculated by

$$E = \frac{V_g}{d}$$

where  $V_g$  is the applied voltage [V],  $d$  is film thickness [cm].

Current density ( $J$ ) is calculated by

### 3. Evaluation of C<sub>10</sub>-DNTT

$$J = \frac{I_g}{S}$$

where  $I_g$  is the gate current [V],  $S$  is area of electrode,  $2.90 \times 10^{-3}$  [cm<sup>2</sup>].

**Thickness Measurement.** Thickness of film ( $d$ ) are measured with an AMBOS Stylus profilometer. The general measurement conditions are speed 0.20 mm/sec, range 100 microns, stylus force 0.5 mg.

**Atomic Force Microscopy (AFM).** The AFM images were measured on a SII nanocute with cyclic-contact dynamic force mode (DFM).

**X-ray diffraction (XRD).** Thin-film XRD were measured on a Rigaku Ultima VI X-ray diffractometer with Cu K $\alpha$  source ( $\lambda = 1.541$  Å) in air. The  $d$ -spacings were calculated by the Bragg equation:  $\lambda = 2d\sin\theta$ .

### 3.4 Evaluation on Plastic Substrates

**Introduction.** The technology of the organic thin film transistors (OTFTs) has been attracted much attention, because of their potential applications as a key device for the future plastic electronics.<sup>3,8</sup> One of the important features of OTFTs that can differentiate from ordinary silicon- or metal oxide-based TFTs is lower processing temperature (<200 °C) than those for the inorganic-based TFTs (several hundreds degree), which allows OTFT to be fabricated on plastic films. In fact, fabrication of OTFTs on the plastic substrates has been investigated actively, and their applications to various devices including the drivers for flexible displays,<sup>164,10b</sup> bendable sensors,<sup>165,181</sup> sheet-like scanners, rewritable braille sheets,<sup>179,182</sup> and so on, have been demonstrated.

Most of these plastic OTFTs have employed pentacene (Figure 3.4.1),<sup>145-147,180</sup> the standard vapor-processible organic semiconductor, as the active material that enables good performance with mobility as high as  $\sim 3 \text{ cm}^2/\text{Vs}$ .<sup>48,8</sup> However, the lack of air-stability and durability of pentacene itself is an apparent drawback for actual plastic electronics applications.<sup>183</sup> On the other hand, dinaphto[2,3-*b*:2'3'-*f*]thieno[3,2-*b*]thiophene (DNNT), developed as an air-stable and high performance organic semiconductor with mobility of up to  $3.0 \text{ cm}^2/\text{Vs}$ , is an attractive alternative,<sup>17</sup> and recently flexible, low-voltage OTFTs and circuits based on DNNT as the active semiconducting material have been realized.<sup>18</sup> In addition, very recently further material improvement in terms of the mobility has been achieved based on the DNNT structure: alkylation of DNNT core turned out to be quite effective to enhance mobility,<sup>124,125</sup> and optimized di(*n*-dodecyl)-DNNT (C<sub>10</sub>-DNNT, Figure 3.4.1)-based devices on Si/SiO<sub>2</sub> substrates reaches up to  $8 \text{ cm}^2/\text{Vs}$ .<sup>22</sup>

In the final section of this chapter, I describe C<sub>10</sub>-DNNT-based TFTs fabricated on the polyimide gate dielectrics coated over polycarbonate (PC) substrates along with the parent DNNT-based TFTs on the same substrate for comparison (Figure 3.4.2). The C<sub>10</sub>-DNNT-based devices showed excellent performances with mobility as high as  $2.4 \text{ cm}^2/\text{Vs}$  and  $I_{\text{on}}/I_{\text{off}}$  grater than  $10^7$  under ambient conditions.

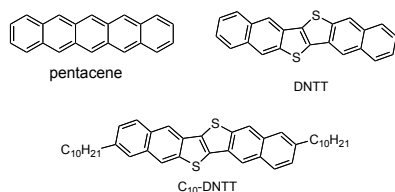


**Figure 3.4.1.** Chemical structure of organic semiconductors.

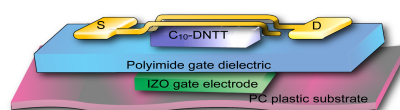


**Figure 3.4.2.** Schematic device structure of TFTs fabricated on PC substrates.

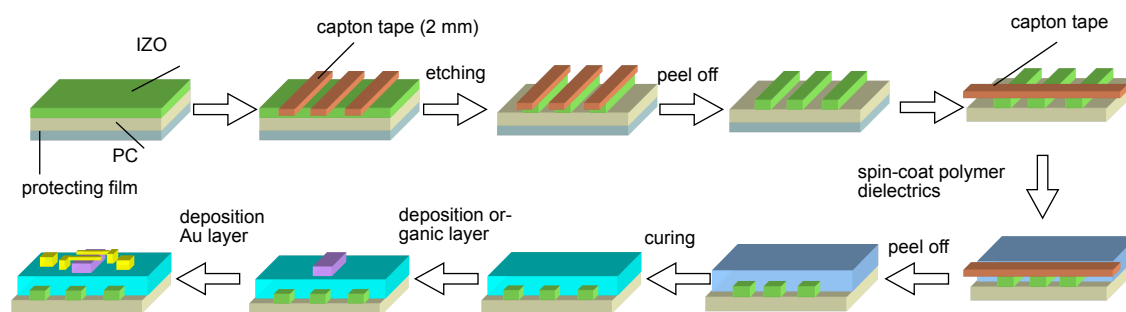


**Figure 3.4.3.** Device fabrication process.

### 3. Evaluation of C<sub>10</sub>-DNTT

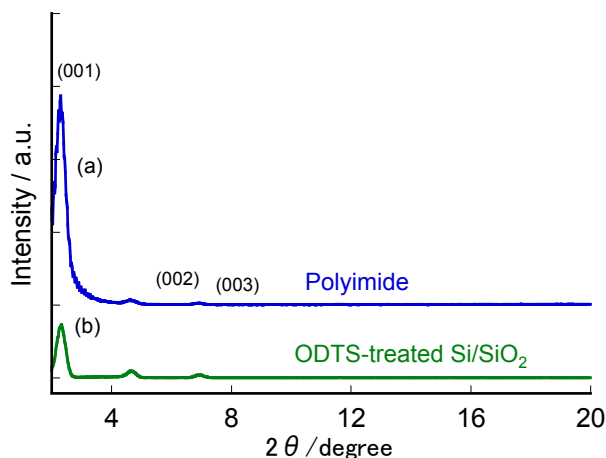


**Figure 3.4.4.** XRD patterns of C<sub>10</sub>-DNTT thin films: (a) on a PC/polyimide substrate and (b) a Si/SiO<sub>2</sub> substrates. The calculated *d*-spacing = 3.8 nm.

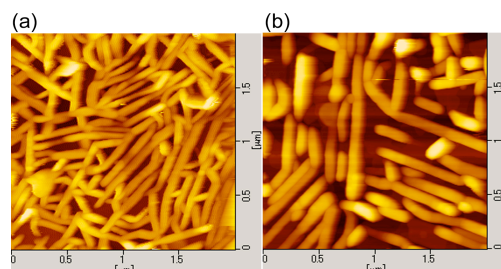


**Figure 3.4.5.** AFM images of C<sub>10</sub>-DNTT thin films: (a) on a PC/polyimide substrate and (b) a Si/SiO<sub>2</sub> substrates.

**Methodology.** A PC film coated with indium-zinc oxide (IZO) layer was cut into pieces of 2 × 2 cm squares (Figure 3.4.3).<sup>184</sup> The IZO layer was patterned for gate electrodes by etching process: the substrates that protected by capton tape were immersed in diluted aqua regia (HCl : H<sub>2</sub>O : HNO<sub>3</sub> = 1 : 4 : 0.08) for ~10 sec. After removal of the capton tape, the substrates were washed with water, acetone, and isopropanol. Polyimide precursor (KEMI-TITE CT4112, Kyocera Chemical)<sup>180</sup> was spin-coated on PC plastic substrates, edge of which had been protected by capton tape for gate-contact for measurement. The spin rate was 1000 rpm for 10 s and 4000 rpm for 30 s. The spin-coated substrates were immediately placed on a hot plate for ~10 min at ~80 °C. The substrate was then annealed at 180 °C for 1 h under nitrogen atmosphere, giving the transparent polyimide film (ca. 600 nm thickness).

C<sub>10</sub>-DNTT and DNTT were synthesized according to the reported procedures and purified by vacuum gradient-sublimation.<sup>17,22</sup> Vacuum deposition of the materials (60 nm thickness) on the substrate with 60 °C of substrate temperature (*T*<sub>sub</sub>) and 0.1 Å/s of deposition rate (*R*<sub>dep</sub>) gave a uniform semiconducting layer. On top of it, vapor deposition of gold (80 nm thickness) through a shadow mask defined the source and drain electrodes, giving OTFT devices with a top-contact, bottom-gate configuration having a constant channel width (*W*) of 1500 μm and various channel lengths (*L*) of 40 ~ 190 μm. The TFT characteristics are evaluated with a Keithley 4200-SCS semiconductor characterization system. Mobility was calculated from the transfer curves in the saturate regime by using the following equation:

$$\mu_{\text{FET}} = (2 \cdot I_d \cdot L) / [W \cdot C_i \cdot (V_g - V_{\text{th}})^2]$$

where  $\mu$  is mobility,  $I_d$  is source-drain current,  $C_i$  is capacitance of dielectric, and  $V_g$  is gate-source voltage. The thickness (*d*) and capacitance ( $C_i$ ) of the dielectrics for each device were measured with an AMBIOS Stylus Profilometer and Keithley 4200-CVU, respectively. Experimentally decided  $C_i$  values showed good agreement with the value estimated from the thickness of the polyimide layer and reported  $\epsilon_r$  value.

The atomic force microscopy (AFM) images were measured on a SII nanocute with cyclic-contact dynamic force mode (DFM). Thin-film X-ray diffraction (XRD) were measured on a Rigaku Ultima VI X-ray diffractometer with Cu K $\alpha$  source ( $\lambda = 1.541 \text{ \AA}$ ) in air.

**Thin film morphology.** Crystallinity and surface morphology of the C<sub>10</sub>-DNTT layer deposited on the polyimide gate dielectric were investigated with X-ray diffraction (XRD) and atomic force microscopy (AFM), respectively. The XRD patterns (Figure 3.4.4) clearly testify that a crystalline C<sub>10</sub>-DNTT thin film formed on the polyimide gate dielectric and the molecular

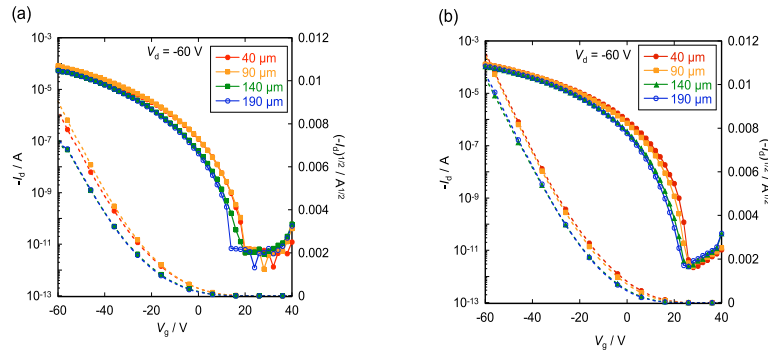


**Figure 3.4.6.** Transfer characteristics of C<sub>10</sub>-DNTT-TFTs: (a) fresh devices and (b) annealed devices at 100 °C.

arrangement is basically the same with that on the Si/SiO<sub>2</sub> substrate. Although the first XRD peak, i.e., the 001 reflection is clearly observed on the polyimide layer, higher reflections are quite broad and weak (Figure 3.4.4a), whereas the thin film on the Si/SiO<sub>2</sub> substrate shows clear peaks up to 003 reflections (Figure 3.4.4b). This indicates that the crystallinity of the thin film on the polyimide layer is lower than that on the Si/SiO<sub>2</sub> substrate, which is presumably caused by the larger roughness of the former than the latter.

AFM images show that wire-like crystalline grains grew on the polyimide layer, whereas relatively larger domains with rod-like crystals are observed for the thin film on the Si/SiO<sub>2</sub> (Figure 3.4.5). This morphological difference can be again ascribed to the surface roughness of the substrates. Rather flat and smooth surface of Si/SiO<sub>2</sub> can induce the formation of larger domains, whereas the polyimide surface with large roughness can facilitate rapid nucleation, resulting in different surface morphologies.

**TFT characteristics.** The C<sub>10</sub>-DNTT-based TFTs on the polyimide gate dielectrics showed decent p-channel FET responses under ambient conditions (Figure 3.4.6). Mobilities extracted from the saturation regime at the drain ( $V_d$ ) and gate voltage ( $V_g$ ) of  $-60$  V were higher than  $0.5$  cm<sup>2</sup>/Vs, regardless of the channel lengths ( $L$ ) (Table 1). Noticeable channel length ( $L$ ) dependence of the mobility was observed, as was the case for the devices on the Si/SiO<sub>2</sub> substrates, and the devices with longer  $L$  tend to give higher mobility. The highest mobility among the fresh devices on the polyimide gate is  $\sim 1.5$  cm<sup>2</sup>/Vs at  $L = 190$  μm, which is about one fifth of the best device fabricated on the Si/SiO<sub>2</sub> substrate ( $7.9$  cm<sup>2</sup>/Vs). It is highly likely that the reduced mobility of the devices on the polyimide gate is ascribed to the reduced crystallinity of the thin film as described above, which may cause higher channel resistance owing to the increase the grain boundary, in other words, the large numbers of carrier traps in the channel region. Similar reduction of the mobility caused by changing the substrate and gate dielectric from the Si/SiO<sub>2</sub> to PC/polyimide was also observed for the unsubstituted DNTT-based TFTs: the mobility as high as  $3.1$  cm<sup>2</sup>/Vs on the Si/SiO<sub>2</sub>, whereas  $0.5$  cm<sup>2</sup>/Vs on the present PC/polyimide substrate. It is thus rational to consider that the surface roughness of the gate dielectric causing the limited crystallinity of the semiconducting layer is one of the major reasons for reducing the mobility. On the other hand, even on such less ideal substrate surface, the present C<sub>10</sub>-DNTT-TFTs showed quite high mobility, clearly indicating the good potential of C<sub>10</sub>-DNTT molecule as an organic semiconductor. It should be also noted that pentacene TFTs fabricated on the identical PC/polyimide substrate showed mobilities up to  $0.24$  cm<sup>2</sup>/Vs, which is one order of magnitude lower than those of the C<sub>10</sub>-DNTT-TFTs.

Another noticeable differences of the TFT characteristics of the present devices compared with those on the Si/SiO<sub>2</sub> substrate are positive turn-on voltage ( $\sim +20$  V) and sluggish increase of  $I_d$  in the subthreshold region. Although the actual reasons for these non ideal behaviors are

### 3. Evaluation of C<sub>10</sub>-DNNT

not clear, it is generally believed that they are attributed to the residual dopant and carrier traps, respectively, in the interface between the semiconducting layer and the dielectric layer. Since such non-ideal characteristics are often improved by thermal annealing after the device fabrication,<sup>176</sup> we tested a thermal treatment (~100 °C) of the devices under nitrogen. Figure 3.4.5 shows the transfer characteristics of the annealed devices; although no significant improvements of the  $I_d$  increase in the subthreshold region was observed, increase of mobility and reduction of off-current were observed.

I also checked the stability of the present C<sub>10</sub>-DNNT-TFTs. Different from the pentacene-based OTFTs, the C<sub>10</sub>-DNNT-TFTs showed good stability during storage under ambient lab conditions: no apparent reduction was observed in the mobility and  $I_{on}/I_{off}$  ratio after 30 days without any encapsulations, although slight  $V_{th}$  shift was observed.

**Summary.** In summary, I have successfully fabricated C<sub>10</sub>-DNNT-TFTs on the PC/polyimide plastic substrate. The devices showed good p-channel characteristics with the mobility over 2.4 cm<sup>2</sup>/Vs and  $I_{on/off}$  of 10<sup>7</sup> under ambient conditions. Although the present mobility is somewhat reduced compared to those of the C<sub>10</sub>-DNNT-TFTs on the Si/SiO<sub>2</sub> substrates, which may be caused by reduced crystallinity of the semiconducting layer on the polyimide gate dielectric as confirmed by the AFM and XRD measurements, the mobility itself is quite high for so far reported OTFTs fabricated on the plastic substrate. Further process optimizations as well as applications of C<sub>10</sub>-DNNT to other flexible substrate/gate dielectrics are now underway in our group.

### 3.5. Conclusion for Chapter 3

I successfully evaluated C<sub>10</sub>-DNTT as a high performance semiconductor showing mobilities ( $\mu_{\text{FETS}}$ ) up to 8 cm<sup>2</sup>/Vs on Si/SiO<sub>2</sub> substrates and 2.4 cm<sup>2</sup>/Vs on PC/polyimide substrates (Figure 3.5.1).

The high  $\mu_{\text{FETS}}$  were obtained reproducibly with the newly designed device configuration. Channel length ( $L$ ) dependence was observed in the TFT characteristics of the C<sub>10</sub>-DNTT-based devices, which indicates contact resistance

limits the  $\mu_{\text{FET}}$  significantly in the short  $L$  devices. In contrast, DNTT showed almost no  $L$  dependence, in spite of almost the same HOMO energy level of DNTT as that of C<sub>10</sub>-DNTT. The structural difference in the solid state may affect the charge-injection characteristics.

The DNTT and C<sub>10</sub>-DNTT-based OTFT devices on the PC/polyimide substrates gave the  $\mu_{\text{FETS}}$  up to 0.6 cm<sup>2</sup>/Vs and 2.4 cm<sup>2</sup>/Vs, respectively. Apparently higher  $\mu_{\text{FETS}}$  of C<sub>10</sub>-DNTT-based devices than those of DNTT-based devices indicate the important role of the long alkyl chains for achieving high  $\mu_{\text{FETS}}$ , which enhances 2-D electronic interaction between the  $\pi$ -cores even on the polymer dielectrics. Formation of the crystalline films was elucidated by the XRDs. However, the slightly increasing disorder in the films of DNTT and C<sub>10</sub>-DNTT on the polyimide can be attributed to the lower  $\mu_{\text{FETS}}$  as compared to those on the SiO<sub>2</sub> dielectric.

The present performances and air-stability of the OTFTs based on C<sub>10</sub>-DNTT on bare Si/SiO<sub>2</sub> and PC/polyimide substrates is comparable or superior to those of pentacene. However, the contact resistance limiting TFT characteristics and the low solubility limiting fabrication process should be improved.<sup>185</sup> Further active development of organic semiconductors will be expected.

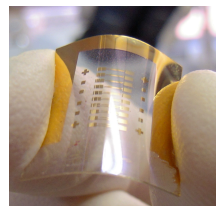


**Figure 3.5.1.** Picture of the C<sub>10</sub>-DNTT-based OTFT on the plastic substrate.

## **Closing Remarks**

I have developed small  $\pi$ -conjugated molecules with long alkyl chains for thin-film-based OFETs, in terms of the molecular design, synthesis, FET characteristics, structural analysis, theoretical analysis, and application to flexible devices. I believe this interdisciplinary studies contribute to development of organic semiconductors. The FET characteristics were well-correlated with the electronic structures in the layer-by-layer structures, which may give new ideas for designing organic semiconductors. The success of this study is come from the study of TTF derivatives that gave the good molecular concept followed by application of the concept to the high performance DNTT  $\pi$ -cores. The result could not be achieved only by myself. The collaboration should be essential for the development of materials and devices.

## References

- (1) 秋田純一, ゼロから学ぶ電子回路, 講談社, 2002.
- (2) 大西一功, 藤田実, 絵ときでわかる半導体デバイス, オーム社, 2002年 [livepage.apple.co.jp](http://livepage.apple.co.jp)
- (3) Klauk, H. *Organic Electronics: Materials, Manufacturing, and Applications*; Wiley-VCH, 2006.
- (4) Nokia Coporate; [http://www.nokia.com/press/media\\_resources/photos/corporate/showphotos?category=rd](http://www.nokia.com/press/media_resources/photos/corporate/showphotos?category=rd)
- (5) *NIKKEI MICRODEVICES*, July 2009 vol. 288; NikkeiBP.
- (6) 鶴飼育弘, 薄膜トランジスタ技術のすべて—構造、特性、製造プロセスから次世代TFTまで, 工業調査会, 2007.
- (7) *Semiconductor FPD World*, **2010**, *29*, 31-37.
- (8) Kagan, C. R.; Andry, P. *Thin-Film Transistors*; CRC Press, 2003.
- (9) “*Extreme bending OTFT*” Sekitani, T.; Zschieschang, U.; Klauk, H.; Someya, T. *Nat. Mater.* **2010**, *9*, 1015-1022.
- (10) (a) Sony Co Ltd; [http://www.sony.co.jp/SonyInfo/technology/technology/theme/organictransistor\\_01.html](http://www.sony.co.jp/SonyInfo/technology/technology/theme/organictransistor_01.html). (b) Gelinck, G.; Heremans, P.; Nomoto, K.; Anthopoulos, T. D. *Adv. Mater.* **2010**, *22*, 3778-3798.
- (11) (a) Roberts, M. E.; Sokolov, A. N.; Bao, Z. *J. Mater. Chem.* **2009**, *19*, 3351-3363. (b) *Semiconductor FPD World* **2009**, *28*, 37-51.
- (12) *Nikkei Electronics* **2009**, 12-28, 73-82.
- (13) Murphy, A. R.; Fréchet, J. M. J. *J. Chem. Rev.* **2007**, *107*, 1066-1096.
- (14) (a) “*Single-crystal DT-TTF-based OFETs*” Mas-Torrent, M.; Durkut, M.; Hadley, P.; Ribas, X.; Rovira, C. *J. Am. Chem. Soc.* **2004**, *126*, 984-985. (b) “*Correlation DT-TTF derivative*” Mas-Torrent, M.; Hadley, P.; Bromley, S. T.; Ribas, X.; Tarrés, J.; Mas, M.; Molins, E.; Veciana, J.; Rovira, C. *J. Am. Chem. Soc.* **2004**, *126*, 8546-8553. (c) Recently higher performance of DT-TTF-based single-crystal OFET was reported: Leufgen, M.; Rost, O.; Gould, C.; Schmidt, G.; Geurts, J.; Molenkamp, L.; Oxtoby, N.; Mas-Torrent, M.; Crivillers, N.; Veciana, J.; Rovira, C. *Org. Elect.* **2008**, *9*, 1101-1106. (d) “*DT-TTF polymorph*” Pfattner, R.; Mas-Torrent, M.; Bilotti, I.; Brillante, A.; Milita, S.; Liscio, F.; Biscarini, F.; Marszalek, T.; Ulanski, J.; Nosal, A.; Gazicki-Lipman, M.; Leufgen, M.; Schmidt, G.; Molenkamp, L. W.; Laukhin, V.; Veciana, J.; Rovira, C. *Adv. Mater.* **2010**, *22*, 4198-4203.
- (15) “*N-alkyl-PyTTFs*” Doi, I.; Miyazaki, E.; Takimiya, K.; Kunugi, Y. *Chem. Mater.* **2007**, *19*, 5230-5237.
- (16) “*N-acyl-PyTTFs*” Doi, I.; Miyazaki, E.; Takimiya, K. *Chem. Lett.* **2008**, *37*, 1088-1089.
- (17) “*DNTT*” Yamamoto, T.; Takimiya, K. *J. Am. Chem. Soc.* **2007**, *129*, 2224-2225.
- (18) “*DNTT on AlOx/SAM*” Zschieschang, U.; Ante, F.; Yamamoto, T.; Takimiya, K.; Kuwabara, H.; Ikeda, M.; Sekitani, T.; Someya, T.; Kern, K.; Klauk, H. *Adv. Mater.* **2010**, *22*, 982-985.
- (19) “*DNTT-based single-crystal OFETs*” Haas, S.; Takahashi, Y.; Takimiya, K.; Hasegawa, T. *Appl. Phys. Lett.* **2009**, *95*, 022111.
- (20) “*3D-OFET*” Uno, M.; Tominari, Y.; Yamagishi, M.; Doi, I.; Miyazaki, E.; Takimiya, K.; Takeya, J. *Appl. Phys. Lett.* **2009**, *94*, 223308.
- (21) “*Anisotropy DNTT*” Yamagishi, M.; Soeda, J.; Uemura, T.; Okada, Y.; Takatsuki, Y.; Nishikawa, T.; Nakazawa, Y.; Doi, I.; Takimiya, K.; Takeya, J. *Phys. Rev. B* **2010**, *81*, 161306.
- (22) “*C<sub>n</sub>-DNTT*” Kang, M. J.; Doi, I.; Mori, H.; Miyazaki, E.; Takimiya, K.; Ikeda, M.; Kuwabara, H. *Adv. Mater.* in press (DOI: 10.1002/adma.201001283).
- (23) “*C<sub>10</sub>-DNTT on Plastic Substrates*” Doi, I.; Myong-Jin, K.; Kazuo, T. *Cur. Appl. Phys.* submitted.
- (24) Heilmeyer, G. H.; Zanon, L. A. *J. Phys. Chem. Solids* **1964**, *25*, 603-611.
- (25) “*Polythiophene OFETs*” Tsumura, A.; Koezuka, H.; Ando, T. *Appl. Phys. Lett.* **1986**, *49*, 1210-1212.
- (26) Dimitrakopoulos, C.; Malenfant, P. *Adv. Mater.* **2002**, *14*, 99-117.
- (27) Dimitrakopoulos, C. D.; Furman, B. K.; Graham, T.; Hegde, S.; Purushothaman, S. *Synth. Met.* **1998**, *92*, 47-52.
- (28) Veres, J.; Ogier, S.; Lloyd, G.; de Leeuw, D. *Chem. Mater.* **2004**, *16*, 4543-4555.
- (29) “*Review*” Katz, H. E. *Chem. Mater.* **2004**, *16*, 4748-4756.
- (30) Osaka, I.; McCullough, R. D. *Advanced Functional Regioregular Polythiophenes* in Leclerc, M.; Morin, J. *Design and Synthesis of Conjugated Polymers*; Wiley-VCH, 2010.
- (31) Takimiya, K.; Sakamoto, K.; Otsubo, T.; Kunugi, Y. *Chem. Lett.* **2006**, *35*, 942-943.
- (32) Bao, Z.; Dodabalapur, A.; Lovinger, A. J. *Appl. Phys. Lett.* **1996**, *69*, 4108-4110.
- (33) Sirringhaus, H.; Tessler, N.; Friend, R. H. *Science* **1998**, *280*, 1741-1744.
- (34) Sirringhaus, H.; Brown, P. J.; Friend, R. H.; Nielsen, M. M.; Bechgaard, K.; Langeveld-Voss, B. M. W.; Spiering, A. J. H.; Janssen, R. A. J.; Meijer, E. W.; Herwig, P.; de Leeuw, D. M. *Nature* **1999**, *401*, 685-688.
- (35) Wang, G.; Swensen, J.; Moses, D.; Heeger, A. J. *J. Appl. Phys.* **2003**, *93*, 6137-6141.

## References

- (36) Chang, J.; Sun, B.; Breiby, D. W.; Nielsen, M. M.; Sölling, T. I.; Giles, M.; McCulloch, I.; Sirringhaus, H. *Chem. Mater.* **2004**, *16*, 4772-4776.
- (37) Kline, R.; McGehee, M.; Kadnikova, E.; Liu, J.; Fréchet, J. *Adv. Mater.* **2003**, *15*, 1519-1522.
- (38) Joseph Kline, R.; McGehee, M. D.; Toney, M. F. *Nat. Mater.* **2006**, *5*, 222-228.
- (39) Osaka, I.; McCullough, R. D. *Acc. Chem. Res.* **2008**, *41*, 1202-1214.
- (40) McCulloch, I.; Heeney, M.; Bailey, C.; Genevicius, K.; MacDonald, I.; Shkunov, M.; Sparrowe, D.; Tierney, S.; Wagner, R.; Zhang, W.; Chabynyc, M. L.; Kline, R. J.; McGehee, M. D.; Toney, M. F. *Nat. Mater.* **2006**, *5*, 328-333.
- (41) Umeda, T.; Kumaki, D.; Tokito, S. *J. Appl. Phys.* **2009**, *105*, 024516-5.
- (42) (a) Li, Y.; Wu, Y.; Liu, P.; Birau, M.; Pan, H.; Ong, B. *Adv. Mater.* **2006**, *18*, 3029-3032. (b) Nakayama, K.; Uno, M.; Nishikawa, T.; Nakazawa, Y.; Takeya, J. *Org. Elect.* **2010**, *11*, 1620-1623.
- (43) Osaka, I.; Zhang, R.; Sauvé, G.; Smilgies, D.; Kowalewski, T.; McCullough, R. D. *J. Am. Chem. Soc.* **2009**, *131*, 2521-2529.
- (44) Osaka, I.; Abe, T.; Shinamura, S.; Miyazaki, E.; Takimiya, K. *J. Am. Chem. Soc.* **2010**, *132*, 5000-5001.
- (45) Yan, H.; Chen, Z.; Zheng, Y.; Newman, C.; Quinn, J. R.; Dotz, F.; Kastler, M.; Facchetti, A. *Nature* **2009**, *457*, 679-686.
- (46) Anthony, J. E.; Facchetti, A.; Heeney, M.; Marder, S. R.; Zhan, X. *Adv. Mater.* **2010**, *22*, 3876-3892.
- (47) Kelley, T. *High-performance Pentacene Transistors*; Wiley-VCH Verlag GmbH & Co. KGaA, 2006.
- (48) Kelley, T. W.; Boardman, L. D.; Dunbar, T. D.; Muyres, D. V.; Pellerite, M. J.; Smith, T. P. *J. Phys. Chem. B* **2003**, *107*, 5877-5881.
- (49) Anthony, J. E. *Chem. Rev.* **2006**, *106*, 5028-5048.
- (50) Takimiya, K.; Kunugi, Y.; Otsubo, T. *Chem. Lett.* **2007**, *36*, 578-583.
- (51) Bao, Z.; Locklin, J. *Organic Field-Effect Transistors*; CRC Press, 2007.
- (52) 森 健彦, 長谷川達夫, 有機トランジスタ材料の評価と応用II, 第1～2章, p3 - 16, シーエムシー出版, 2008.
- (53) 小野昇, 低分子有機半導体の高性能化, *Science&Technology*, 2009.
- (54) Murphy, A. R.; Fréchet, J. M. J. *Chem. Rev.* **2007**, *107*, 1066-1096.
- (55) Sun, Y.; Liu, Y.; Zhu, D. *J. Mater. Chem.* **2005**, *15*, 53-65.
- (56) Takeya, J.; Kato, J.; Hara, K.; Yamagishi, M.; Hirahara, R.; Yamada, K.; Nakazawa, Y.; Ikehata, S.; Tsukagoshi, K.; Aoyagi, Y.; Takenobu, T.; Iwasa, Y. *Phys. Rev. Lett.* **2007**, *98*, 196804.
- (57) Braga, D.; Horowitz, G. *Adv. Mater.* **2009**, *21*, 1473-1486.
- (58) Briseno, A. L.; Mannsfeld, S. C. B.; Ling, M. M.; Liu, S.; Tseng, R. J.; Reese, C.; Roberts, M. E.; Yang, Y.; Wudl, F.; Bao, Z. *Nature* **2006**, *444*, 913-917.
- (59) de Boer, R. W. I.; Klapwijk, T. M.; Morpurgo, A. F. *Appl. Phys. Lett.* **2003**, *83*, 4345-4347.
- (60) Li, R.; Jiang, L.; Meng, Q.; Gao, J.; Li, H.; Tang, Q.; He, M.; Hu, W.; Liu, Y.; Zhu, D. *Adv. Mater.* **2009**, *21*, 4492-4495.
- (61) (a) Takeya, J.; Yamagishi, M.; Tominari, Y.; Hirahara, R.; Nakazawa, Y.; Nishikawa, T.; Kawase, T.; Shimoda, T.; Ogawa, S. *Appl. Phys. Lett.* **2007**, *90*, 102120. (b) Uno, M.; Tominari, Y.; Takeya, J. *Org. Elect.* **2008**, *9*, 753-756.
- (62) Hasegawa, T.; Takeya, J. *Sci. Technol. Adv. Mater.* **2009**, *10*, 024314.
- (63) Afzali, A.; Dimitrakopoulos, C. D.; Breen, T. L. *J. Am. Chem. Soc.* **2002**, *124*, 8812-8813.
- (64) Weidkamp, K. P.; Afzali, A.; Tromp, R. M.; Hamers, R. J. *J. Am. Chem. Soc.* **2004**, *126*, 12740-12741.
- (65) Hirao, A.; Akiyama, T.; Okujima, T.; Yamada, H.; Uno, H.; Sakai, Y.; Aramaki, S.; Ono, N. *Chem. Commun.* **2008**, 4714-4716.
- (66) Murphy, A. R.; Fréchet, J. M. J.; Chang, P.; Lee, J.; Subramanian, V. *J. Am. Chem. Soc.* **2004**, *126*, 1596-1597.
- (67) Sirringhaus, H. *Adv. Mater.* **2005**, *17*, 2411-2425.
- (68) Anthony, J. E.; Eaton, D. L.; Parkin, S. R. *Org. Lett.* **2002**, *4*, 15-18.
- (69) Payne, M. M.; Parkin, S. R.; Anthony, J. E.; Kuo, C.; Jackson, T. N. *J. Am. Chem. Soc.* **2005**, *127*, 4986-4987.
- (70) Llorente, G. R.; Dufourg-Madec, M.; Crouch, D. J.; Pritchard, R. G.; Ogier, S.; Yeates, S. G. *Chem. Commun.* **2009**, 3059-3061.
- (71) Laquindanum, J. G.; Katz, H. E.; Lovinger, A. J. *J. Am. Chem. Soc.* **1998**, *120*, 664-672.
- (72) Curtis, M. D.; Cao, J.; Kampf, J. W. *J. Am. Chem. Soc.* **2004**, *126*, 4318-4328.
- (73) Kondo, R.; Higa, M.; Kagoshima, S.; Hoshino, H.; Mori, T.; Mori, H. *J. Phys. Soc. Jpn.* **2006**, *75*, 044716.
- (74) Halik, M.; Klauk, H.; Zschieschang, U.; Schmid, G.; Ponomarenko, S.; Kirchmeyer, S.; Weber, W. *Adv. Mater.* **2003**, *15*, 917-922.
- (75) Gao, X.; Wang, Y.; Yang, X.; Liu, Y.; Qiu, W.; Wu, W.; Zhang, H.; Qi, T.; Liu, Y.; Lu, K.; Du, C.; Shuai, Z.; Yu, G.; Zhu, D. *Adv. Mater.* **2007**, *19*, 3037-3042.
- (76) Meng, H.; Sun, F.; Goldfinger, M. B.; Jaycox, G. D.; Li, Z.; Marshall, W. J.; Blackman, G. S. *J. Am. Chem. Soc.* **2005**, *127*, 2406-2407.

- (77) (a) Yamada, J.; Sugimoto, T. *TTF Chemistry: Fundamentals And Applications Of Tetrathiafulvalene*; Springer-Verlag, 2004. (b) Otsubo, T.; Takimiya, K. *Bull. Chem. Soc. J.* **2004**, *77*, 43-58.
- (78) Mas-Torrent, M.; Rovira, C. *J. Mater. Chem.* **2006**, *16*, 433-436.
- (79) Iizuka, M.; Shiratori, Y.; Kuniyoshi, S.; Kudo, K.; Tanaka, K. *Applied Surface Science* **1998**, *130-132*, 914-918.
- (80) Noda, B.; Katsuhara, M.; Aoyagi, I.; Mori, T.; Taguchi, T.; Kambayashi, T.; Ishikawa, K.; Takezoe, H. *Chem. Lett.* **2005**, *34*, 392-393.
- (81) Miskiewicz, P.; Mas-Torrent, M.; Jung, J.; Kotarba, S.; Glowacki, I.; Gomar-Nadal, E.; Amabilino, D. B.; Veciana, J.; Krause, B.; Carbone, D.; Rovira, C.; Ulanski, J. *Chem. Mater.* **2006**, *18*, 4724-4729.
- (82) Mori, T. *J. Phys. Cond. Mater* **2008**, *20*, 184010.
- (83) Naraso; Nishida, J.; Ando, S.; Yamaguchi, J.; Itaka, K.; Koinuma, H.; Tada, H.; Tokito, S.; Yamashita, Y. *J. Am. Chem. Soc.* **2005**, *127*, 10142-10143.
- (84) Naraso; Nishida, J.; Kumaki, D.; Tokito, S.; Yamashita, Y. *J. Am. Chem. Soc.* **2006**, *128*, 9598-9599.
- (85) Yoshino, T.; Shibata, K.; Wada, H.; Bando, Y.; Ishikawa, K.; Takezoe, H.; Mori, T. *Chem. Lett.* **2009**, *38*, 200-201.
- (86) Mas-Torrent, M.; Hadley, P.; Bromley, S. T.; Crivillers, N.; Veciana, J.; Rovira, C. *Appl. Phys. Lett.* **2005**, *86*, 012110.
- (87) Takahashi, Y.; Hasegawa, T.; Horiuchi, S.; Kumai, R.; Tokura, Y.; Saito, G. *Chem. Mater.* **2007**, *19*, 6382-6384.
- (88) Kanno, M.; Bando, Y.; Shirahata, T.; Inoue, J.; Wada, H.; Mori, T. *J. Mater. Chem.* **2009**, *19*, 6548-6555.
- (89) Yamada, T.; Kumai, R.; Takahashi, Y.; Hasegawa, T. *J. Mater. Chem.* **2010**, *20*, 5810-5812.
- (90) Inoue, J.; Kanno, M.; Ashizawa, M.; Seo, C.; Tanioka, A.; Mori, T. *Chem. Lett.* **2010**, *39*, 538-540.
- (91) Morioka, Y.; Nishida, J.; Fujiwara, E.; Tada, H.; Yamashita, Y. *Chem. Lett.* **2004**, *33*, 1632-1633.
- (92) Gao, X.; Wu, W.; Liu, Y.; Qiu, W.; Sun, X.; Yu, G.; Zhu, D. *Chem. Commun.* **2006**, 2750-2752.
- (93) Bando, Y.; Shirahata, T.; Shibata, K.; Wada, H.; Mori, T.; Imakubo, T. *Chem. Mater.* **2008**, *20*, 5119-5121.
- (94) Katsuhara, M.; Aoyagi, I.; Nakajima, H.; Mori, T.; Kambayashi, T.; Ofuji, M.; Takanishi, Y.; Ishikawa, K.; Takezoe, H.; Hosono, H. *Synth. Met.* **2005**, *149*, 219-223.
- (95) Simonsen, K. B.; Svenstrup, N.; Lau, J.; Simonsen, O.; Mørk, P.; Kristensen, G. J.; Becher, J. *Synthesis* **1996**, *1996*, 407-418.
- (96) Takimiya, K.; Oharuda, A.; Aso, Y.; Ogura, F.; Otsubo, T. *Chem. Mater.* **2000**, *12*, 2196-2204.
- (97) Jigami, T.; Takimiya, K.; Otsubo, T.; Aso, Y. *J. Org. Chem.* **1998**, *63*, 8865-8872.
- (98) Jeppesen, J. O.; Takimiya, K.; Thorup, N.; Becher, J. *Synthesis* **1999**, *1999*, 803,810.
- (99) Jeppesen, J. O.; Takimiya, K.; Jensen, F.; Brimert, T.; Nielsen, K.; Thorup, N.; Becher, J. *J. Org. Chem.* **2000**, *65*, 5794-5805.
- (100) Stueber, D.; Patterson, D.; Mayne, C. L.; Orendt, A. M.; Grant, D. M.; Parry, R. W. *Inorganic Chemistry* **2001**, *40*, 1902-1911.
- (101) Ferraris, J. P.; Poehler, T. O.; Bloch, A. N.; Cowan, D. O. *Tetrahedron Letters* **1973**, *14*, 2553-2556.
- (102) Renner, R. M.; Burns, G. R. *Tetrahedron Letters* **1994**, *35*, 269-272.
- (103) Crivillers, N.; Oxtoby, N. S.; Mas-Torrent, M.; Veciana, J.; Rovira, C. *Synthesis* **2007**, *2007*, 1621,1623.
- (104) Cornil, J.; Calbert, J. P.; Beljonne, D.; Silbey, R.; Brédas, J. *Adv. Mater.* **2000**, *12*, 978-983.
- (105) Cornil, J.; Beljonne, D.; Calbert, J.; Brédas, J. *Adv. Mater.* **2001**, *13*, 1053-1067.
- (106) Altomare, A.; Cascarano, G.; Giacovazzo, C.; Guagliardi, A.; Burla, M. C.; Polidori, G.; Camalli, M. *Journal of Applied Crystallography* **1994**, *27*, 435.
- (107) Sheldrick, G. M. *Program for the Refinement of Crystal Structures*; University of Göttingen: Göttingen, Germany, 1997.
- (108) *teXsan: Single Crystal Structure Analysis Software, Version 1.19*; Molecular Structure Corporation and Rigaku Corporation, 2000.
- (109) Takimiya, K.; Yamamoto, T.; Ebata, H.; Izawa, T. *Sci. Technol. Adv. Mater.* **2007**, *8*, 273-276.
- (110) Winkler, M.; Houk, K. N. *J. Am. Chem. Soc.* **2007**, *129*, 1805-1815.
- (111) Calculated by Gaussian 03 program. M. J. Frisch, G. W. Trucks, H. B. Schlegel, G. E. Scuseria, M. A. Robb, J. R. Cheeseman, J. A. Montgomery, Jr., T. Vreven, K. N. Kudin, J. C. Burant, J. M. Millam, S. S. Iyengar, J. Tomasi, V. Barone, B. Mennucci, M. Cossi, G. Scalmani, N. Rega, G. A. Petersson, H. Nakatsuji, M. Hada, M. Ehara, K. Toyota, R. Fukuda, J. Hasegawa, M. Ishida, T. Nakajima, Y. Honda, O. Kitao, H. Nakai, M. Klene, X. Li, J. E. Knox, H. P. Hratchian, J. B. Cross, V. Bakken, C. Adamo, J. Jaramillo, R. Gomperts, R. E. Stratmann, O. Yazyev, A. J. Austin, R. Cammi, C. Pomelli, J. W. Ochterski, P. Y. Ayala, K. Morokuma, G. A. Voth, P. Salvador, J. J. Dannenberg, V. G. Zakrzewski, S. Dapprich, A. D. Daniels, M. C. Strain, O. Farkas, D. K. Malick, A. D. Rabuck, K. Raghavachari, J. B. Foresman, J. V. Ortiz, Q. Cui, A. G. Baboul, S. Clifford, J. Cioslowski, B. B. Stefanov, G. Liu, A. Liashenko, P. Piskorz, I. Komaromi, R. L. Martin, D. J. Fox, T. Keith, M. A. Al-Laham, C. Y. Peng, A. Nanayakkara, M. Challacombe, P. M. W. Gill, B. Johnson, W. Chen, M. W. Wong, C. Gonzalez, J. A. Pople, Gaussian 03, Revision C.02, Gaussian, Inc., Wallingford CT, 2004.
- (112) Pommerehne, J.; Vestweber, H.; Guss, W.; Mahrt, R. F.; Bäessler, H.; Porsch, M.; Daub, J. *Adv. Mater.* **1995**, *7*, 551-554.
- (113) Balaji, G.; Phua, D. I.; Shim, W. L.; Valiyaveetil, S. *Org. Lett.* **2010**, *12*, 232-235.

## References

- (114) Jung, S.; Yao, Z. *Appl. Phys. Lett.* **2005**, *86*, 083505.
- (115) Huang, J.; Sun, J.; Katz, H. E. *Adv. Mater.* **2008**, *20*, 2567-2572.
- (116) Ruiz, R.; Papadimitratos, A.; Mayer, A.; Malliaras, G. *Adv. Mater.* **2005**, *17*, 1795-1798.
- (117) Miyazaki, E.; Kaku, A.; Mori, H.; Iwatani, M.; Takimiya, K. *J. Mater. Chem.* **2009**, *19*, 5913-5915.
- (118) Engler, E. M.; Patel, V. V.; Andersen, J. R.; Schumaker, R. R.; Fukushima, A. A. *J. Am. Chem. Soc.* **1978**, *100*, 3769-3776.
- (119) Santalo, N.; Veciana, J.; Rovira, C.; Molins, E.; Miravittles, C.; Claret, J. *Synth. Met.* **1991**, *42*, 2205-2209.
- (120) Rovira, C.; Veciana, J.; Santalo, N.; Tarres, J.; Cirujeda, J.; Molins, E.; Llorca, J.; Espinosa, E. *J. Org. Chem.* **1994**, *59*, 3307-3313.
- (121) Rovira, C. *Chem. Rev.* **2004**, *104*, 5289-5318.
- (122) Kumaki, D.; Yahiro, M.; Inoue, Y.; Tokito, S. *Appl. Phys. Lett.* **2007**, *90*, 133511.
- (123) Klauk, H.; Halik, M.; Zschieschang, U.; Schmid, G.; Radlik, W.; Weber, W. *J. Appl. Phys.* **2002**, *92*, 5259-5263.
- (124) "C<sub>n</sub>-BTBT" Ebata, H.; Izawa, T.; Miyazaki, E.; Takimiya, K.; Ikeda, M.; Kuwabara, H.; Yui, T. *J. Am. Chem. Soc.* **2007**, *129*, 15732-15733.
- (125) Izawa, T.; Miyazaki, E.; Takimiya, K. *Adv. Mater.* **2008**, *20*, 3388-3392.
- (126) Yamamoto, T.; Shinamura, S.; Miyazaki, E.; Takimiya, K. *Bull. Chem. Soc. J.* **2010**, *83*, 120-130.
- (127) Sánchez-Carrera, R. S.; Atahan, S.; Schrier, J.; Aspuru-Guzik, A. *J. Phys. Chem. C* **2010**, *114*, 2334-2340.
- (128) Valiyev, F.; Hu, W.; Chen, H.; Kuo, M.; Chao, I.; Tao, Y. *Chem. Mater.* **2007**, *19*, 3018-3026.
- (129) Gao, X.; Qiu, W.; Liu, Y.; Yu, G.; Zhu, D. *Pure Appl. Chem.* **2008**, *80*, 2405-2423.
- (130) (a) Bromley, S. T.; Mas-Torrent, M.; Hadley, P.; Rovira, C. *J. Am. Chem. Soc.* **2004**, *126*, 6544-6545.
- (131) Casado, J.; Zgierski, M. Z.; Delgado, M. C. R.; Navarrete, J. T. L.; Mas-Torrent, M.; Rovira, C. *J. Phys. Chem. C* **2007**, *111*, 10110-10118.
- (132) Takimiya, K.; Kunugi, Y.; Konda, Y.; Ebata, H.; Toyoshima, Y.; Otsubo, T. *J. Am. Chem. Soc.* **2006**, *128*, 3044-3050.
- (133) Cornil, J.; Calbert, J. P.; Brédas, J. L. *J. Am. Chem. Soc.* **2001**, *123*, 1250-1251.
- (134) Coropceanu, V.; Cornil, J.; da Silva Filho, D. A.; Olivier, Y.; Silbey, R.; Brédas, J. *Chem. Rev.* **2007**, *107*, 926-952.
- (135) Kim, E.; Coropceanu, V.; Gruhn, N. E.; Sánchez-Carrera, R. S.; Snoeberger, R.; Matzger, A. J.; Brédas, J. *J. Am. Chem. Soc.* **2007**, *129*, 13072-13081.
- (136) Valeev, E. F.; Coropceanu, V.; da Silva Filho, D. A.; Salman, S.; Brédas, J. *J. Am. Chem. Soc.* **2006**, *128*, 9882-9886.
- (137) Marcus, R. *Rev. Mod. Phys.* **1993**, *65*, 599-610.
- (138) Delgado, M. C. R.; Pigg, K. R.; da Silva Filho, D. A.; Gruhn, N. E.; Sakamoto, Y.; Suzuki, T.; Osuna, R. M.; Casado, J.; Hernández, V.; Navarrete, J. T. L.; Martinelli, N. G.; Cornil, J.; Sánchez-Carrera, R. S.; Coropceanu, V.; Brédas, J. *J. Am. Chem. Soc.* **2009**, *131*, 1502-1512.
- (139) ADF2008.01. Scientific Computing & Modeling (SCM), Theoretical Chemistry, Vrije Universiteit, Amsterdam, The Netherlands, <http://www.scm.com>
- (140) Prins, P.; Senthilkumar, K.; Grozema, F. C.; Jonkheijm, P.; Schenning, A. P. H. J.; Meijer, E. W.; Siebbeles, L. D. A. *J. Phys. Chem. B* **2005**, *109*, 18267-18274.
- (141) Senthilkumar, K.; Grozema, F. C.; Bickelhaupt, F. M.; Siebbeles, L. D. A. *J. Chem. Phys.* **2003**, *119*, 9809-9817.
- (142) Mori, T.; Kobayashi, A.; Sasaki, Y.; Kobayashi, H.; Saito, G.; Inokuchi, H. *Bull. Chem. Soc. Jpn.* **1984**, *57*, 627-633.
- (143) Mori, T. *Bull. Chem. Soc. J.* **1998**, *71*, 2509-2526.
- (144) Appleton, A. L.; Miao, S.; Brombosz, S. M.; Berger, N. J.; Barlow, S.; Marder, S. R.; Lawrence, B. M.; Hardcastle, K. I.; Bunz, U. H. F. *Org. Lett.* **2009**, *11*, 5222-5225.
- (145) Klauk, H.; Halik, M.; Zschieschang, U.; Eder, F.; Schmid, G.; Dehm, C. *Appl. Phys. Lett.* **2003**, *82*, 4175-4177.
- (146) Kitamura, M.; Arakawa, Y. *J. Phys.: Condens. Matter* **2008**, *20*, 184011.
- (147) Tan, H. S.; Mathews, N.; Cahyadi, T.; Zhu, F. R.; Mhaisalkar, S. G. *Appl. Phys. Lett.* **2009**, *94*, 263303.
- (148) Takimiya, K.; Ebata, H.; Sakamoto, K.; Izawa, T.; Otsubo, T.; Kunugi, Y. *J. Am. Chem. Soc.* **2006**, *128*, 12604-12605.
- (149) Okamura, K.; Nikolova, D.; Mechau, N.; Hahn, H. *Appl. Phys. Lett.* **2009**, *94*, 183503.
- (150) Walser, M. P.; Kalb, W. L.; Mathis, T.; Batlogg, B. *Appl. Phys. Lett.* **2009**, *95*, 233301.
- (151) Kumaki, D.; Umeda, T.; Tokito, S. *Appl. Phys. Lett.* **2008**, *92*, 013301.
- (152) Kano, M.; Minari, T.; Tsukagoshi, K. *Appl. Phys. Lett.* **2009**, *94*, 143304.
- (153) (a) Anthopoulos, T. D.; Singh, B.; Marjanovic, N.; Sariciftci, N. S.; Ramil, A. M.; Sitter, H.; Colle, M.; de Leeuw, D. M. *Appl. Phys. Lett.* **2006**, *89*, 213504. (b) Itaka, K.; Yamashiro, M.; Yamaguchi, J.; Haemori, M.; Yaginuma, S.; Matsumoto, Y.; Kondo, M.; Koinuma, H. *Adv. Mater.* **2006**, *18*, 1713-1716.
- (154) Shukla, D.; Nelson, S. F.; Freeman, D. C.; Rajeswaran, M.; Ahearn, W. G.; Meyer, D. M.; Carey, J. T. *Chem. Mater.* **2008**, *20*, 7486-7491.
- (155) Ong, B. S.; Wu, Y.; Liu, P.; Gardner, S. *J. Am. Chem. Soc.* **2004**, *126*, 3378-3379.

- (156)Pernstich, K. P.; Haas, S.; Oberhoff, D.; Goldmann, C.; Gundlach, D. J.; Batlogg, B.; Rashid, A. N.; Schitter, G. *J. Appl. Phys.* **2004**, *96*, 6431-6438.
- (157)Suemori, K.; Uemura, S.; Yoshida, M.; Hoshino, S.; Takada, N.; Kodzasa, T.; Kamata, T. *Appl. Phys. Lett.* **2007**, *91*, 192112.
- (158)森 健彦, 長谷川達夫, 有機トランジスタ材料の評価と応用II, 第4章, p117-128, シーエムシー出版, 2008.
- (159)Halik, M. *Gate Dielectrics* in Klauk, H *Organic Electronics: Materials, Manufacturing, and Applications*, Wiley-VCH Verlag GmbH & Co. KGaA, 2006.
- (160)Kim, C.; Wang, Z.; Choi, H.; Ha, Y.; Facchetti, A.; Marks, T. J. *J. Am. Chem. Soc.* **2008**, *130*, 6867-6878.
- (161)Pokhodnya, K. I.; Bonner, M.; Miller, J. S. *Chem. Mater.* **2004**, *16*, 5114-5119.
- (162)Podzorov, V.; Pudalov, V. M.; Gershenson, M. E. *Appl. Phys. Lett.* **2003**, *82*, 1739-1741.
- (163)Podzorov, V.; Sysoev, S. E.; Loginova, E.; Pudalov, V. M.; Gershenson, M. E. *Appl. Phys. Lett.* **2003**, *83*, 3504-3506.
- (164)Sekitani, T.; Nakajima, H.; Maeda, H.; Fukushima, T.; Aida, T.; Hata, K.; Someya, T. *Nat. Mater.* **2009**, *8*, 494-499.
- (165)Someya, T.; Sekitani, T.; Iba, S.; Kato, Y.; Kawaguchi, H.; Sakurai, T. *Proceedings of the National Academy of Sciences of the United States of America* **2004**, *101*, 9966 -9970.
- (166)Umeda, T.; Kumaki, D.; Tokito, S. *Org. Elect.* **2008**, *9*, 545-549.
- (167)Deshmukh, K. D.; Reuter, K.; Kempa, H.; West, J. E.; Katz, H. E. *Appl. Phys. Lett.* **2009**, *95*, 113307.
- (168)Jang, J.; Kim, J. W.; Park, N.; Kim, J. *Org. Elect.* **2008**, *9*, 481-486.
- (169)Kaji, Y.; Kawasaki, N.; Lee, X.; Okamoto, H.; Sugawara, Y.; Oikawa, S.; Ito, A.; Okazaki, H.; Yokoya, T.; Fujiwara, A.; Kubozono, Y. *Appl. Phys. Lett.* **2009**, *95*, 183302.
- (170)Kalb, W. L.; Mathis, T.; Haas, S.; Stassen, A. F.; Batlogg, B. *Appl. Phys. Lett.* **2007**, *90*, 092104.
- (171)Smith, J.; Hamilton, R.; McCulloch, I.; Heeney, M.; Anthony, J. E.; Bradley, D. D.; Anthopoulos, T. D. *Synth. Met.* **2009**, *159*, 2365-2367.
- (172)Walser, M. P.; Kalb, W. L.; Mathis, T.; Brenner, T. J.; Batlogg, B. *Appl. Phys. Lett.* **2009**, *94*, 053303.
- (173)Walser, M. P.; Kalb, W. L.; Mathis, T.; Batlogg, B. *Appl. Phys. Lett.* **2009**, *95*, 233301-3.
- (174)Uno, M.; Tominari, Y.; Yamagishi, M.; Doi, I.; Miyazaki, E.; Takimiya, K.; Takeya, J. *Appl. Phys. Lett.* **2009**, *94*, 223308.
- (175)時任 静士他 “フルオロポリマーをゲート絶縁膜に用いたボトムコンタクト有機TFTアレイの試作”  
2009年春期応用物理学関係連合講演会
- (176)Fukuda, K.; Sekitani, T.; Someya, T. *Appl. Phys. Lett.* **2009**, *95*, 023302-3.
- (177)Kato, Y.; Sekitani, T.; Takamiya, M.; Doi, M.; Asaka, K.; Sakurai, T.; Someya, T. *IEEE Trans. Electron Devices* **2007**, *54*, 202-209.
- (178)Ahn, T.; Choi, Y.; Jung, H. M.; Yi, M. *Org. Elect.* **2009**, *10*, 12-17.
- (179)Sekitani, T.; Iba, S.; Kato, Y.; Noguchi, Y.; Someya, T.; Sakurai, T. *Appl. Phys. Lett.* **2005**, *87*, 073505.
- (180)Kato, Y.; Iba, S.; Teramoto, R.; Sekitani, T.; Someya, T.; Kawaguchi, H.; Sakurai, T. *Appl. Phys. Lett.* **2004**, *84*, 3789-3791.
- (181)Roberts, M. E.; Mannsfeld, S. C.; Stoltenberg, R. M.; Bao, Z. *Org. Elect.* **2009**, *10*, 377-383.
- (182)Kawaguchi, H.; Iba, S.; Kato, Y.; Semitani, T.; Someya, T.; Sakurai, T. *IEEE Sensors Journal* **2006**, *6*, 1209-1217.
- (183)Maliakal, A.; Raghavachari, K.; Katz, H.; Chandross, E.; Siegrist, T. *Chem. Mater.* **2004**, *16*, 4980-4986.
- (184)Hanada, T.; Negishi, T.; Shiroishi, I.; Shiro, T. *Thin Solid Films* **2010**, *518*, 3089-3092.
- (185)Kano, M.; Minari, T.; Tsukagoshi, K. *Appl. Phys. Express* **2010**, *3*, 051601.



## Appendix

## A1. OFET Operation

**P- and n-channel operations.** Energy levels of frontier orbitals, namely, a highest occupied molecular orbital (HOMO) or a lowest unoccupied molecular orbital (LUMO) of an organic semiconductor, determine the p- or n-channel FET operation. The frontier energy-levels also affect the air-stability of the FET characteristics (Figure A1). The energy levels are determined from the electronic potential of the compound in solutions. Work functions ( $\Phi$ ) (Fermi energy,  $\epsilon_F$ ) of metal electrodes and energy levels of HOMO or LUMO should be close for smooth carrier injection.

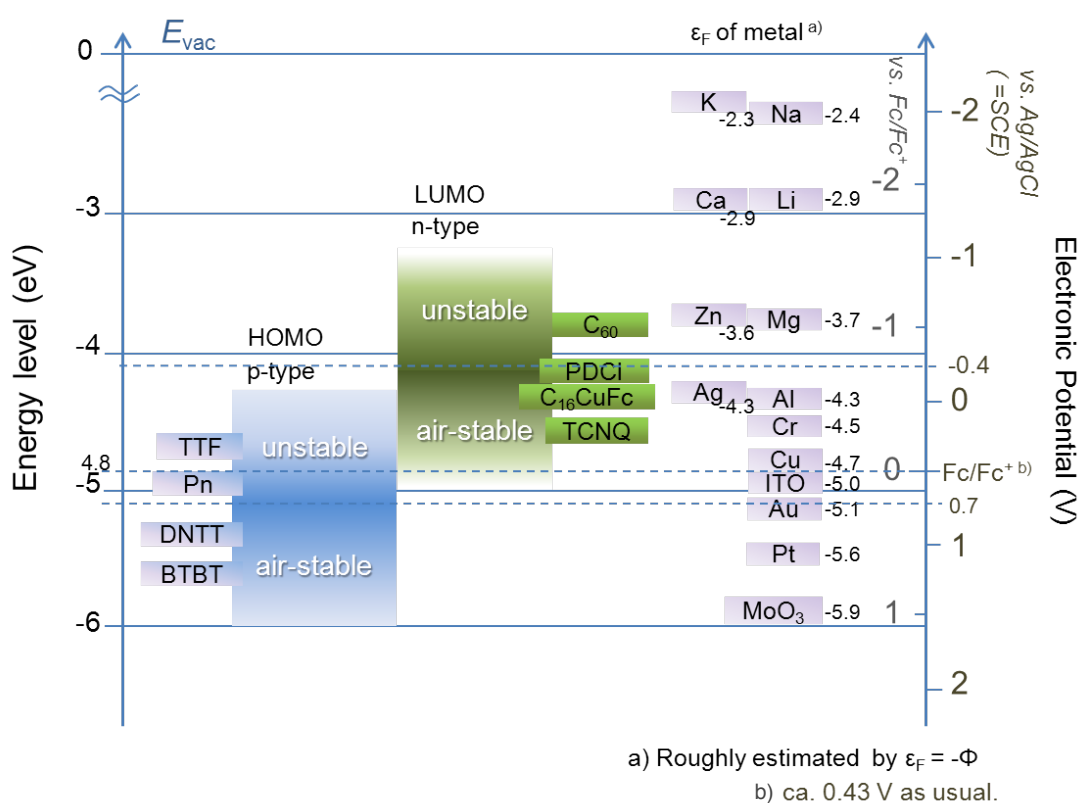


**Figure A1.** Relationship between energy levels of frontier orbitals of organic semiconductors and stable/unstable p- or n-type operation of OFETs in air. Work functions ( $= \epsilon_F$ ) of metals are also depicted.

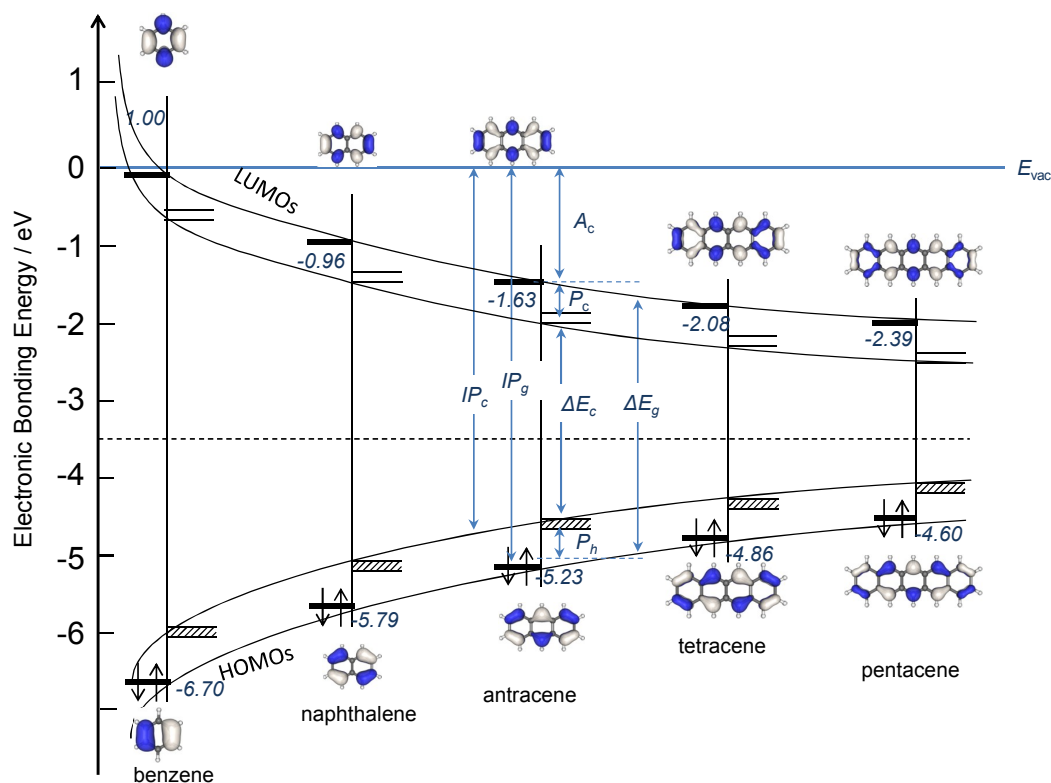


**Figure A2.** Energy band structure of the acene compounds. The calculation is based on DFT method at B3LYP/6-31(d) level.<sup>111</sup>

**Relationship Between Molecular Structures and HOMO-LUMO energy levels.** The HOMO and LUMO levels of the  $\pi$ -compounds are changed linearly with increase in the extension of  $\pi$ -conjugation (Figure A2). The relationship can be confirmed by molecular orbital calculations.<sup>111</sup> It is noted that an energy level in a solid state increases somewhat (polarization energy,  $P_c$  or  $P_h$ ) due to formation of a small band structure. Thus an ionization potential in a gas state ( $IP_g$ ) is different from that in a solid state ( $IP_c$ ).

## A2. Nomenclature of tetrathiafulvalene derivatives

**Common Name vs IUPAC Name.** The compound and name of tetrathiafulvalene (TTF) is widely known, however, the name of TTF is not admit by IUPAC (International Union of Pure and Applied Chemistry) nomenclature. Structure of TTF is named by IUPAC as “2,2’-bis(1,3-dithiolylidene)”(Figure A3a), which derived from the name of “1,1’-bi(cyclopenta-2,4-diene-1-ylidene)” (Figure A3b).

Other name of TTF is traditionally given by “ $\Delta^{2,2'}$ -bi-1,3-dithiole”, where  $\Delta$  expresses that the same structures are connected by double bond at the numbering positions. It is frequently used when naming quinoidal compounds. The names of thiophene-fused TTFs are in Figure A4.

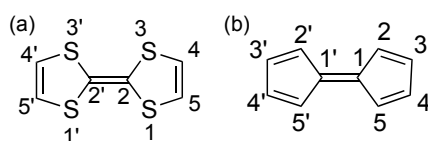


**Figure A3.** Numbering of (a) TTF and an (b) analogy.

Nomenclature	Name
common 1	dithiophene-tetrathiafulvalene (DT-TTF)
common 2	bis(thiophene[3,4- <i>d</i> ])tetrathiafulvalene
traditional	$\Delta^{2,2'}$ -bitheno[3,4- <i>d</i> ]-1,3-dithiole
IUPAC	2-(thieno[3,4- <i>d</i> ]-1,3-dithiole-2-ylidene)thieno[3,4- <i>d</i> ]-1,3-dithiole

Nomenclature	Name
common 1	$\alpha$ -dithiophene-tetrathiafulvalene ( $\alpha$ DT-TTF)
common 2	( <i>Z</i> )/( <i>E</i> )-bis(thieno[2,3- <i>d</i> ])tetrathiafulvalene
traditional	( <i>Z</i> )/( <i>E</i> )- $\Delta^{2,2'}$ -bithieno[2,3- <i>d</i> ]-1,3-dithiole
IUPAC	( <i>Z</i> )/( <i>E</i> )-2-(thieno[2,3- <i>d</i> ]-1,3-dithiole-2-ylidene)thieno[2,3- <i>d</i> ]-1,3-dithiole

Nomenclature	Name
common	bis(pyrrolo[3,4- <i>d</i> ])tetrathiafulvalene (PyTTF)
traditional	$\Delta^{2,2'}$ -bipyrrolo[3,4- <i>d</i> ]-1,3-dithiole
IUPAC	2-(pyrrolo[3,4- <i>d</i> ]-1,3-dithiole-2-ylidene)pyrrolo[3,4- <i>d</i> ]-1,3-dithiole

**Figure A4.** Nomenclatures of TTF derivatives.

## A3. Crystallographic Data for X-ray Single-Crystal Structure Analyses

75

Table A1 Crystal Data for the heteroaromatic-fused TTFs

	<b>1a</b> (H-PyTTF)	<b>1c</b> (n-butyl-PyTTF)	<b>1d</b> (n-octyl-PyTTF)	<b>1e</b> (n-dodecyl-PyTTF)	<b>1f</b> (n-cetyl-PyTTF)	<b>2b</b> (n-hexanoyl-PyTTF)	<b>3a</b> (nDT-TTF)	<b>3b</b> (methyl-nDT-TTF)	<b>3c</b> (S-n-octyl-nDT-TTF)	
Empirical Formula	C <sub>10</sub> H <sub>6</sub> N <sub>2</sub> S <sub>4</sub>	C <sub>18</sub> H <sub>22</sub> S <sub>4</sub> N <sub>2</sub>	C <sub>26</sub> H <sub>38</sub> N <sub>2</sub> S <sub>4</sub>	C <sub>34</sub> H <sub>54</sub> N <sub>2</sub> S <sub>4</sub>	C <sub>42</sub> S <sub>4</sub> N <sub>2</sub> H <sub>70</sub>	C <sub>22</sub> H <sub>26</sub> N <sub>2</sub> O <sub>5</sub> S <sub>4</sub>	C <sub>10</sub> H <sub>4</sub> S <sub>6</sub>	C <sub>12</sub> S <sub>4</sub> H <sub>8</sub>	C <sub>26</sub> H <sub>36</sub> S <sub>8</sub>	C <sub>10</sub> H <sub>4</sub> Se <sub>2</sub> S <sub>4</sub>
Formula Weight	282.41	394.63	506.84	619.05	731.27	478.70	316.50	344.56	605.03	410.30
Crystallization From	acetone	toluene	chlorobenzene	toluene	chlorobenzene	sublimation (~10 <sup>3</sup> Pa)	toluene	toluene	benzene	chlorobenzene
Crystal Color, Habit	yellow, platelet	yellow, block	yellow, block	yellow, block	yellow, platelet	yellow, block	red, platelet	red, platelet	orange, platelet	red, platelet
Crystal Dimensions	0.25 × 0.20 × 0.10 mm	0.50 × 0.20 × 0.10 mm	0.25 × 0.50 × 0.40 mm	0.30 × 0.20 × 0.05 mm	0.30 × 0.25 × 0.20 mm	0.50 × 0.30 × 0.15 mm	1.00 × 0.20 × 0.20 mm	2.00 × 1.60 × 0.10 mm	0.15 × 0.15 × 0.02 mm	0.50 × 0.20 × 0.01 mm
Crystal System	monoclinic	<i>monoclinic</i>	monoclinic	triclinic	triclinic	triclinic	monoclinic	triclinic	monoclinic	monoclinic
Lattice Parameters	a = 29.0(2) Å b = 7.80(6) Å c = 9.72(7) Å	a = 10.237(4) Å b = 11.170(4) Å c = 8.139(4) Å	a = 9.929(5) Å b = 10.846(5) Å c = 12.603(3) Å	a = 4.659(4) Å b = 7.680(8) Å c = 23.82(2) Å	a = 5.394(3) Å b = 7.502(3) Å c = 26.92(2) Å	a = 4.914(4) Å b = 10.260(8) Å c = 22.87(2) Å	a = 6.1828(5) Å b = 15.455(1) Å c = 18.617(1) Å	a = 7.742(3) Å b = 9.742(3) Å c = 10.785(3) Å	a = 10.326 Å b = 4.214 Å c = 34.056 Å	a = 6.265(2) Å b = 16.195(4) Å c = 6.303(2) Å
	β = 93.26(3) °	β = 91.51(2) °	β = 92.51(1) °	α = 80.75(3) ° β = 83.92(3) ° γ = 85.96(3) °	α = 92.34(2) ° β = 94.06(2) ° γ = 103.68(2) °	α = 96.18(1) ° β = 91.54(1) ° γ = 90.84(1) °	β = 95.09(2) °	β = 103.041(9) ° γ = 105.033(8) °	β = 94.81 °	β = 109.45(1) °
Space Group	C2/c (#15)	P2 <sub>1</sub> /a (#14)	V = 930(7) Å <sup>3</sup> P2 <sub>1</sub> /a (#14)	V = 835(5) Å <sup>3</sup> P1 (#2)	V = 1053.8(9) Å <sup>3</sup> P1 (#2)	V = 1145(1) Å <sup>3</sup> P1 (#2)	V = 1772.0(2) Å <sup>3</sup> P2 <sub>1</sub> /n (#14)	V = 696.5(4) Å <sup>3</sup> P1 (#2)	V = 1476.7 Å <sup>3</sup> P2 <sub>1</sub> /a (#14)	V = 603.0(3) Å <sup>3</sup> P2 <sub>1</sub> /a (#14)
Z value	8	2	2	1	1	2	6	2	2	2
μ (MoKα)	8.33 cm <sup>-1</sup>	5.13 cm <sup>-1</sup>	3.67 cm <sup>-1</sup>	3.10 cm <sup>-1</sup>	2.56 cm <sup>-1</sup>	4.36 cm <sup>-1</sup>	11.20 cm <sup>-1</sup>	9.57 cm <sup>-1</sup>	5.79 cm <sup>-1</sup>	67.89 cm <sup>-1</sup>
Temperature	293 K	200 K	200 K	200 K	200 K	293 K	200 K	296 K	200 K	200 K
No. of Reflections Measured	Total: 8736 Unique: 2512 (R <sub>int</sub> = 0.038)	Total: 9216 Unique: 2133 (R <sub>int</sub> = 0.053)	Total: 12909 Unique: 3094 (R <sub>int</sub> = 0.025)	Total: 8184 Unique: 3430 (R <sub>int</sub> = 0.199)	Total: 7768 Unique: 3938 (R <sub>int</sub> = 0.045)	Total: 8338 Unique: 4871 (R <sub>int</sub> = 0.073)	Total: 16990 Unique: 4038 (R <sub>int</sub> = 0.026)	Total: 6900 Unique: 3155 (R <sub>int</sub> = 0.031)	Total: 3803 Unique: 1711 (R <sub>int</sub> = 0.055)	Total: 5952 Unique: 1445 (R <sub>int</sub> = 0.063)
No. of Reflections (All, 2θ < 54.97°)	1471	1641	2628	1599	2751	2266	2873	1419	1172	802
No. of Variables	145	109	145	181	217	271	217	163	159	73
Residuals: R; R <sub>w</sub>	5.2 %; 8.0 %	4.5 %; 11.9 %	3.4 %; 10.2 %	8.3 %; 27.5 %	5.6 %; 17.8 %	7.2 %; 20.2 %	4.2 %; 13.1 %	6.5 %; 28.6 %	8.6 %; 27.6 %	8.4 %; 24.8 %
Goodness of Fit Indicator	1.02	1.07	1.02	0.8	0.93	0.90	1.09	1.08	2.5	0.91
Diffraction Source	Rigaku/MSC Mercury CCD	Rigaku Rapid-S Imaging Plate	Rigaku/MSC Mercury CCD	Rigaku Rapid-S Imaging Plate	Rigaku Rapid-S Imaging Plate	Rigaku DSC Imaging Plate (Synchrotron in KEK)	Rigaku Rapid-S Imaging Plate			

A4. Slideshow for Ph.D Defense (February 7th, 2011)

Presentation for Ph.D Defense

## Development of Small $\pi$ -Conjugated Molecules with Long Alkyl Chains for Organic Field-Effect Transistors

(長鎖アルキル基を導入した低分子トランジスタ材料の開発)

D083606 土井伊織

工学研究科  
物質化学システム専攻  
応用有機化学研究室

広島大学

Ph.D defense : Development of  $\pi$ -Conjugated Molecules with Long Alkyl Chains for OFETs

**CHAPTER 1**  
General Introduction

**CHAPTER 2**  
Development of Heteroaromatic-Fused TTFs as Organic Semiconductors for Solution Processible Field-Effect Transistors  
*I. Doi et al, Chem. Mater. 2007, 19, 5230.*  
*I. Doi et al, Chem. Lett. 2008, 37, 1088.*

**CHAPTER 3**  
Evaluation of C<sub>18</sub>-DNTT as Organic Semiconductors for High Performance Thin-Film Transistors  
*I. Doi et al, Cur. Appl. Phys. submitted.*  
*Kang et al, Adv. Mater. in press.*

Ph.D defense : Development of  $\pi$ -Conjugated Molecules with Long Alkyl Chains for OFETs

**CHAPTER 1 GENERAL INTRODUCTION**

**ORGANIC ELECTRONIC MATERIALS**  
Organic compounds are insulator

$\pi$ -Compounds + carrier-dope give conductors

Controlling the carrier by field-effect give transistors

Ph.D defense : Development of  $\pi$ -Conjugated Molecules with Long Alkyl Chains for OFETs

**ORGANIC FIELD-EFFECT TRANSISTOR (OFET)**

ON-state (conducting)  $\longleftrightarrow$  OFF-state (insulating)  
Gate-electric field

How arrange neutral molecules regularly on a substrate

Planer Dielectric  $\longleftrightarrow$  Self-organizing ability

Electrostatic potential  
Dipoles  
Hydrophobic/hydrophilic  
Steric hindrance

Many compounds have been developed

Si/SiO<sub>2</sub> Surface roughness < 0.1 nm (smaller than a molecule)  
Inorganic Insulating Polymers

Ph.D defense : Development of  $\pi$ -Conjugated Molecules with Long Alkyl Chains for OFETs

**ADVANTAGES OF OFETs**

- Flexible
- Low-process temperature
- Low-cost
- Large area fabrication

Need solution-process

Solution-process materials should be improved

Ph.D defense : Development of  $\pi$ -Conjugated Molecules with Long Alkyl Chains for OFETs

## CHAPTER 2 DEVELOPMENT OF SEMICONDUCTOR

**SMALL  $\pi$ -COMPOUNDS + LONG ALKYL CHAINS**

Solution-process

Heteroaromatic-fused TTFs

Source Drain  
Organic Semiconductor  
Dielectric  
Gate  
Substrate

**Design**  $\pi$ -core

**Synthesis**

9 steps  
KOH + CS<sub>2</sub>

**FET characteristics**

**Structural / theoretical analysis**

7

Ph.D defense : Development of  $\pi$ -Conjugated Molecules with Long Alkyl Chains for OFETs

## CHAPTER 3 EVALUATION & APPLICATION

**SMALL  $\pi$ -COMPOUNDS + LONG ALKYL CHAINS**

Vacuum-process

Alkylated DNTT

Source Drain  
Organic Semiconductor  
Dielectric  
Gate  
Substrate

**Device configuration**

Si/SiO<sub>2</sub> substrate

Plastic substrate

Chapter 3 is omitted in this presentation

8

Ph.D defense : Development of  $\pi$ -Conjugated Molecules with Long Alkyl Chains for OFETs

## CHAPTER 1

General Introduction

## CHAPTER 2

Development of Heteroaromatic-Fused TTFs as Organic Semiconductors for Solution Processible Field-Effect Transistors

- 2.1 Introduction for Organic Semiconductors
- 2.2 Bis(N-alkyl-pyrrolo[3,4-d])tetrathiafulvalenes (N-alkyl-PyTTFs)
  1. Doi et al., *Chem. Mater.* **2007**, *19*, 5230.
- 2.3 Bis(N-acyl-pyrrolo[3,4-d])tetrathiafulvalenes (N-acyl-PyTTFs)
  1. Doi et al., *Chem. Lett.* **2008**, *37*, 1088.
- 2.4 Bis(thieno[2,3-d])tetrathiafulvalenes ( $\alpha$ DT-TTFs)
  1. Doi et al., *Chem. Lett.* **2008**, *37*, 1088.
- 2.5 Correlation between Electronic Structure in Solid State and Field-Effect Mobility
- 2.6 Conclusion for Chapter 2

## CHAPTER 3

Evaluation of C<sub>18</sub>-DNTT as Organic Semiconductors for High Performance Thin-Film Transistors

- 3.1 Introduction for Alkylated DNTT
- 3.2 Evaluation on Silicon Substrates Kang et al., *Adv. Mater.* in press.
- 3.3 Fabrication of Polymer Dielectrics
- 3.4 Evaluation on Plastic Substrates I. Doi et al., *Cur. Appl. Phys.* submitted.
- 3.5 Conclusion for Chapter 3

9

Ph.D defense : Development of  $\pi$ -Conjugated Molecules with Long Alkyl Chains for OFETs

## CHAPTER 2 DEVELOPMENT OF SOLUTION-PROCESSIBLE ORGANIC SEMICONDUCTORS

Heteroaromatic-fused TTFs

**REPRESENTATIVE ORGANIC SEMICONDUCTOR**

**Pentacene**

$\mu_{FET} \sim 3 \text{ cm}^2/\text{Vs}$   
(vacuum-process)

Tan et al., *Appl. Phys. Lett.* **2009**, *94*, 263303.  
Klauk et al., *J. Appl. Phys.* **2002**, *92*, 5259-5263.  
Kelley et al., *J. Phys. Chem. B* **2003**, *107*, 5877.

**Herringbone**

Jung et al., *Appl. Phys. Lett.* **2005**, *86*, 083505-3.

**2D semiconducting layer parallel to the substrates**

Tan et al., *Chem. Mater.* **2007**, *19*, 3018.

10

Grain (Crystalline)

**1D conduction**

carrier

Weak against defects

**2D conduction**

carrier

**2D conduction is preferable for thin-film-based OFETs**

11

Ph.D defense : Development of  $\pi$ -Conjugated Molecules with Long Alkyl Chains for OFETs

## REPRESENTATIVE SOLUTION-PROCESSIBLE ORGANIC SEMICONDUCTOR

Regio-regular Alkyl thiophene

$\mu_{FET} = 0.1 \text{ cm}^2/\text{Vs}$

Alkyl/ $\pi$ - $\pi$  intermolecular interactions

Lamella structure (2D conducting layer)

Osaka et al., *Acc. Chem. Res.* **2008**, *41*, 1202.

✗ Drawbacks

- Low mobility
- Distribution Mw
- Synthetic limitation
- Difficulty of structural analysis

12

Ph.D defense : Development of  $\pi$ -Conjugated Molecules with Long Alkyl Chains for OFETs

### SMALL MOLECULES WITH SOLUBLE SUBSTITUENTS (1)

ex. Anthra-dithiophene core

TIPS group in acene core

2-D (R = Et)  $\mu_{FET} = -1.0 \text{ cm}^2/\text{Vs}$

1-D (R = *i*-Pr)  $\mu_{FET} = \sim 10^{-4} \text{ cm}^2/\text{Vs}$

J. E. Anthony et al., *J. Am. Chem. Soc.* **2005**, *127*, 4986.

- ✓ Soluble
- ✗ Organizing ability (1-D)
- ✗ Variation of  $\pi$ -cores

13

Ph.D defense : Development of  $\pi$ -Conjugated Molecules with Long Alkyl Chains for OFETs

### SMALL MOLECULES WITH SOLUBLE SUBSTITUENTS (2)

ex. Anthra-dithiophene core

$\mu_{FET} = -0.01 \text{ cm}^2/\text{Vs}$  (solution-cast)  
 $\sim 0.15 \text{ cm}^2/\text{Vs}$  (vacuum)

H.T. Karz et al., *J. Am. Chem. Soc.* **1998**, *120*, 664.

✗ Low solubility

$\mu_{FET} = 0.1 \text{ cm}^2/\text{Vs}$  (vacuum process)

$\mu_{FET} = 0.03 \text{ cm}^2/\text{Vs}$  (vacuum process)  
 $\mu_{FET} = 10^{-4} \text{ cm}^2/\text{Vs}$  (solution process)

Adv. Mater. **2007**, *19*, 1864-1868.

14

Ph.D defense : Development of  $\pi$ -Conjugated Molecules with Long Alkyl Chains for OFETs

### TETRATHIAFULVALENE (TTF)

- ✓ Donor in organic conductors
- ✓ Small  $\pi$ -core • aggregation (S atoms)
- ✓ Large coefficient on the sulfur atoms  $\Rightarrow$  strong intermolecular interaction

#### TTF-based Semiconductors

DT-TTF  $\mu_{FET}$  (crystal) =  $\sim 1.4 \text{ cm}^2/\text{Vs}$   
 Rovira et al., *JACS*, **2004**, *126*, 984.

$\mu_{FET} = 0.4 \text{ cm}^2/\text{Vs}$   
 Yamashita et al., *JACS*, **2005**, *127*, 10142.

$\mu_{FET} = 0.11 \text{ cm}^2/\text{Vs}$   
 Mori et al., *Chem. Lett.* **2005**, *34*, 392.

S-S &  $\pi$ - $\pi$  contacts (Herringbone like)

15

Ph.D defense : Development of  $\pi$ -Conjugated Molecules with Long Alkyl Chains for OFETs

causes disorder in thin film

⚠ Attention

$\text{cis/trans}$  equilibrium in solution

Tetra-substitution perturbs S-S interactions • 1D • LC

$\mu_{FET} = \sim 0.08 \text{ cm}^2/\text{Vs}$  (solution, dip)  
 Chem. Mater. **2006**, *18*, 4724.

$\mu_{FET} = \sim 0.02 \text{ cm}^2/\text{Vs}$  (solution)  
 Chem. Comm. **2006**, 2750.

16

Ph.D defense : Development of  $\pi$ -Conjugated Molecules with Long Alkyl Chains for OFETs

### HETEROAROMATIC-FUSED TTFs

$\mu_{FET} = 1.4 \text{ cm}^2/\text{Vs}$

1  $C_{17}$ -PyTTF

2  $C_{17}$ -AcPyTTF

3  $SC_{17}$ - $\alpha$ DT-TTFs same thiophene ring

- ✓ Heteroaromatic-fused TTF + Long alkyl chains
- Solubility
- S-S &  $\pi$ - $\pi$  intermolecular interactions
- Small steric disorder by *cis/trans* isomerization

17

Ph.D defense : Development of  $\pi$ -Conjugated Molecules with Long Alkyl Chains for OFETs

### $C_{17}$ -PyTTF : SYNTHESIS (1)

Previous 6 step 22% J. Becher et al., *J. Org. Chem.* **2000**, *65*, 5794.

Improved: 5 step 31%

*Inorg. Chem.* **2001**, *40*, 1902.

*Tetrahedron Lett.* **1973**, 2553.  
*Tetrahedron Lett.* **1989**, 134.

*Tetrahedron Lett.* **1994**, 269.

18

Ph.D defense : Development of  $\pi$ -Conjugated Molecules with Long Alkyl Chains for OFETs

### SYNTHESIS (2)

R	yield / %	solubility / g L <sup>-1</sup>
C <sub>1</sub> CH <sub>3</sub>	79	<0.01
C <sub>4</sub> <i>n</i> -C <sub>4</sub> H <sub>9</sub>	71	10
C <sub>8</sub> <i>n</i> -C <sub>8</sub> H <sub>17</sub>	75	29
C <sub>12</sub> <i>n</i> -C <sub>12</sub> H <sub>25</sub>	61	50
C <sub>16</sub> <i>n</i> -C <sub>16</sub> H <sub>33</sub>	79	4
C <sub>20</sub> <i>n</i> -C <sub>20</sub> H <sub>41</sub>	53	0.4

in toluene at rt. 19

**High solubility**

- C<sub>16</sub> & C<sub>20</sub>: Low

Ph.D defense : Development of  $\pi$ -Conjugated Molecules with Long Alkyl Chains for OFETs

### THIN-FILM FABRICATION & FET CHAR.

Solution-Processible (> <i>n</i> -C <sub>4</sub> H <sub>9</sub> )	
R	FET characteristics
	$\mu$ / cm <sup>2</sup> V <sup>-1</sup> s <sup>-1</sup> $I_{on}/I_{off}$
H	no field-effect
C <sub>1</sub> CH <sub>3</sub>	5 × 10 <sup>-5</sup>
C <sub>4</sub> <i>n</i> -C <sub>4</sub> H <sub>9</sub>	2 × 10 <sup>-5</sup> 10 <sup>1</sup>
C <sub>8</sub> <i>n</i> -C <sub>8</sub> H <sub>17</sub>	no field-effect
C <sub>12</sub> <i>n</i> -C <sub>12</sub> H <sub>25</sub>	6 × 10 <sup>-3</sup> 10 <sup>2</sup>
C <sub>16</sub> <i>n</i> -C <sub>16</sub> H <sub>33</sub>	8 × 10 <sup>-3</sup> 10 <sup>4</sup>
C <sub>20</sub> <i>n</i> -C <sub>20</sub> H <sub>41</sub>	0.01    10 <sup>4</sup>

From toluene solutions

**Longer alkyl chains**  
⇒ **higher performances**

Ph.D defense : Development of  $\pi$ -Conjugated Molecules with Long Alkyl Chains for OFETs

### THIN-FILM XRDs

R	<i>d</i> -spacing / Å	$\mu_{FET}$ / cm <sup>2</sup> Vs <sup>-1</sup>
<b>A</b> C <sub>4</sub> <i>n</i> -C <sub>4</sub> H <sub>9</sub>	10.2 ; 8.5	2 × 10 <sup>-5</sup>
C <sub>8</sub> <i>n</i> -C <sub>8</sub> H <sub>17</sub>	12.6	-
<b>B</b> C <sub>12</sub> <i>n</i> -C <sub>12</sub> H <sub>25</sub>	21.0	6 × 10 <sup>-3</sup>
C <sub>16</sub> <i>n</i> -C <sub>16</sub> H <sub>33</sub>	26.8	8 × 10 <sup>-3</sup>
C <sub>20</sub> <i>n</i> -C <sub>20</sub> H <sub>41</sub>	32.3	0.01

**Crystalline thin films**

**Large interlayer distance (*d*-spacing) : High mobility**

***d*-Spacing = Crystallographic *c*-axis ..... similar structure**

21

Ph.D defense : Development of  $\pi$ -Conjugated Molecules with Long Alkyl Chains for OFETs

### MOLECULAR ARRANGEMENTS IN SINGLE-CRYSTAL

**A** C<sub>8</sub>-PyTTF

$\mu_{FET}$  = no field-effect

Small  $\pi$ - $\pi$  overlaps

**B** C<sub>16</sub>-PyTTF

$\mu_{FET}$  = 0.008 cm<sup>2</sup>/Vs

Large  $\pi$ - $\pi$  overlaps

22

Ph.D defense : Development of  $\pi$ -Conjugated Molecules with Long Alkyl Chains for OFETs

### SUMMARY OF C<sub>n</sub>-PyTTF

**Longer alkyl chains = Higher mobility**

R = C<sub>20</sub>:  $\mu_{FET}$  = 0.01 cm<sup>2</sup>/Vs    Hydrophobic interactions

**Low air-stability**

Low oxidation potential causes (E<sup>1/2</sup> vs. Fc/Fc<sup>+</sup>) = -0.11 eV

oxidation

-4.6 HOMO estimated from CV

stored in air

23

Ph.D defense : Development of  $\pi$ -Conjugated Molecules with Long Alkyl Chains for OFETs

### C<sub>n</sub>-AcPyTTF

**Air-stability** → Oxidation potentials → Introduction of EDW groups

C<sub>n</sub>-PyTTF

N-Acyl groups

C<sub>n</sub>-AcPyTTF

MO calc. (DFT:B3LYP/6-31G\*)

E <sub>HOMO</sub>	-4.2 eV (exp. -4.6 eV)
	-4.9 eV

24

Ph.D defense : Development of  $\pi$ -Conjugated Molecules with Long Alkyl Chains for OFETs

### SYNTHESIS

R	name	yield (%)	solubility (g L <sup>-1</sup> )
C <sub>1</sub>	acetyl	60	< 5 × 10 <sup>-4</sup>
C <sub>5</sub>	hexanoyl	56	1 × 10 <sup>-2</sup>
C <sub>11</sub>	dodecanoyl	74	2 × 10 <sup>-3</sup>

**✗ Insoluble**

25

Ph.D defense : Development of  $\pi$ -Conjugated Molecules with Long Alkyl Chains for OFETs

### OXIDATION POTENTIALS

HOMO level  
Std : E<sub>Fc/Fc+</sub> = -4.8 eV

Molecule	HOMO level (eV)
PyTTF	-4.62
AcPyTTF	-4.95

**✓ Oxidation potential increases +0.3 eV**

26

Ph.D defense : Development of  $\pi$ -Conjugated Molecules with Long Alkyl Chains for OFETs

### FET CHARACTERISTICS

R	$\mu_{\text{FET}} / \text{cm}^2 \text{V}^{-1} \text{s}^{-1}$	$I_{\text{on}} / I_{\text{off}}$
C <sub>1</sub> : CH <sub>3</sub>	~ 0.05 <sup>a</sup>	10 <sup>4</sup>
C <sub>5</sub> : <i>n</i> -C <sub>5</sub> H <sub>11</sub>	~ 0.08 <sup>b</sup>	10 <sup>5</sup>
C <sub>11</sub> : <i>n</i> -C <sub>11</sub> H <sub>23</sub>	no field effect	
cf: <i>N</i> - <i>n</i> -alkyl-PyTTF	~ 0.01	10 <sup>4</sup>

<sup>a</sup> HMDS-treated SiO<sub>2</sub>; T<sub>amb</sub> = 100°C. <sup>b</sup> ODTS-treated SiO<sub>2</sub>; T<sub>amb</sub> = 100°C

**✓ C<sub>5</sub>-AcPyTTF Improve mobility and air-stability**

27

Ph.D defense : Development of  $\pi$ -Conjugated Molecules with Long Alkyl Chains for OFETs

### THIN-FILM XRDs

Molecule	d-spacing / Å
C <sub>11</sub> -AcPyTTF	-
C <sub>5</sub> -AcPyTTF	23
C <sub>1</sub> -AcPyTTF	17

**✓ Crystalline thin films for C<sub>1</sub> & C<sub>5</sub>**

28

Ph.D defense : Development of  $\pi$ -Conjugated Molecules with Long Alkyl Chains for OFETs

### MOLECULAR ARRANGEMENT IN SINGLE-CRYSTAL

**✓ Herringbone + S-S contacts**

Formula: C<sub>27</sub>H<sub>36</sub>N<sub>2</sub>O<sub>2</sub>S<sub>4</sub>  
System: triclinic  
Lattice: a = 4.914(4) Å  
b = 10.260(8) Å  
c = 22.87(2) Å  
α = 95.18(1)°  
β = 91.54(1)°  
γ = 90.84(1)°  
R merge: 7.2%

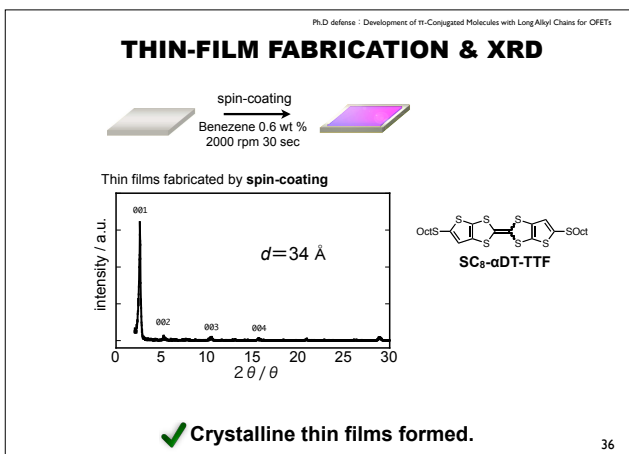
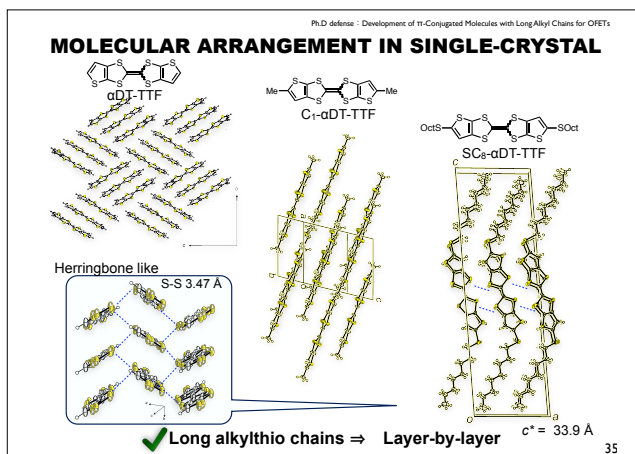
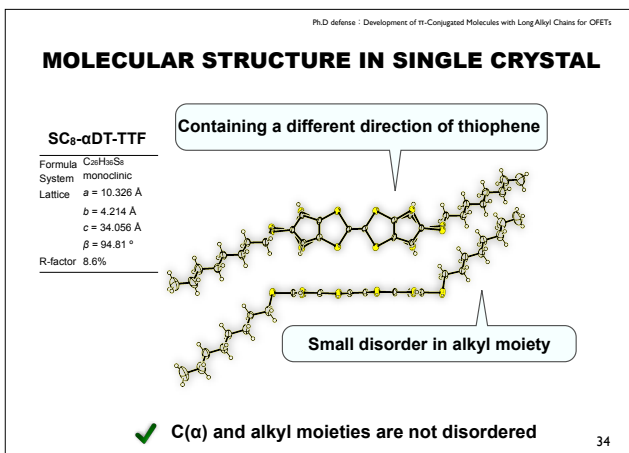
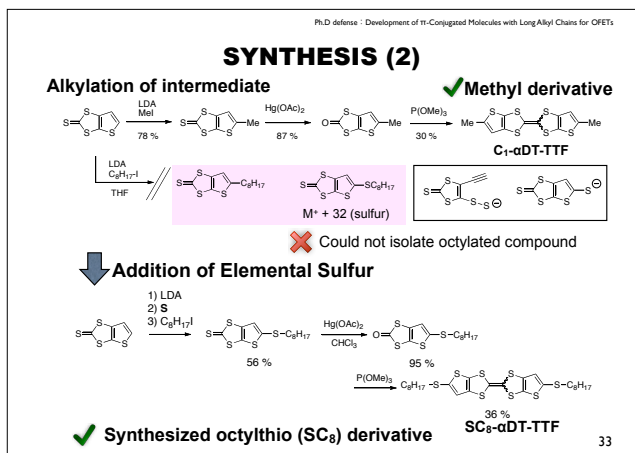
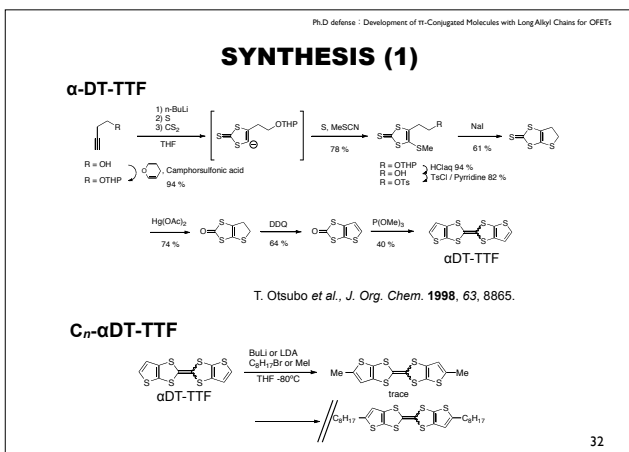
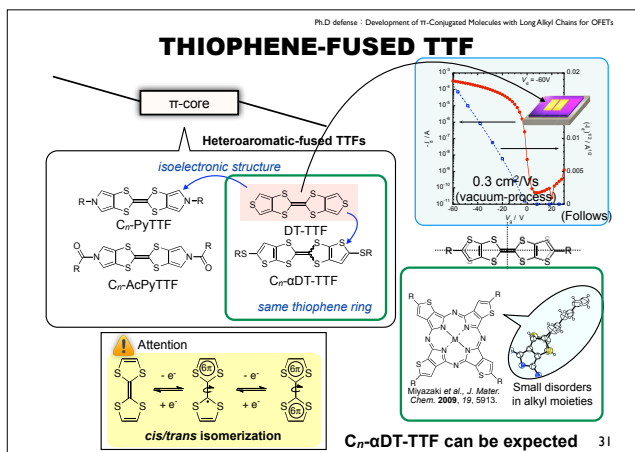
29

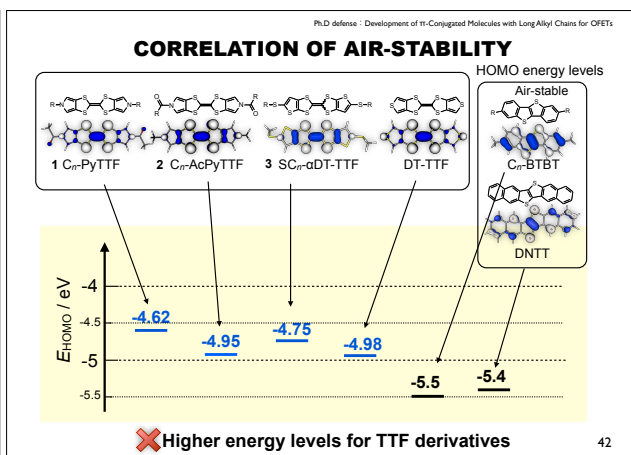
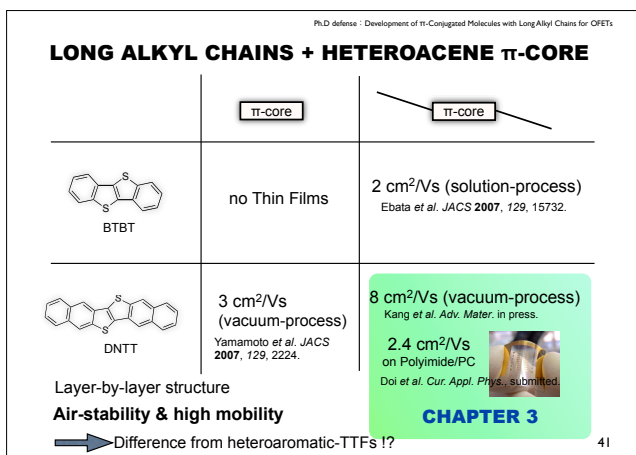
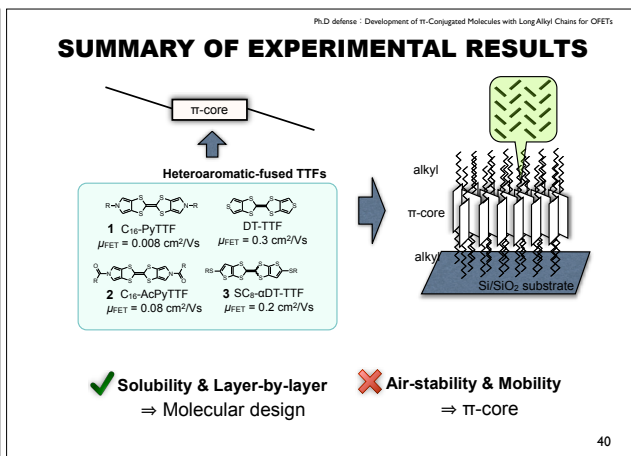
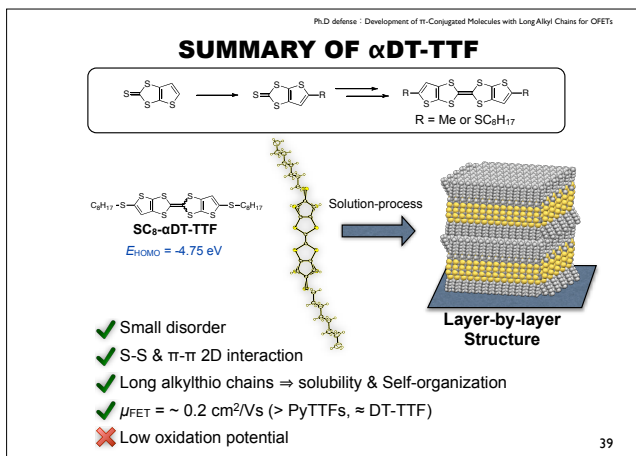
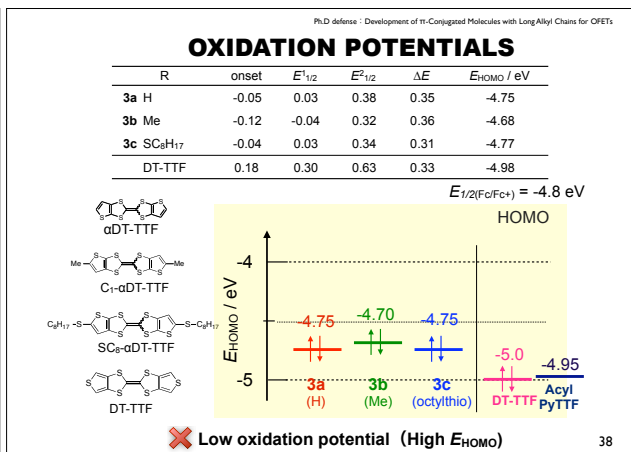
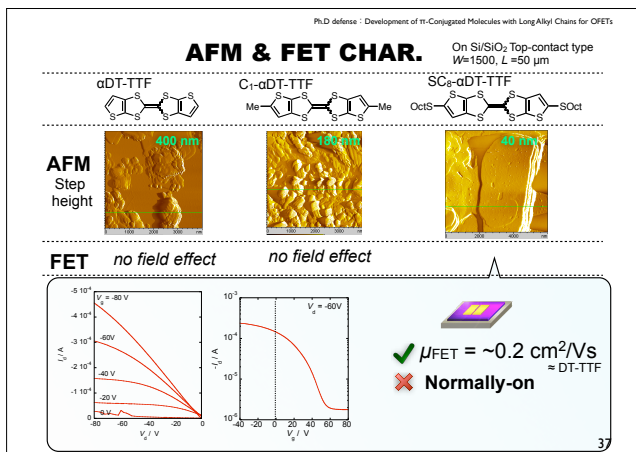
Ph.D defense : Development of  $\pi$ -Conjugated Molecules with Long Alkyl Chains for OFETs

### SUMMARY OF C<sub>n</sub>-AcPyTTF

**Layer-by-layer structure**  
**2D conducting layer**  
**μ<sub>FET</sub> ~ 0.08 cm<sup>2</sup>/Vs**  
**Air-stability** ✗ **Solubility**

30





Ph.D defense : Development of  $\pi$ -Conjugated Molecules with Long Alkyl Chains for OFETs

### CORRELATION OF MOBILITY

**Packing of C<sub>12</sub>-BTBT (DNNT is similar)**

Typical Herringbone fashion  
S-S 3.54 Å

**Heteroaromatic-fused TTFs**

S-S	$\mu_{FET}$
3.40 Å	✓
< 3.57 Å	✓
3.46 Å	✓
3.55 Å	✓

**How was the strong S-S interaction !?**  
It is necessary to evaluate electronic structure quantitatively.

43

Ph.D defense : Development of  $\pi$ -Conjugated Molecules with Long Alkyl Chains for OFETs

### MECHANISM OF ELECTRON-TRANSFER

To evaluate electronic structure / properties relating to hole transport quantitatively  
Mechanism in well-ordered organic semiconductors

**Hopping Model**

A hole is considered to be transferred via overlap of orbitals.

**Electronic Transfer rate  $k_{ET}$  (Marcus Theory)**

$$k_{ET} = \tau^{-1} \sqrt{\frac{\pi}{\hbar k_B T \lambda}} \exp\left(-\frac{(\Delta E - \lambda)^2}{4\lambda k_B T}\right)$$

**Two major parameters**

- $t$  : transfer integral  
Portion for energy gain
- $\lambda$  : reorganization energy  
Portion for energy loss

**Calculate  $t$  &  $\lambda$  in following slides**

44

Ph.D defense : Development of  $\pi$ -Conjugated Molecules with Long Alkyl Chains for OFETs

### REORGANIZATION ENERGY ( $\lambda$ )

for hole  $\lambda^h$

Energy-loss when a hole transfers to the neighboring one

**DEFINITION : Sum of two relaxation energy**

$$\lambda^h = \lambda_{rel}^{(1)} + \lambda_{rel}^{(2)}$$

An isolated molecule in vacuum  
Keep planer conformation

B3LYP/6-31G(d), Gaussian 03 program 45

Ph.D defense : Development of  $\pi$ -Conjugated Molecules with Long Alkyl Chains for OFETs

### REORGANIZATION ENERGY ( $\lambda$ )

Compound	Structure	$\lambda^h$ (meV)	$\mu_{FET}$ (cm <sup>2</sup> /Vs)
1 C <sub>16</sub> -PyTTF		280	0.008
2 C <sub>5</sub> -AcPyTTF		350	0.08
3 SC <sub>8</sub> -dDT-TTF		- <sup>a</sup>	0.2
DT-TTF		253	0.3
C <sub>12</sub> -BTBT		239	2
DNNT		130	3

<sup>a</sup> Alkylthio derivative has large value because of taking a boat form

**✗ TTFs have large values** → **Aromaticity** (boat form) vs **Non-aromaticity** (planar form)

Acyl derivative : the largest value

46

Ph.D defense : Development of  $\pi$ -Conjugated Molecules with Long Alkyl Chains for OFETs

### TRANSFER INTEGRAL ( $t$ )

**Electronic coupling between neighboring molecules**  
Evaluation of strength of electronic bonding

Neglect phases (+ or -)

Program ADF (Amsterdam density functional)  
Function Slater-type orbital approximation  
Triple- $\zeta$  polarization (TZP) basis set  
Level GGA-PW91

**Calculate  $t$  of dimers in single-crystal structure**

47

Ph.D defense : Development of  $\pi$ -Conjugated Molecules with Long Alkyl Chains for OFETs

### TRANSFER INTEGRAL $t_{HOMO}$

Compound	$t_{HOMO}$ (meV)	$\mu_{FET}$ (cm <sup>2</sup> /Vs)
C <sub>8</sub> -PyTTF (no field-effect (solution))	$\frac{p}{q} = 14$ $\frac{r}{s} = 17^a$	-
C <sub>16</sub> -PyTTF (0.008 cm <sup>2</sup> /Vs (solution))	$\frac{p}{q} = 87^a$ $\frac{r}{s} = 3^b$	-
C <sub>5</sub> -AcPyTTF (0.08 cm <sup>2</sup> /Vs (vacuum))	$\frac{p}{q} = 33^a$ $\frac{r}{s} = 25^a$ $\frac{r}{s} = 45^b$ $\frac{r}{s} = 43^b$	-

<sup>a</sup> S-S 3.37 Å      <sup>a</sup>  $\pi$ - $\pi$  3.57 Å, <sup>b</sup> S-S 3.40 Å

**1-D**      **2-D**

**✓ 2D electronic interaction = higher mobility**

**S-S short contact**      **S-S contact  $\neq$  Electronic Interaction**

48

Ph.D defense : Development of  $\pi$ -Conjugated Molecules with Long Alkyl Chains for OFETs

### TRANSFER INTEGRAL $t_{HOMO}$

C6H13-S-C6H4-S-C6H4-S-C6H13

0.2 cm<sup>2</sup>/Vs (solution)

$t_{HOMO}$  (meV)  
p 14<sup>a</sup>  
q 54<sup>b</sup>  
r 53<sup>b</sup>

<sup>a</sup> S-S 3.46 Å.  
**2-D**

S-C6H4-S-C6H4-S

DT-TTF

0.3 cm<sup>2</sup>/Vs (vacuum)

$t_{HOMO}$  (meV)  
p 55<sup>a</sup>  
q 34<sup>b</sup>  
r 34<sup>b</sup>

<sup>a</sup> S-S 3.55 Å.  
**2-D**

✓ Moderate  $t$  in two directions  $\Rightarrow$  2D conducting layer  
Values are larger than those in PyTTFs

49

Ph.D defense : Development of  $\pi$ -Conjugated Molecules with Long Alkyl Chains for OFETs

### TRANSFER INTEGRAL $t_{HOMO}$

C12H25-C6H4-S-C6H4-S-C6H4-S-C12H25

C<sub>12</sub>-BTBT

2 cm<sup>2</sup>/Vs (solution)

$t_{HOMO}$  (meV)  
p 62<sup>a</sup>  
q 46<sup>b</sup>  
r 46<sup>b</sup>

<sup>a</sup> S-S 3.54 Å.  
**2-D**

C12H25-C6H4-S-C6H4-S-C6H4-S-C12H25

DNTT

3 cm<sup>2</sup>/Vs (vacuum)

$t_{HOMO}$  (meV)  
p 71<sup>a</sup>  
q 91<sup>a</sup>  
r 14<sup>b</sup>

<sup>a</sup> CH- $\pi$  2.78 Å. <sup>b</sup> CH- $\pi$  2.73 Å  
**2-D**

$t$  (50 ~ 90 meV) in two directions  
✓  $\Rightarrow$  Stronger interactions than those in TTF derivatives

50

Ph.D defense : Development of  $\pi$ -Conjugated Molecules with Long Alkyl Chains for OFETs

### SUMMARY OF TRANSFER INTEGRALS

S-S contact direction

compd.	structure	$t_{HOMO}$ (meV)			$\mu_{FET}$ (cm <sup>2</sup> /Vs)
		perp	side1	side2	
1	C <sub>16</sub> -PyTTF	87	3	1	0.008
2	C <sub>17</sub> -AcPyTTF	29 <sup>a</sup>	45	43	0.08
3	SC <sub>8</sub> -oDT-TTF	14	54	53	0.2
	DT-TTF	55	34	34	0.3
	C <sub>12</sub> -BTBT	62	46	46	2
	DNTT	71	91	14	3

$t$  = correlates with mobility (dimensionality & abs value)  
Not all S-S contact give electronic interactions

51

Ph.D defense : Development of  $\pi$ -Conjugated Molecules with Long Alkyl Chains for OFETs

### EX. OF EFFECTIVE S-S INTERACTION IN TTF

C10H8S2

HM-TTF

Thin films : 3 cm<sup>2</sup>/Vs (vacuum)  
Crystal : 8 cm<sup>2</sup>/Vs

Chem Mater. 2007, 19, 6382.  
J. Mater. Chem. 2009, 19, 6548.

$t_{HOMO}$  (meV)  
p 40<sup>a</sup>  
q 105<sup>b</sup>  
r 28<sup>b</sup>

**Quasi 2-D**

<sup>a</sup>  $\pi$ - $\pi$  3.6 Å. <sup>b</sup> S-S 3.55 Å.  $\leftrightarrow$  3.46 Å (SC<sub>8</sub>-oDT-TTF).

**S-S interaction**

- Distance
- Position

**Both needed.**

$\pi$ -Orbital expands the  $\pi$ -plane normal (anisotropic)

52

Ph.D defense : Development of  $\pi$ -Conjugated Molecules with Long Alkyl Chains for OFETs

### SUMMARY OF CHAPTER 2

$\pi$ -CORE

alkyl

$\pi$ -core

alkyl

Si/SiO<sub>2</sub> substrate

- ✓ **Good Molecular Design Strategy**
  - 2D electronic interaction in layer-by-layer structures
- ✓ **Correlation: FET Char. & Structures**
  - Low oxidation potentials (air-stability)
  - Large  $\lambda^{\pi}$  & small  $t$  in the Herringbone like packing (mobility)

$t_{HOMO} = \sim 50$  meV  $\leftrightarrow$  DNTT & BTBT

53

Ph.D defense : Development of  $\pi$ -Conjugated Molecules with Long Alkyl Chains for OFETs

### SUMMARY

#### Chapter 2

Long alkyl chains + heteroaromatic-fused TTFs (solution-process)

Compd.	Solubility	Air-stability	cm <sup>2</sup> /Vs Mobility	Layer-by-layer
1 C <sub>n</sub> -PyTTF	○	✗	0.01	○
2 C <sub>n</sub> -AcPyTTF	✗	○	0.08	○
3 SC <sub>8</sub> -oDT-TTF	○	✗	0.2	○

Correlated electronic Structure  $E_{HOMO}$   $\leftrightarrow$   $t$  values/dimensionality  $\lambda^{\pi}$  values

#### Chapter 3

Heteroacene core + Long alkyl chains (vacuum-process)

C<sub>10</sub>-DNTT 8 cm<sup>2</sup>/Vs on Si/SiO<sub>2</sub>  $\leftrightarrow$  DNTT  $\sim$ 2.1 cm<sup>2</sup>/Vs  
2.4 cm<sup>2</sup>/Vs on PC/polyimide  $\leftrightarrow$  DNTT  $\sim$ 0.4 cm<sup>2</sup>/Vs

✓ **Long alkyl chains along a small  $\pi$ -conjugated molecule promote formation of 2D conducting layers which suitable for thin-film-based OFETs owing to its hydrophobic interaction. The resulting semiconductors showed high characteristics even on plastic substrates.**

54



## List of Publications

### Contributed Paper 1 (Article): Section 2.2

Doi, I.; Miyazaki, E.; Takimiya, K.; Kunugi, Y. "Development of *N*-Alkyl-Substituted Bis(pyrrolo[3,4-*d*])tetrathiafulvalenes as Organic Semiconductors for Solution Processible Field-Effect Transistors" *Chemistry of Materials*. **2007**, *19*, 5230.

### Contributed Paper 2 (Letter): Section 2.3

Doi, I.; Miyazaki, E.; Takimiya, K. "Synthesis and Characterization of *N*-Acyl-Substituted PyrroloTTF Derivatives and Improvement Air-Stability of PyrroloTTF-based OFETs" *Chemistry Letters*. **2008**, *37*, 1088.

### Contributed Paper 3 (Letter): Section 3.2

Kang, M. J.; Doi, I.; Mori, H.; Miyazaki, E.; Takimiya, K.; Ikeda, M.; Kuwabara, H. "Alkylated Dinaphtho[2,3-*b*:2',3'-*f*]thieno[3,2-*b*]thiophenes ( $C_n$ -DNTTs)" *Advanced Materials* in press.

### Contributed Paper 4 (Letter). Section 3.4

Doi, I.; Kang, M. J.; Takimiya, K. "High Mobility Organic Thin-Film Transistors on Plastic Substrates" *Current Applied Physics*, submitted.

### Related Paper 1

Uno, M.; Doi, I.; Takimiya, K.; Takeya, J. "Three-dimensional organic field-effect transistors with high output current and high on-off ratio" *Applied Physics Letters* **2009**, *94*, 103307.

### Related Paper 2

Uno, M.; Tominari, Y.; Yamagishi, M.; Doi, I.; Miyazaki, E.; Takimiya, K.; Takeya, J. "Moderately anisotropic field-effect mobility in dinaphtho[2,3-*b*; 2'3'-*f*]thiopheno[3,2-*b*]thiophenes single-crystal transistors" *Applied Physics Letters*, **2009**, *94*, 223308.

### Related Paper 3

Yamagishi, M.; Soeda, J.; Uemura, T.; Okada, Y.; Takatsuki, Y.; Nishikawa, T.; Nakazawa, Y.; Doi, I.; Takimiya, K.; Takeya, J. "Free-electron-like Hall effect in high-mobility organic thin-film transistors" *Phys. Rev. B* **2010**, *81*, 161306.

## Acknowledgment

This work had been carried out in Applied Organic Chemistry Research Group since 2005 until 2011. If it had not been for the support of following persons, I would not have been able to complete this study.

### Stuff Members

Prof. Kazuo Takimiya 瀧宮和男教授	Thank you for everything about the Ph.D work and thesis. お忙しい中本当にお世話になりました。明日から4時に起きます。
Dr. Eigo Miyazaki 宮崎栄吾助教	Thank you for his great support of X-ray and other technical advices for ca. 5 years. 5年間に渡る技術的な指導、特にX線解析と多岐にわたる助言に感謝いたします。
Dr. Itaru Osaka 尾坂格助教	I really admit his challengeable carrier and optimism. チャレンジ精神溢れるキャリアと楽観主義を尊敬しています。
Prof. emeritus Tetsuo Otubo 大坪徹夫名誉教授	His advices were correct for me now. 一年間の短期間でしたが指導していただきありがとうございました。
岩谷さん	元素分析でお世話になりました。
Secretary Hashimoto Keiko 橋本恵子秘書	She supported everything during writing this thesis. 論文執筆中には一番お世話になりました。
Dr. Tatsuya Yamamoto 山本達也博士	I will work as a post-doctor like him DNNTTは偉大です。

### Takeya Research Group

Prof. Junichi Takeya 竹谷純一教授	He gave me great inspiration and motivation for study on organic transistor. 恐縮ながら共同研究者として活動できたことに本当に感謝しています。
Dr. Takafumi Uemura 植村隆文助教	Thank you for his advice for device fabrication. I respect your fascinating techniques. デバイス研究に関する御助言ありがとうございました。高い技術を見習います。
Dr. Mayumi Uno 宇野真由美博士	It was nice work with you although short time. お手伝いさせていただいた時の実験が成果に結びついたようで非常に光栄です。
Dr. Masakazu Yamagishi 山岸正和博士	He is one of the few graduates in same year. I hope our success in the future. 研究室は違いましたが数少ない僕の同期生ですね。これからもよろしく。

### Excellent Collaborators

Mr. Kiyotaka Goshome 五升目清剛	The Chapter 2.5 is almost your work! Thank you for grateful research. 本論文の第2章4節はほとんど君の成果です。ありがとう。
-------------------------------	--

### Excellent Doctoral Candidates

Dr.C. Hiroki Mori 森裕樹博士(見込)	Thank you for his leadership in our group with great beard for organic devices. 本研究室のリーダーとしてまたデバイスに関して多大なる支援ありがとう。
Dr.C. Myeong Jin Kang 姜明辰(姜명진)博士(見込)	I was able to enjoy my doctoral life with her cheerfulness and with her C <sub>10</sub> -DNNTT. いつも元気なミョンジンでいてください。
Dr.C. Shoji☆Sinamura 品村祥司博士(見込)	Research of the excellent, by the excellent, for the excellent. 分子軌道計算に関する多大な助言を頂き感謝いたします。
Dr.C. Tomoya Kashiki 榎木友也博士(見込)	I have no advice for your doctoral research. 博士論文の健闘をお祈りしています。
Dr.C. Masahiro Nakano 中野正浩 博士	I hope you will enjoy your synthesis on my desk and equipment. 頑張ってください。

### Labmates (順不同)

香原くん	石根希望	西村健	斉藤慎彦	阿部達	秋田誠広	橋本雄人	瀬田梢	P山
龍ちゃん	工場長	典子さん	林秀輝博士	田辺寛幸博士	島脇雅史	柳井直幸	小松	新見くん
八田くん	P	まろ	キング	竹田さん	岩谷くん	野村くん	加来さん	
<b>Great classmates</b>								
伊澤隆文	じいちゃん	半田さん	中瀬くん					
<b>Great Seniors</b>								
渡久地さん	江端さん	香山さん						
鳴滝さん	宇野さん	本田さん	蔵田さん	多田さん	田中さん			

何よりここまで辛抱強く支援していただきました母・土井千恵美(+妹・小夜)に感謝申し上げます。

Sincerely  
Iori Doi 土井伊織